Charge and heat transport across interfaces in nanostructured porous Silicon

---

Haider Haseeb

Dissertation

zur Erlangung des akademischen Grades
Doctor rerum naturalium
(Dr. rer. nat.)
in der Wissenschaftsdisziplin Physik der kondensierten Materie

eingereicht an der

Mathematisch-Naturwissenschaftlichen Fakultät

Institut für Physik und Astronomie

der Universität Potsdam

und durchgeführt am

Helmholtz-Zentrum Berlin für Materialien und Energie GmbH

Ort und Tag der Disputation: Potsdam, 25.09.2023

Gutacher:

Prof. Dr. Patrick Huber
Technische Universität Hamburg und Deutsches Elektronen-Synchrotron DESY

PD Dr. Klaus Habicht
Universität Potsdam und Helmholtz-Zentrum Berlin

Prof. Dr. Matias Bargheer
Universität Potsdam und Helmholtz-Zentrum Berlin

Betreuer:

Dr. Tommy Hofmann
Helmholtz-Zentrum Berlin

Published online on the
Publication Server of the University of Potsdam:
https://doi.org/10.25932/publishup-61122
https://nbn-resolving.org/urn:nbn:de:kobv:517-opus4-611224

Dedicated to my beloved family

Abstract

This thesis discusses heat and charge transport phenomena in single-crystalline Silicon penetrated by nanometer-sized pores, known as mesoporous Silicon (pSi). Despite the extensive attention given to it as a thermoelectric material of interest, studies on microscopic thermal and electronic transport beyond its macroscopic characterizations are rarely reported. In contrast, this work reports the interplay of both.

PSi samples synthesized by electrochemical anodization display a temperature dependence of specific heat C_p that deviates from the characteristic T^3 behaviour (at $T < 50K$). A thorough analysis reveals that both 3D and 2D Einstein and Debye modes contribute to this specific heat. Additional 2D Einstein modes ($\sim 3\ meV$) agree reasonably well with the boson peak of SiO_2 in pSi pore walls. 2D Debye modes are proposed to account for surface acoustic modes causing a significant deviation from the well-known T^3dependence of C_p at $T < 50K$.

A novel theoretical model gives insights into the thermal conductivity of pSi in terms of porosity and phonon scattering on the nanoscale. The thermal conductivity analysis utilizes the peculiarities of the pSi phonon dispersion probed by the inelastic neutron scattering experiments. A phonon mean-free path of around 10 nm extracted from the presented model is proposed to cause the reduced thermal conductivity of pSi by two orders of magnitude compared to p-doped bulk Silicon. Detailed analysis indicates that compound averaging may cause a further 10-50% reduction. The percolation threshold of 65% for thermal conductivity of pSi samples is subsequently determined by employing theoretical effective medium models.

Temperature-dependent electrical conductivity measurements reveal a thermally activated transport process. A detailed analysis of the activation energy E_A^σ in the thermally activated transport exhibits a Meyer Neldel compensation rule between different samples that originates in multi-phonon absorption upon carrier transport. Activation energies E_A^S obtained from temperature-dependent thermopower measurements provide further evidence for multi-phonon assisted hopping between localized states as a dominant charge transport mechanism in pSi, as they systematically differ from the determined E_A^σ values.

List of Figures

List of Tables

Table of Contents

Introduction

Today's energy infrastructure is confronted with the problem of an extensive and ever increasing global energy consumption. It amounts already to 150000 TWh per year [3], that is 100 times more than roughly a century ago and a further, steep increase is expected.

If one does not want to rely either on nuclear energy and the construction of new nuclear plants because of well-known safety and environmental concerns, or on non-renewable sources like coal, oil or gas with limited abundance, then one must explore novel energy sources and develop an efficient, economic, and preferably green energy infrastructure to satisfy this energy demand.

Harvesting of sustainable energy in solar or wind parks, subsequent energy storage in novel ion batteries with high energy density or alternatively in the form of solar fuels through catalytic reactions, e.g., water splitting, as well as fuel cell technologies are considered as main pillars of the 21st century energy infrastructure [4, 5]. These technologies readily cover the chain that starts with harvesting energy and ends with using the energy.

Recycling of waste heat is one important aspect that must be part of the next generation energy infrastructure. Energy generation processes that are dependent for instance on fossil fuels are highly inefficient [6, 7]. Coal plants exploit only 40% of the fuel's energy content, 60% is lost in the form of waste heat [8]. The combustion of gasoline in cars is only to 20% efficient [9].

These two examples are only a "tip of the iceberg" selection for inefficient technologies. In general, an unfavorable ratio of 1:3 is estimated between "used" energy and energy loss respectively waste heat. It becomes obviously a paradigm for the near future, to develop technologies that harvest these energy losses. To this end, recent years saw a renewed interest in thermoelectric materials.

Thermoelectric materials are mostly solid-state systems [10]. They are capable to convert directly heat into electrical power and vice versa electrical power into temperature gradients [11, 12]. Envisioned applications for this material class include consequently but not exclusively thermal converters that harvest waste heat in exhaust systems, electric generators, and solid-state refrigerators without cryogenic and toxic liquids [13, 14].

Thermoelectric materials do not only come along with the promise to harvest and convert heat. Rather it becomes possible to design a new generation of customer products. It is possible to conceive devices without moving parts that are wearing off. Devices come in reach, which are

exceptionally quiet but highly reliable. Wearable electronics that are powered by body heat [15, 16] are envisioned for entertainment purposes as well as medical surveillance [17, 18].

The most used thermoelectric material of the past decades is bismuth telluride [19, 20]. Unfortunately, its conversion efficiency is too low to be of use for more than niche applications [21]. In general, state-of-the-art thermoelectrics are often plagued by low efficiencies, the need for non-abundant materials that are expensive and even toxic. Consequently, researchers identified the need for novel thermoelectric material classes, which overcome these obstacles.

The efficiency of thermoelectric materials scales with the figure of merit $zT = \sigma S^2/\kappa\, T$, which depends on electrical conductivity σ, Seebeck coefficient S and thermal conductivity κ as well as temperature T. Optimizing these parameters to obtain figure of merits way above unity is at the forefront of fundamental and applied research projects. Often, the slightly contradictory concept of an electron crystal and a phonon glass is propagandized [22, 23].

A main approach to improve the figure of merit is to manipulate the lattice thermal conductivity in crystalline thermoelectric materials [24, 25]. In skutterudites, rattler atoms are incorporated into the crystal to act as scattering centers for phonons thus reducing the thermal conductivity [26]. In nanostructured materials phonons are scattered at structural features like interfaces or boundaries [27, 28]. To improve electrical conductivity in thermoelectrics, doping or more challenging concepts like band engineering have been put forward [29].

So far, a material that fulfills all demands of being cheap, abundant, efficient and non-toxic has yet to be found. In all the existing research whether fundamental or applied, it becomes increasingly obvious that a thorough understanding of microscopic heat and charge transport in thermoelectric materials must at least accompany the quest for highly efficient systems. It is in this framework that the topic of this thesis was conceived.

In this thesis, I discuss charge and heat transport in mesoporous Silicon that is a form of nanostructured Silicon proposed for thermoelectric applications. The outline of the thesis is subsequently described.

Chapter 1 introduces the fundamental concepts of thermoelectricity. It critically reviews state-of-the art thermoelectrics and discusses strategies to get improved thermoelectric materials. Mesoporous Silicon (pSi) is introduced as thermoelectric material of interest.

Chapter 2 describes the synthesis of pSi by means of electrochemical anodization. It provides a comprehensive account on the experimental setup necessary for anodization. It finally details the chemical reaction processes during the synthesis.

Chapter 3 gives an overview of the main experimental techniques used to characterize heat and thermoelectric transport in pSi. The morphology of pSi samples is characterized by sorption isotherm measurements and scanning electron microscopy. The thermal transport is investigated by means of a laser flash apparatus (LFA) and a physical property measurement system (PPMS). The PPMS system is also utilized to measure the temperature dependent specific heat of pSi. Thermoelectric transport measurements utilize the dedicated SBA-equipment.

Chapter 4 concentrates on experimental results and their discussion. It presents a thorough interpretation of the temperature-dependent specific heat of pSi. A novel theoretical model is proposed to understand the thermal conductivity in pSi in terms of porosity and phonon scattering on the nanoscale. Electrical transport by multi-phonon assisted hopping between localized states is proposed as a dominant transport mechanism.

Chapter 5 concludes the thesis highlighting key scientific results.

1. Theory and fundamentals

1.1. Thermoelectric effects

Thermoelectric materials (TEMs) exploit the Seebeck effect and the Peltier effect for electrical energy generation and cooling, respectively [12, 30].

1.1.1. Seebeck effect

In 1821, Thomas Johann Seebeck discovered that two dissimilar materials joined together generate a potential difference (ΔV) while two ends are held at different temperatures. Charge carriers (electrons and holes) diffuse from a hot side to a cold side attributed to their high energy in the hot regime. Thus, a charge difference builds up between the hot and cold side and produces voltage and electric current. The Seebeck effect can be described as $S = -\Delta V/\Delta T$, where S is the Seebeck coefficient, ΔV is the voltage difference, and ΔT is the temperature difference between hot and cold sides of the junction [10]. The sign of Seebeck coefficient tells about type of charge carriers in a material. The positive values indicate the presence of holes while the negative values show the presence of electrons [30].

1.1.2. Peltier effect

In 1834, Jean Charles Peltier discovered that an electrical current can generate or remove heat at the junctions of two dissimilar conducting materials [12, 31]. For example, when a current passes through a circuit made of two different materials, Peltier heat absorbed at the junction can be measured with the relation, $Q = \Pi I$, where Q is the heat absorbed which is directly proportional to the current I, the proportionality constant being the Peltier coefficient Π of the materials used in the circuit [30].

Fig. 1-1 illustrates how a thermoelectric material can convert heat directly to electrical power (Seebeck effect) and how a material can heat up or cool down at an electrified junction (Peltier effect).

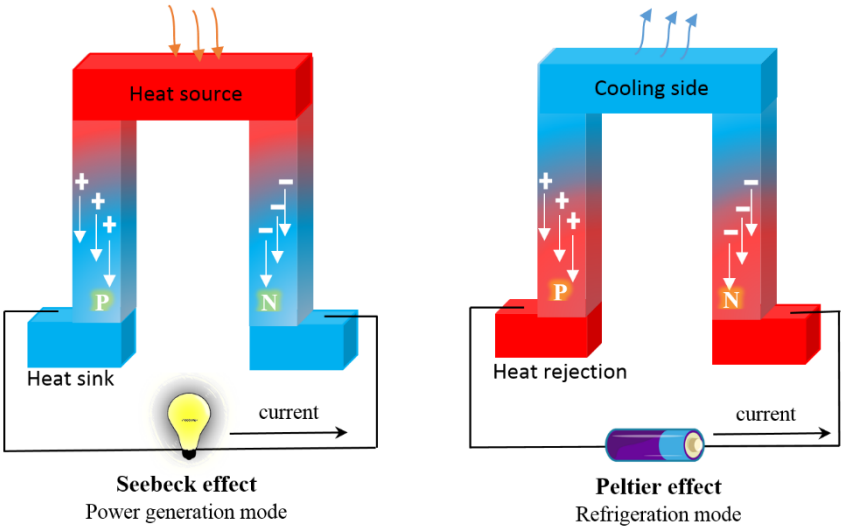

Fig. 1-1 Illustration of how a thermoelectric material can convert heat directly into electrical power via Seebeck effect (Left) and how a material can heat up or cool down via Peltier effect (Right).

1.2. Thermoelectric Figure of Merit

The energy conversion efficiency of TEMs is determined by the dimensionless figure of merit zT defined as:

$$zT = \frac{S^2\sigma}{\kappa}T = \frac{S^2\sigma}{\kappa_{electronic}+\kappa_{lattice}}T \tag{1.1}$$

where S, σ, κ and T are the Seebeck coefficient, the electrical conductivity, the thermal conductivity and the absolute temperature at which material properties are measured, respectively. The themoelectric device's efficiency is directly related to zT.

For power generation, the maximum efficiency Φ_{max} can be expressed as:

$$\Phi_{max} = \eta_c \gamma \tag{1.2}$$

where

$$\eta_c = \frac{T_h - T_c}{T_h} \tag{1.3}$$

$$\gamma = \frac{\sqrt{1+zT}-1}{\sqrt{1+zT}+{T_c}/{T_h}} \tag{1.4}$$

The maximum efficiency is the product of the Carnot efficiency η_c, and γ, which incorporates the parameters of the materials. T_h and T_c are the hot- and cold-end temperatures of the thermoelectric material of interest [30].

Suitable thermoelectric materials have zT values close to unity. However, a zT value of up to three is essential for thermoelectric energy converters that could compete with the efficiency of mechano-electric power generators [32]. Since the 1960s, research has been devoted to identifying TEMs that could satisfy this requirement.

A major challenge resides in three inter-connected physical properties used to calculate zT, i.e. S, σ and κ. In order to obtain a high zT value, S and σ should be high while κ should be reduced. Their interdependence has hindered the development of materials for thermoelectric applications [10, 12, 14, 32]. For their integration into devices, other challenges are encountered, such as the coupling of n- and p-type materials with metallic contacts and the coefficient of thermal expansion for materials [14].

1.3. Strategies to improve the thermoelectric Figure of Merit

The record of $zT \approx 1$ was broken in the mid-1990s by two different approaches: exploring new thermoelectric materials and reducing material dimensions [11, 23, 32-35].

1.3.1. Quest for new thermoelectric materials

Thermoelectric effects were first investigated for metals as thermo-elements [35]. However, Altenkirch's theoretical predictions for thermoelectric devices, clearly stated that metals were inefficient for thermoelectric applications [35]. Later, Goldsmid et al. contributed to finding the most suited semiconductors such as Bismuth Telluride (Bi_2Te_3) for thermoelectric devices [31]. Known as the first generation thermoelectrics with an average zT of about 1.0, these materials possessed device energy conversion efficiencies of 4-6% [31, 36]. Extensive research led to the development of second generation thermoelectrics with $zT \approx 1.7$ at high temperatures and device energy conversion efficiency of up to 12% [34]. These materials, namely clatharates, half-Heuslers, lead tellurides (LAST), and, loosely bonded atoms within a large cage exhibit the 'rattling' motion generating phonon scattering with minimal impact on charge transport [22]. Consequently, the thermal conductivity of these materials can be reduced while maintaining high electrical conductivity [14, 32, 34].

Thermoelectric materials can be further classified into three groups with respect to their operating temperatures [30]. Bismuth, antimony, tellurium, and selenium-based alloys are

classified under low-temperature materials that can be used at temperatures up to around $450K$. Materials based on lead telluride belong to the intermediate temperature range up to around $850K$ whereas thermoelectric materials employed at the highest temperatures are silicon-germanium based alloys that operate up to $1300K$. The low zT values of commercially available thermoelectric materials limit the performance of thermoelectric devices. Metals and metal alloys ($zT \ll 1$) can, for example, only be applied in thermocouples to measure temperature. Semiconducting thermoelectric materials, such as Bi_2Te_3 and SiGe alloys with $zT \approx 1$ are used in low-power cooling and low-power thermoelectric generators, such as beverage coolers and laser diode coolers, and power generators in space missions [10, 13, 37].

1.3.2. Nanostructured thermoelectric materials

Nanostructured thermoelectric materials were introduced in the 1990s after the publication of Dresselhaus et al. that presented routes to tailor the otherwise interconnected physical parameters of S, σ and κ [38]. High zT values can be obtained by high σ, a high S and low $\kappa_{electronic}$ and $\kappa_{lattice}$ of the material. $\kappa_{lattice}$ can be impaired by introducing phonon scattering centres within a material via nanostructuring [27, 28, 39]. Nanostructured materials exist in various forms, such as quantum wells, nanowires, quantum dots and superlattices [39-41]. Fundamentally, these materials can be differentiated based on their dimensionality [32, 42]. Quantum wells are materials that are so thin as to be essentially of two dimensions. Quantum wires, also referred to as nanowires, have significantly small cross-sections and are considered one dimensional (1D). Quantum dots (QDs) are 2-10 nm sized tiny crystals. Charge carriers in QDs are confined in three dimensions. Superlattices are the multiple-layered structure of quantum wells [32]. Artificial boundaries and interfaces in these nanostructures reduce the phonon mean free path and increase diffuse scattering causing a significant reduction in thermal conductivity [43, 44]. However, electron scattering and charge carrier depletion through interface trapping in such systems also impairs electrical conductivity [45, 46]. Electrical conductivity can be controlled by doping while the preferential scattering of low-energy electrons at grain boundaries can potentially enhance the Seebeck coefficient S and hence the power factor $S^2\sigma$ [47-49].

1.4. Synthesis of nanostructured thermoelectric materials

Nanostructured thermoelectric materials can be synthesized by a variety of physical and chemical processes [50]. These methods can be classified under 'top-down' and 'bottom-up' approaches [41, 42]. The top-down approach refers to the reduction of micro and macro scale materials into nanoscale domains. Solid-state synthesis followed by mechanical and melt alloying routes is a usually applied method utilized in this approach [41]. Solid-state synthesis and melting techniques are renowned metallurgical processes. A stoichiometric ratio of high purity elemental components (in powder or compacted form) is heated or melted for long durations to obtain the desired thermoelectric phase [51]. In mechanical alloying, pure elemental micron size powders are ball milled to obtain submicron or nanoscale bulk TE materials [52].

Chemical fabrication methods are mainly bottom-up approaches that allow a more desirable control over a TE material's particle size and morphology by optimizing various parameters. Solvothermal [53], hydrothermal [54], solution co-precipitation [55], sol-gel [56], microemulsion [57], and electrochemical synthesis [58] are well known bottom-up approaches [41, 50]. Solution co-precipitation and solvothermal chemical reactions can produce various TE materials with improved thermoelectric performance [53, 55].

1.5. Mesoporous Silicon (pSi)

1.5.1. Introduction

Accidentally discovered at Bell Laboratories in 1956 [59], pSi gained attention of researchers in 1990s when L. Canham examined its optical properties [42]. Since then, pSi has emerged as a versatile material of interest for fundamental and applied research [60-62]. Silicon penetrated with pores is basically referred to as porous Silicon (pSi). It is classified as micro-, meso- and macro-porous Silicon according to the pore size regimes of $< 2\ nm$, $2 - 50\ nm$ and $> 50\ nm$ respectively based on the IUPAC classification of porous solids [63].

1.5.2. Synthesis routes

There are several routes to synthesize porous Silicon such as stain etching [64], galvanic etching [65], metal assisted etching [66] and E-beam lithography [60, 67]. Approaches such as E-beam lithography yields regular nanostructured surface patterns but demands higher expenditures as

compared to financially feasible methods such as electrochemical anodization [60, 68, 69]. Electrochemically anodized free-standing pSi membranes come with benefits like scalability and a high degree of tunability [17, 70-72]. Anodization parameters allow controlling porosity, pore size distribution, pore connectivity and even pore orientation [69, 73].

1.5.3. Properties and applications

Porous Silicon finds a multitude of potential applications in diverse fields such as optoelectronics, batteries and acoustics [40] [74]. Its biocompatibility makes it interesting for medical and diagnostic applications such as drug delivery and chip-based biosensing [17]. Filters and nanofluidics seek to benefit from the flow dynamics of gases and liquids in the pore network [75]. Huge internal surfaces are interesting for battery anodes and capacitors [76]. Its exceptionally low thermal conductivity allows its integration into thermoelectrics [77]. Other applications include molecular separation [78], bio-sensitivity [79] and tissue engineering [80].

1.5.4. Porous Silicon as a thermoelectric material of interest

Initial work on Silicon nanowires with reported values of $zT \approx 0.5 - 1$ at room temperature motivated the research on pSi as a thermoelectric material of interest [39, 43, 81-83]. PSi combines the Silicon advantages like abundance and processability with a robust and scalable fabrication process. However, in contrast to various reports concerning its application in optoelectronics and as an insulating material, there has been mainly theoretical research on its thermoelectric properties. The theoretical studies of pSi presented by Lee et al. reported a reduction in thermal and electrical conductivity at room temperature by a factor of $2 - 4$ as compared to bulk Silicon [84]. They reported a two-fold increase in the Seebeck coefficient for carrier concentrations less than $2 \times 10^{-19} cm^{-3}$. From the reported results, zT was predicted to increase by two orders of magnitude compared to bulk Silicon. This enhancement of zT was attributed to a significant reduction in thermal conductivity compared to a moderate change in power factor. Experimental results for pSi with 35% porosity synthesized by block-copolymer lithography by Tang et al. reported temperature-dependent zT values of 0.05 at $150K$ to 0.4 at room temperature [85]. Electrical conductivity of around $1000\ S/cm$ at room temperature was reported by Boor et. al. for post-doped pSi samples synthesized by electrochemical anodization [86]. Their pSi samples with 60% porosity exhibited effective thermal conductivity of

7.6 W/mK and zT values around 0.02 at room temperature, lower than 0.4 as reported by Tang et. al.

These are only a few literature examples about thermoelectric properties of pSi probed by macroscopic thermal and electronic measurements. It is essential to have a coherent microscopic picture of charge and heat transport phenomena in pSi. In this context, pSi is discussed in the following sections as thermoelectric material of interest with detailed insights into its macroscopic and microscopic properties.

2. Synthesis of pSi

This chapter introduces electrochemical anodization for the synthesis of pSi. Introduction to the experimental setup is followed by a description of the formation mechanism of pSi. Anodization conditions and their effect on pore size, geometry and porosity of synthesized pSi membranes are summarized. Subsequently, synthesis and chemical post treatment of as-etched pSi membranes is presented as a method to tune the pore size of pSi in the regime of 8-25 nm.

2.1. Electrochemical anodization

Electrochemical etching of single crystalline bulk Silicon in hydrofluoric acid (HF) based electrolytes is the most extensively used method for the synthesis of pSi [61, 68, 69, 72].

2.1.1. Electrochemical anodization setup

Anodization can be carried out using an HF-resistant container, electrodes and power supply. For an electrochemical reaction to occur, two electrodes are needed. One supplies electrons to the electrolyte solution (the cathode), and the other removes electrons from the solution (the anode). Fig. 2-1 presents a schematic of a two-electrode Silicon anodization cell.
The cell body itself is made of an HF/organic solvent-resistant polymer, i.e. Teflon®, in which the electrolyte is placed. An HF resistant and electrically conductive material (Platinum in this case) is immersed in the electrolyte and serves as the cathode. In this configuration, a backside contact is used. Practically, the surface of the Si wafer, which is anodized, is the one that is in contact with the electrolyte, while the opposite side is placed in contact with a metallic plate (commonly Al). It serves as an anode, and thus the electrical circuit is closed. The two sides are isolated with an O-ring, and thus the electrolyte cannot reach the metallic backside contact. The O-ring is composed of HF and organic solvent resistant material, namely Viton®.

2.1.2. Etching parameters

The most important etching parameters are the HF concentration, current density and etching time. With the appropriate resistivity and crystallographic orientation of the used silicon wafers, it is possible to control pore sizes, porosity and inter-connectivity of the etched pore networks [69].

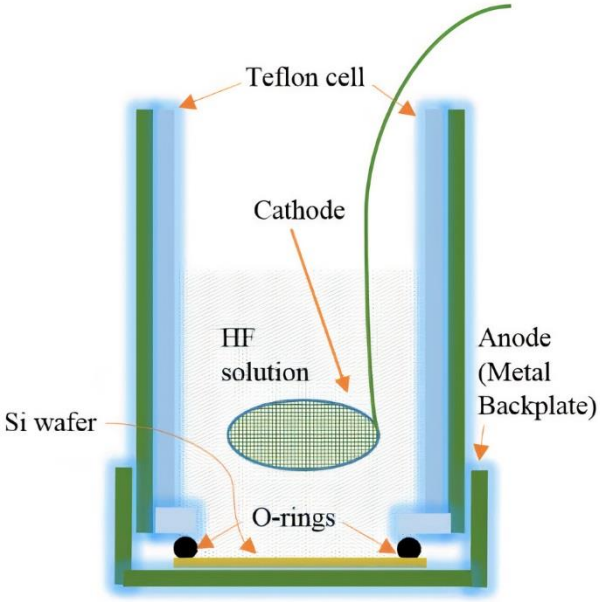

Fig. 2-1 Schematic of a two-electrode Silicon anodization cell.

Table 2-1. summarizes important parameters and their effect on pore size, porosity and etching rate of electrochemically etched pSi [62]. The resulting structure of pSi depends on the doping concentration of the Silicon substrate. More specifically, by anodizing highly doped Si substrates, vertical pores with dendritic–like structure are formed [87]. On the other hand, if the starting Silicon wafer is lightly doped, the pSi formed has a sponge-like structure [40, 69]. The latter material is homogeneous (with both pore diameter and inter-pore spacing typically 2-5 nm) and isotropic in structure [88, 89]. An increase in the applied current density during etching results in pSi membranes with higher porosity and larger pores. A decrease in the concentration of HF in the electrolyte leads to higher porosities of the resulting porous Si membranes. The etching rate in Table 2-1 refers to the increase in Psi membrane thickness per unit time.

Table 2-1. Effects of key parameters on pSi formation

Increased Yields ➔ ⬇	*Porosity*	*Pore Diameter*	*Etching Rate*
HF Concentration	Decreased	Decreased	Decreased
Current Density	Increased	Increased	Increased
P type doping	Decreased	Decreased	Increased
N type doping	Increased	Increased	Increased
Etching time	Increased	Increased	Almost constant

In the current work, pSi samples were synthesized by electrochemical anodization of p-type (boron doped), [001] oriented Silicon wafers with a resistivity of $0.01 - 0.02\,\Omega cm^{-1}$. Columnar pore channels (with $6 - 10\,nm$ sized pore diameter), along the [001] crystallographic direction, were grown by exposing the wafer to an electrolyte composed of HF and ethanol [HF (48%): Ethanol (99.9%) → 4:6, 6:4 volumetric ratio] utilizing an etching current density of $j = 12\,mAcm^{-2}$. Subsequently, after $4 - 6h$ of anodization, an increased current density of $j = 132\,mAcm^{-2}$ was applied for $60s$ to detach $160 - 250\,\mu m$ thick free standing pSi membranes from the supporting bulk Silicon wafers in a final lift-off step.

2.2. Formation mechanism of pSi

Dissolution of bulk Silicon and formation of pSi involves a series of electrochemical reactions [90] schematically illustrated in Fig. 2-2. Overall process of pSi formation can be expressed by an anodic reaction as:

$$Si + 4HF_2^- + h^+ \rightarrow {SiF_6}^{2-} + 2HF + H_2 + e^- \qquad (2.1)$$

The Si-H bonds passivate the silicon surface. Injection of the holes (h^+) from the bulk Si to its surface causes a nucleophilic attack of the fluorine anions on Si-H bonds and the formation of the Si-F bonds. Two hydrogen atoms combine consequently injecting an electron into the Silicon substrate. Polarization effect caused by the Si-F bonds leads to the nucleophilic attack by another fluorine anion that replace the second hydrogen atom. The Si-F bonds' induced polarization cause the reduction of an electron density of the remaining Si-Si bonds. It makes them susceptible to the second nucleophilic attack by the fluoride anions causing the formation of Silicon tetra fluoride SiF_4. It further reacts with hydrofluoric acid to form stable a fluoro-

anion SiF_6^{2-}. Overall, the reaction pathway cause the local removal of Silicon atoms forming pores at the regions where the concentration of holes is high.

As the pore-wall thickness decreases, its resistance to hole transport increases. At a critical pore-wall thickness (typically a few nanometers for p-doped silicon), propagation of holes along thin silicon filaments (pore-walls) become less favourable than their propagation into the bulk Silicon wafer. The increased band gap resulting from quantum confinement causes holes to go out of pore walls into the bulk Silicon wafer. At higher current density, pore diameter increases cutting through the pore walls in a final lift-off step, detaching pSi membrane from the bulk Silicon wafer.

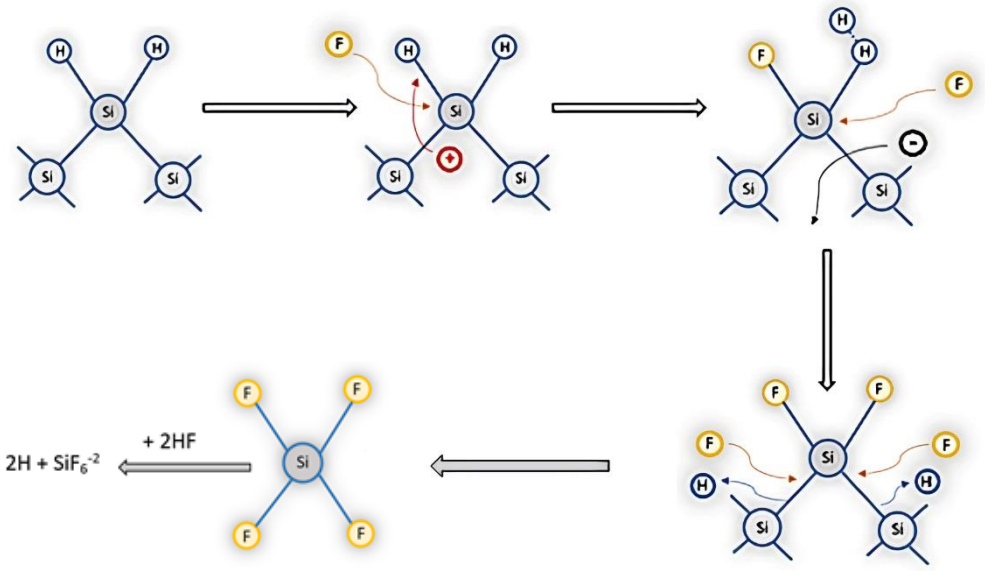

Fig. 2-2 Porous Silicon formation mechanism via anodization of Silicon in HF-based electrolyte.

2.3. Chemical post-processing of as-etched pSi

A subset of as-etched samples were post-treated at room temperature to increase the pore diameter. The post-treatment procedure developed in my work was an extension of the work of Kumar et al. [73]. In the cited reference, the membranes were exposed for several hours to hydrogen peroxide and hydrofluoric acid, a cyclic approach was used in the current work. Porous membranes were repeatedly bathed in H_2O_2 (98%) and HF (48%) each time for 30 minutes (1 cycle). H_2O_2 oxidizes the branchy pore walls. The HF subsequently dissolves the formed SiO_2. Stopping chemical post treatment after 3-, 6- or 9-cycles, results in different samples with varying pore diameter, porosity and specific surface.

3. Characterization techniques

This chapter first presents the measurement techniques used to probe the morphology of synthesized pSi membranes. Furthermore, the employed macroscopic characterization methods are explained together with their fundamental principles and measurement parameters.

3.1. Scanning electron microscopy (SEM)

SEM was utilized as a local probe to elucidate morphological characteristics of as-prepared mesoporous membranes. The SEM LEO Gemini microscope was used to obtain surface and cross-sectional images of pSi membranes. SEM microcgraphs of a porous membrane (Fig. 3-1) show in a top view the surface morphology without depth information and in a side view a small part of the pore cross section.

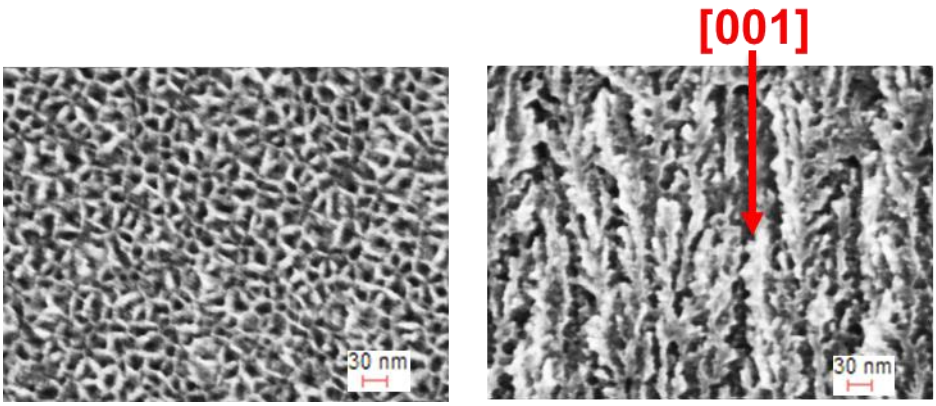

Fig. 3-1 SEM micrographs of pSi obtained from SEM LEO Gemini microscope employing 15kV energy with magnification of 400KX. The scale bar represents 30 nm. (Left) Top view of the pores in etched silicon. (Right) Side view of pores.

SEM surface and cross-sectional image of synthesized membranes illustrate polygonal-shaped pore growth along the [001] direction with dendritic branches. The top view exhibits a sponge-like densely distributed porous structure without long-range order. It allows the determination of the pore size distribution by using a dedicated image analysis algorithm [91]. It identifies the pores' polygonal contour lines and utilizes the enclosed area to calculate the equivalence radius of a circular pore. The resulting pore size distribution (PSD) is shown in the Fig. 3-2. The pore size here refers to the pore radius. Close inspection of PSD's obtained from the etched and back-

side of the membrane shows variation in average radius up to 50% as compared to etched side. Detaching pSi membrane at higher current density increases the pore radius on the backside [2].

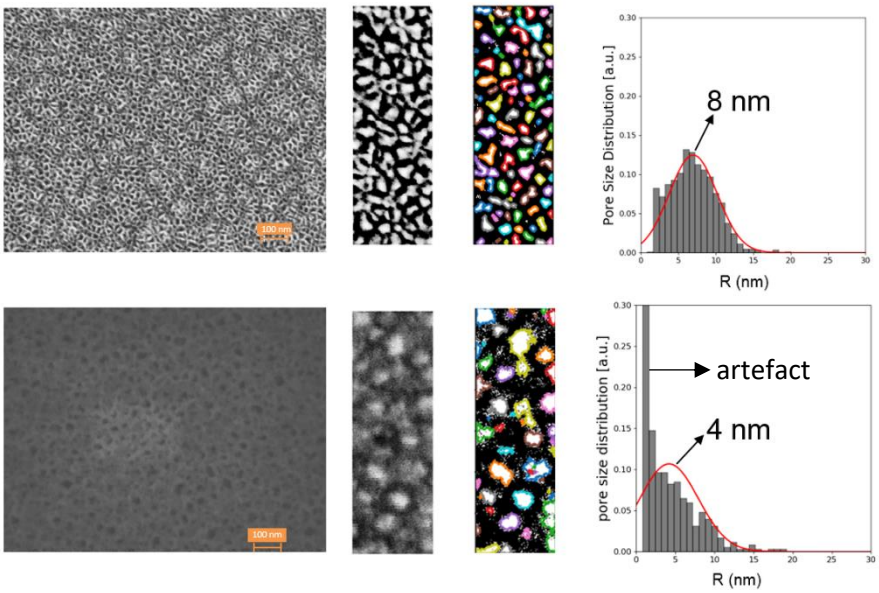

Fig. 3-2 SEM micrographs and the respective binary images of back-side of pSi (Top) and etched-side of pSi (Bottom), Pore contouring and obtained pore size distributions for both sides of pSi sample are presented (Right). The red line represents average PSD. The scale bars in the SEM images present 100 nm. An artefact due to pore-contouring at the edge of the SEM image is marked.

3.2. Sorption isotherm

The pore structure information in porous silicon is essential for controlling its structure and understanding its formation mechanism. One of the most widely used, robust methods of structural characterization of porous, especially mesoporous, materials are the measurements of sorption isotherms. Utilizing this technique, one may obtain information of internal specific surface, pore size distribution, and, under certain conditions, details of the pore space geometry [92]. It can be probed gravimetrically, volumetrically, or by optical reflectivity experiments [93, 94]. Thermoporometry has also emerged as an experimental method for structural characterization of mesoporous materials that complement sorption isotherm [95].

The gas sorption technique relates to the adsorption of nitrogen (or, less commonly, argon, xenon or krypton), at cryogenic temperatures, via adsorption and capillary condensation from the gas phase and subsequent desorption after complete pore filling. An adsorption-desorption isotherm is formed based on the relationship between the adsorbate gas pressure and the

adsorbed/desorbed gas volume. The Nitrogen sorption measurement technique was used to determine pore volume and pore size distribution of pSi membranes. It measures volumetrically the total uptake of liquid nitrogen $f = N/N_0$ in the pores as function of the reduced pressure $P_{red} = P/P_0$ at fixed temperature $T = 77\ K$. N and N_0 relate here to the number of molecules physisorbed in the pores respectively required to fill the entire pore space whereas P and P_0 refer to the nitrogen vapor pressure below and at saturation ($P_0(77K) = 1013\ mbar$). The characteristic dependence of filling fraction f on reduced pressure P_{red} relates to physisorption of molecules on the pore walls at low pressures and capillary condensation in the pore centers at higher pressure.

The sorption behavior of synthesized pSi sample is illustrated in Fig. 3-3 together with schematics of sorption phenomena occurring in the pore. At lower relative pressure, the sorption mechanism is comparable to that on plane surfaces [93]. Region A shows multilayer adsorption. After reaching a critical film thickness at B, region B-C indicates capillary condensation in the pore centers. The plateau near C indicates complete filling of the pores. Evaporation takes place at a pressure less than the pore condensation pressure (region D). Region E shows closure of the hysteresis loop corresponding to the adsorbed multilayer film in equilibrium with a vapor in the pore center.

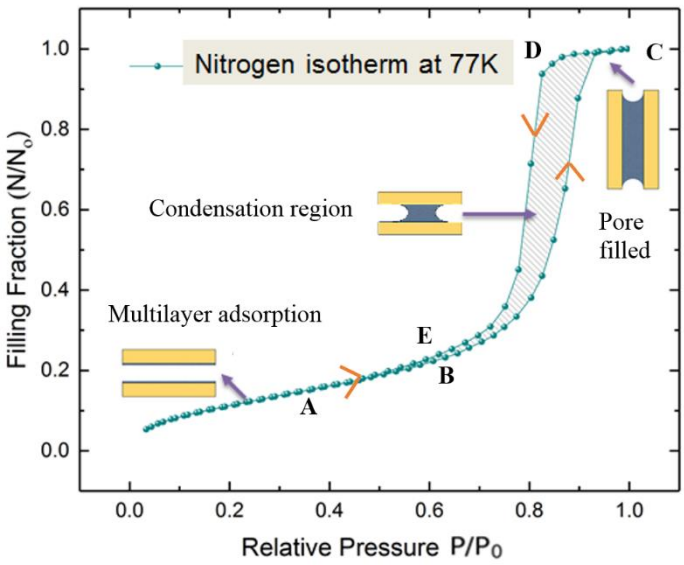

Fig. 3-3 Typical data presenting multilayer adsorption, pore condensation and hysteresis in mesoporous silicon.

The Kelvin equation relates the pore radius to the relative vapour pressure at which condensation occurs:

$$RTln\,{}^{P}/_{P_o} = \frac{-2\gamma\overline{V}}{r_m} \tag{3.1}$$

where r_m is the radius of liquid adsorbate's meniscus, P refers to equilibrium vapor pressure of a curved meniscus of liquid in capillary/pore, P_o is equilibrium pressure of bulk liquid , γ is surface tension of the liquid, $\overline{V}$ refers to molar volume of condensed liquid in the pore and the universal gas constant $R = N_A \times k_B$ where N_A is Avogadro's number (6.02×10^{23}molecules/mol) and k_B is Boltzmann constant ($1.38 \times 10^{-23} J/K$).

The pore radius $r_p = r_m + t_a$ where t_a refers to the surface adsorbed layer's thickness (monolayer or multilayer, before pores filling). This model assumes that the liquid completely wets the pores. The smaller the pore radius, the lower the relative pressure at which condensation can occur at a given temperature [63, 93]. The Barrett-Joyner-Halenda (BJH) method relies on a systematic analysis of the desorption based on the Kelvin equation [93, 96]. The BJH analysis of the desorption measurements identifies an average pore radius of r = 4 nm for the synthesized pSi membranes.

The Brunauer-Emmet-Teller (BET) method is an extensively used procedure to determine surface area of solid materials [97]. It involves utilizing the BET equation [92, 93, 97]:

$$\frac{1}{M_{ads}\left(\left({}^{P_o}/_{P}\right) - 1\right)} = a + m\left({}^{P}/_{P_o}\right) \tag{3.2}$$

where M_{ads} refers to the specific amount of nitrogen adsorbed in mol/g at P/P_0 . Linear BET plot of $\frac{1}{M_{ads}\left(\left({}^{P_o}/_{P}\right)-1\right)}$ vs ${}^{P}/_{P_o}$ restricted to a limited adsorption isotherm regime in the P/P_0 range of $0.05 - 0.35$ (for nitrogen isotherm) allows the extraction of the slope $m = \frac{c-1}{v_m \times c}$ and intercept $a = \frac{1}{v_m \times c}$. c is BET constant and v_m refers to monolayer absorbed gas volume. Numerical values of slope m and intercept a are utilized to solve for v_m and c. Specific and total surface area $A_{specific/total}$ is calculated via Eqn. 3.3

$$A_{specific} = {}^{A_{total}}/_{m_{sample}} \quad , \quad A_{total} = {}^{v_m N_A A_{cs}}/_{V} \tag{3.3}$$

where m_{sample} refers to the sample's mass, N_A is the Avogadro's number, V refers to molar volume of adsorbed gas and A_{cs} denotes cross-sectional area of adsorbate molecule (i.e $\sim 16.2 Å^2$ for nitrogen).

$A_{specific} = 157\ m^2/g$ was inferred from a Brunauer-Emmet-Teller analysis [93, 97] of the low-pressure part (multilayer regime) of the isotherm (Figure. 3-3) before onset of capillary condensation membrane volume and N_0 allow finally a porosity estimate of 50%.

3.3. Inelastic neutron scattering

Neutrons are particularly suitable for measurements of excitations because both their energy and wavelength can be simultaneously matched to the sample's energy and length scales. Thermal neutrons which have a wavelength (~ 2 Å) similar to inter-atomic distances have an energy (20 meV) similar to elementary excitations in solids. This allows simultaneous information on the structure and dynamics of materials to be obtained and to measure dispersion relation $\hbar\omega(\vec{q})$ of excitations.

When neutrons are incident on a sample they can be transmitted, scattered or absorbed by the sample: Scattered neutron pattern is a specific function of angle 2θ that is characteristic of the the sample's structure. During the scattering process the neutron energy is either unchanged or it is gained or lost by the sample. The atom can recoil during the collision with the neutron in which case the neutron loses energy and the sample gains energy. Alternatively, if atom is already moving e.g. a phonon vibration, it transfers this energy to the neutron, the neutron gains energy and the sample loses energy. Elastic neutron scattering is when the neutron energy is unchanged. Inelastic neutron scattering occurs when the neutron gains or lose energy in the scattering process.

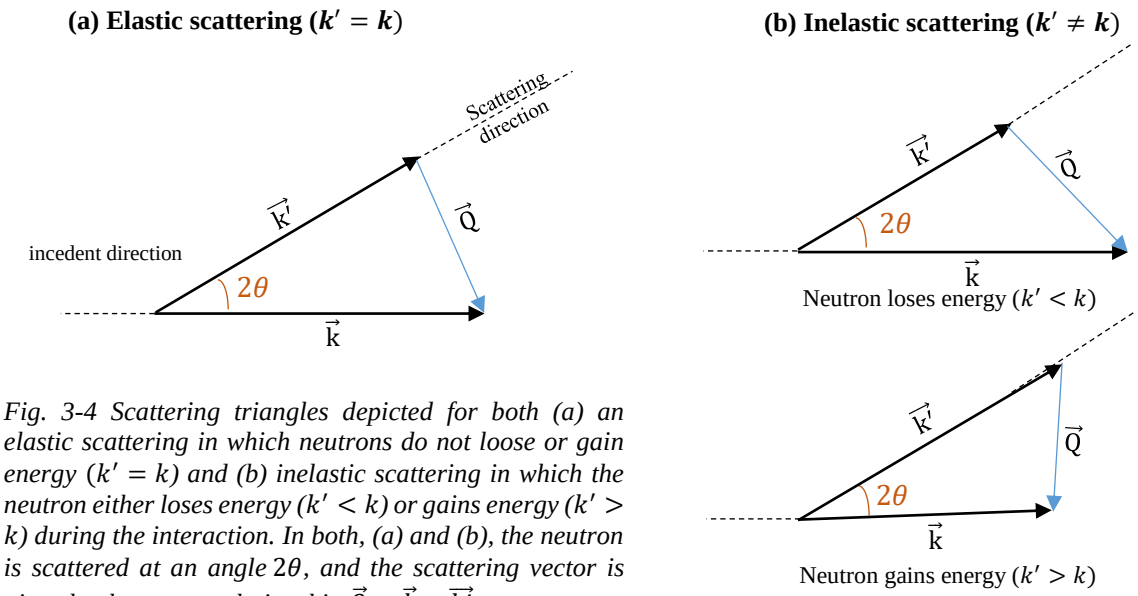

Fig. 3-4 Scattering triangles depicted for both (a) an elastic scattering in which neutrons do not loose or gain energy ($k' = k$) and (b) inelastic scattering in which the neutron either loses energy ($k' < k$) or gains energy ($k' > k$) during the interaction. In both, (a) and (b), the neutron is scattered at an angle 2θ, and the scattering vector is given by the vector relationship $\vec{Q} = \vec{k} - \vec{k'}$.

The collective motion of the lattice is a phonon. Their energies are quantized with each phonon having an energy $\hbar\omega$ where ω refers to the atomic motion frequency associated with that phonon. Energy transfer between neutrons and phonons gives rise to neutrons' inelastic coherent scattering in which the neutron energy before and after the scattering process varies by an amount equal to phonon energy.

Inelastic neutron scattering data is collected with PUMA, a thermal triple-axis spectrometer at the high-flux neutron research reactor FRM II in Garching, Germany. It is designed to probe the scattering function $S\ (\vec{Q}, \omega)$ of elementary excitations such as phonons and magnons in single-crystalline materials. Excitations with energies up to $\hbar\omega = 100$ meV and wavevectors of $|\vec{q}| = 12$ Å^{-1} can be measured.

All scattering experiments were performed at room temperature. Two types of scans were utilized to measure the phonon energy versus phonon wavevector dispersion relation $\hbar\omega(\vec{q})$ in pSi and bSi along well-defined crystallographic directions. So-called constant-energy scans measure the intensity of scattered neutrons with fixed energy loss for different wavevector transfers $\vec{q}$ as depicted in Fig. 3-5. They are suited to probe the low energy dispersion where the phonon energy $\hbar\omega$ depends strongly on the probed phonon wavevector $\vec{q}$. So-called constant-$\vec{q}$ scans record the neutrons depending on the energy loss $\hbar\omega$ at fixed wavevector transfer $\vec{q}$. They are typically performed closer to the boundary of the Brillouin zone where a weak $\omega(\vec{q})$ dependence is evident. PUMA measures neutrons with a fixed final wavevector

$|\vec{k}_f| = 4.11$ Å^{-1} and varies the incident wavevector $\vec{k}_i$ for the constant-$\vec{q}$ scans. For the constant-energy scans both $|\vec{k}_i|$ and $|\vec{k}_f|$ are fixed. Representative scans obtained from PUMA are shown in Fig. 3-6.

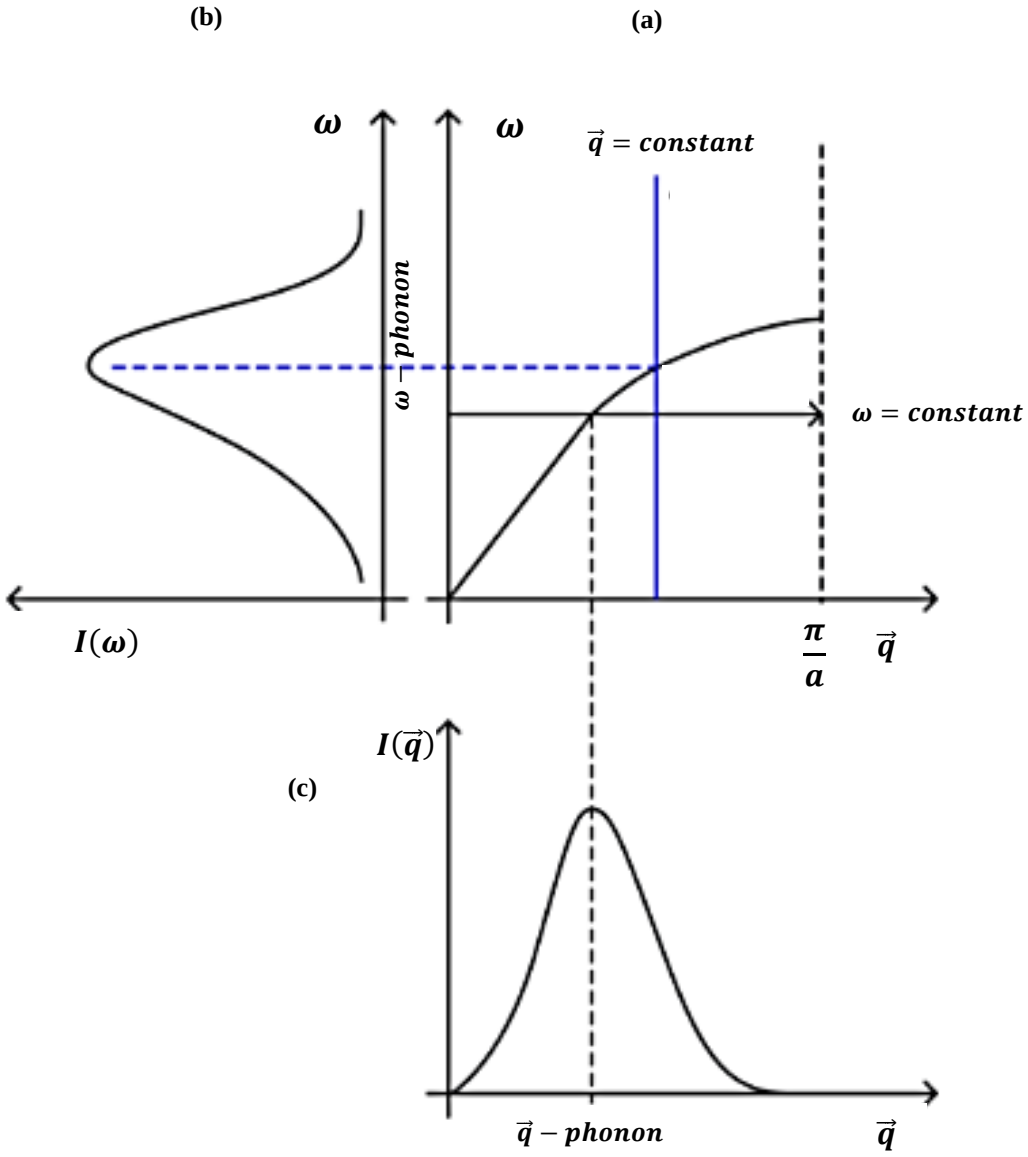

Fig. 3-5 Pictorial illustration of a neutron scattering experiment where (a) the phonon dispersion $\omega(\vec{q})$ is probed vertically ($\vec{q} = constant$) and horizontally ($\omega = constant$). (b)+(c) depicts the neutron intensity I against ω for the probed dispersion regions. Constant-ω scans probe the low energy dispersion whereas constant-q scans probe dispersion closer to the Brillouin zone boundary.

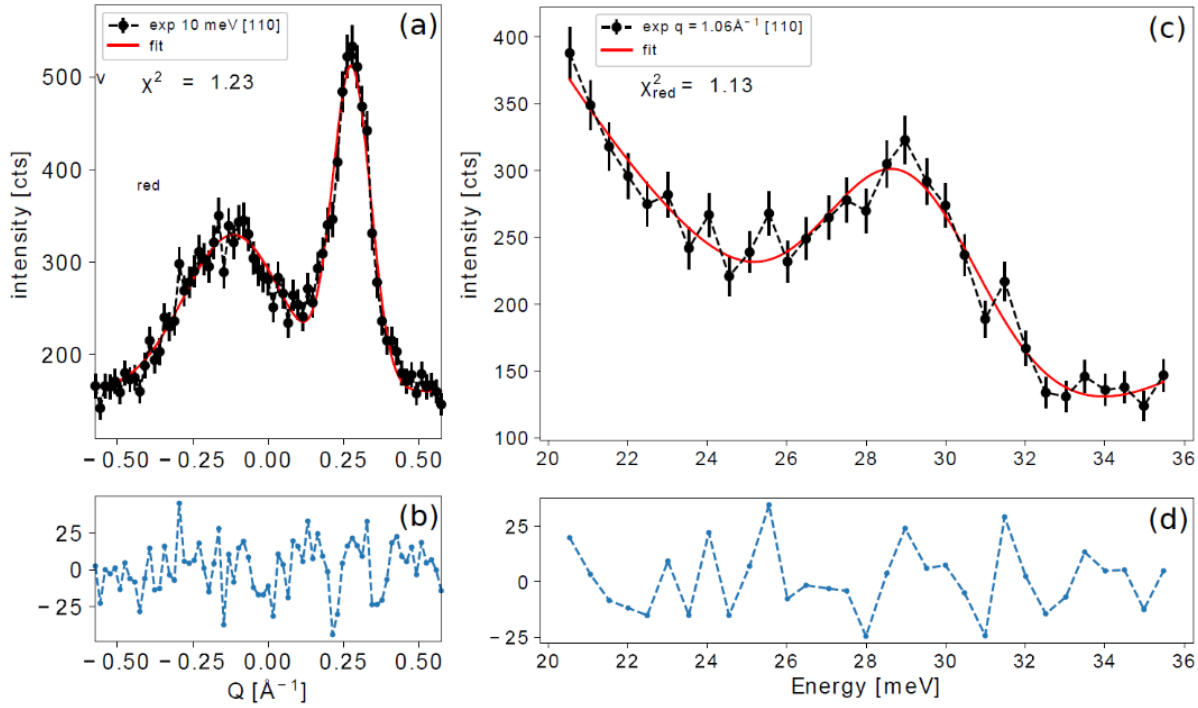

Fig. 3-6 (a) A 10 meV transverse phonon is evident in a q-scan along the [110] direction that is measured around the (004) Bragg reflection (black symbols). The instrumental configuration of the triple-axis spectrometer PUMA probes the phonon in a defocusing condition (q < 0) and a focusing condition (q > 0). Non-linear least squares fitting employing two Gaussians is utilized to extract the wave-vector q of the 10 meV phonon (red line) ***(c)*** *For a wavevector transfer of q =1.06 Å^{-1} the [110] transverse phonon is evident in an ω scan for an energy transfer of approximately 28 meV. Non-linear least squares fitting employing one Gaussian and a polynomial background is utilized to extract the energy of the phonon (red line) (b) + (d) Residual between non-linear least squares approximation and the data.*

The neutron scattering experiments are conceived to elucidate phonons along high symmetry directions in the Brillouin zone of Silicon as depicted in Fig. 3-7. Probed are specifically $\overline{\Gamma L}$, $\overline{\Gamma K}$ and $\overline{\Gamma X}$ directions. All information about the phonon dispersion are contained within the first Brillouin zone and depend solely on the reduced phonon wavevector $\vec{q}$ [98]. However, inelastic scattering of neutrons on phonons increases with the absolute wavevector transfer $\vec{Q} = \vec{Q}_{Bragg} + \vec{q}$ [99] between neutron and lattice. Consequently, phonons are best measured in the highest instrumentally accessible Brillouin zones to maximize scattering intensity and consequently to improve signal-to-noise ratios.

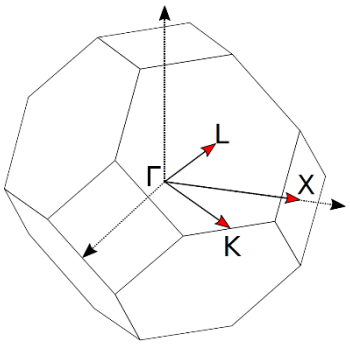

Fig. 3-7 First Brillouin zone of a fcc lattice: Dotted arrows mark the cubic [100] directions. Red arrows show the high symmetry directions.

3.4. Electrical conductivity and Seebeck measurements

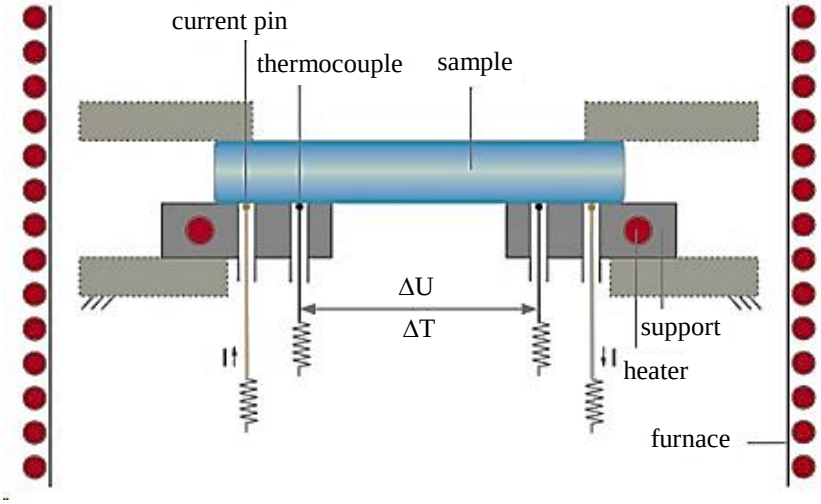

Fig. 3-8 Measurement setup of the Netzsch SBA 458 Nemesis®

Temperature-dependent electrical conductivity and Seebeck coefficient for as-etched and post treated pSi samples were measured simultaneously using the NETZSCH SBA-458 system in the temperature range from $300K$ to $773K$ in helium atmosphere. The device's measurement part contains four pins linearly in contact with the sample's lower surface that faced the electrolyte during synthesis, as shown in Fig 3-8. Two outer rhodium pins inject current through the sample while Inconel covered type K thermocouples measure voltage.

This four-point probe configuration enables the measurement of in-plane electrical conductivity with maximum current of $1\ mA$. The thermopower is determined from the voltage drop across

the thermocouples and temperatures measured at the thermocouples with a thermal gradient $\Delta T < 7.5K$ created by successive heating of both sample holder sides. The main drawback of the two-point probe technique is the contact resistances. Mainly, the measured resistance includes the contact resistances, which introduces significant errors. Thus the obtained resistivity value is much less accurate. However, this uncertainty can be surmounted using the four-point probe method.

The value of determined S is positive for p-type semiconductors or negative for n-type semiconductors, where the transport carriers are holes or electrons, respectively. Fig. 3-9. presents temperature dependent electrical conductivity and Seebeck coefficient of pSi membranes

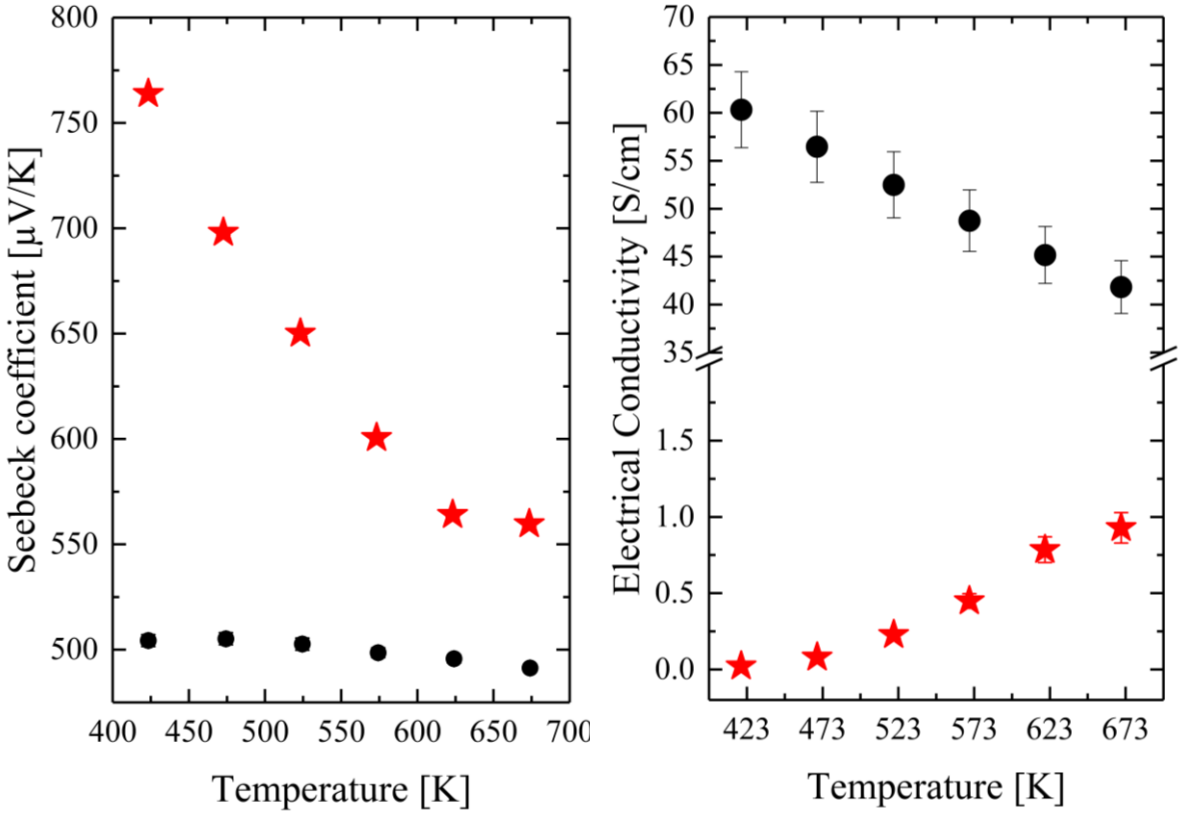

Fig. 3-9 Temperature dependent Seebeck coefficient and electrical conductivity of as-etched pSi samples (red stars) and bulk Silicon (black circles). For some data points, error bars are of a similar size than the symbols.

3.5. Heat capacity measurements

The Quantum design physical property measurement system (PPMS) was utilized to measure heat capacity C_p in the temperature range of $2K - 380K$ at a constant pressure.

$$C_p = \left(\frac{\delta H}{dT}\right)_p \tag{3.4}$$

H refers to enthalpy in Eqn. 3.4. The heat capacity option of PPMS utilizes a relaxation technique proposed by Hwang et al. [100]. The heat capacity sample holder uses the standard PPMS 12-pin format for electrical connections, and it contains a small microcalorimeter platform for mounting the sample. PSi samples were mounted to this platform by a standard cryogenic Apiezon grease that also acts as a heat transfer material between the sample and the platform. Eight thin wires serve as the electrical leads for an embedded heater and thermometer connected to the sample platform. The measurement involves heating the sample for a fixed time followed by cooling for the same time duration. The sample's entire temperature response is fitted to a model that considers both (i) the sample platform's thermal relaxation to the bath temperature and (ii) the relaxation between the sample platform and the sample itself. The latter is considered in case of the poor thermal connection between the sample and the platform. This modelling ensures correct heat capacity values despite poor thermal contact.

PPMS software utilises two thermal models, the one-tau model and the two-tau model, to fit the temperature response curve. The one-tau model treats the sample and the platform (on which the sample is mounted) as one system, whereas in the two-tau model, a heat flow between the sample and the platform is considered as well.

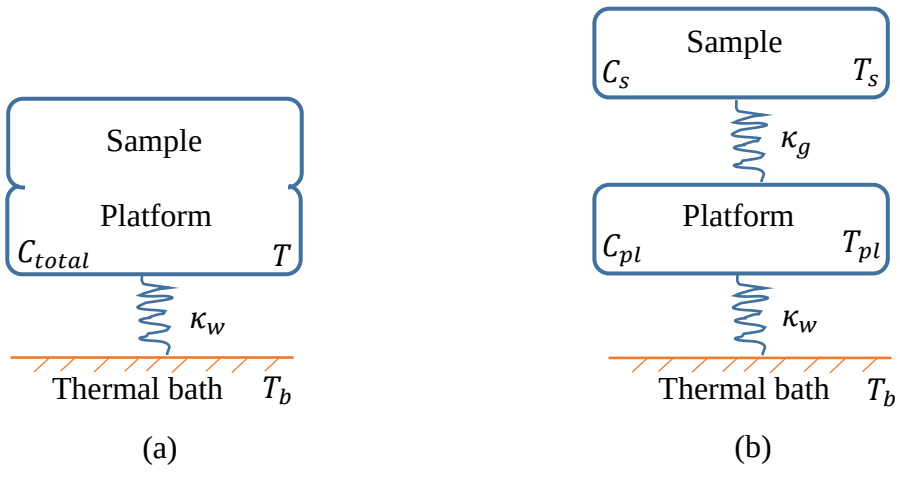

Fig. 3-10 Heat flow diagram for (a) One-tau model where C_{total} is the heat capacity of the whole system and κ_w denotes thermal conductivity of the wires. T_b is the bath temperature. (b) Two-tau model where κ_g is the thermal conductivity of the grease. C_{pl}, T_{pl} and C_s, T_s are the heat capacity and temperature of the platform and sample respectively.

In one-tau model, the temperature T of the whole system as a function of time t obeys the Eqn. 3.5.

$$C_{total}\frac{dT}{dt} = -\kappa_w(T - T_b) + P(t) \tag{3.5}$$

where C_{total} is the total heat capacity of the sample and sample platform, $P(t)$ is the power of the heater, κ_w is the thermal conductivity of the supporting wires and T_b is the bath temperature. A constant power P is applied during the heating part of the measurement and is kept zero during the cooling part. The differential Eqn. 3.5 is solved for $T(t)$ as:

$$T(t) = \begin{cases} \dfrac{P\tau\left(1 - e^{-t/\tau}\right)}{C_{total} + T_b} & 0 < t < t_0 \\ \dfrac{P\tau\left(1 - e^{-t_0/\tau}\right)e^{-(t-t_0)/\tau}}{C_{total} + T_b} & t > t_0 \end{cases} \tag{3.6}$$

where $\tau = {C_{total}}/{\kappa_w}$ is a characteristic time constant.

In Eqn. 3.6, the first line describes the heating part. At $t = 0$, the heater is turned on, and the temperature increase till the temperature $T_b + 2\%$ is reached at time $t = t_0$. Subsequently, the heater switches off, and the bath temperature is attained again, described by the second line. In the one-tau model, the sample's heat capacity is the difference between the measured heat capacity with and without the sample.

The two-tau model is used by the PPMS software when the sample has a poor thermal contact with the platform. The following equations govern the two-tau model:

$$C_{pl}\frac{dT_{pl}}{dt} = P(t) - \kappa_w\left(T_{pl}(t) - T_b\right) + \kappa_g(T_s(t) - T_{pl}(t)) \tag{3.7}$$

$$C_s\frac{dT_s}{dt} = -\kappa_g(T_s(t) - T_{pl}(t)) \tag{3.8}$$

where C_{pl} is the platform's heat capacity, $T_{pl}(t)$ and $T_s(t)$ are the temperatures of the platform and sample, respectively, κ_g is the thermal conductivity of the grease, and C_s is sample's heat

capacity. The choice of model by the software is based on the fit deviation of the two models. In our experiments, the data is obtained by one-tau model.

3.6. Thermal conductivity measurements

Thermal conductivity data was measured in the temperature range from $2K$ to $670K$. The PPMS setup was used to determine in-plane thermal conductivity in a temperature range of $2K$ to $380K$. For a higher temperature range of $300K - 670K$, laser flash analysis (LFA) was used to measure the thermal diffusivity that further enables the calculation of temperature-dependent cross-plane thermal conductivity.

3.6.1. Physical property measurement system (PPMS)

For conducting the PPMS measurement, the pSi sample is placed between a heat source and a heat sink. The sample is heated via current heat from a heater with known steady-state power. The temperature difference ΔT as a function of time t across a given length L of the sample is modelled as follows:

$$\Delta T_{model,heating} = \Delta T_{\infty} \times \left[1 - \frac{\left[\tau_1 \times exp\left(-\frac{t}{\tau_1}\right) - \tau_2 \times exp\left(-\frac{t}{\tau_2}\right)\right]}{\tau_1 - \tau_2}\right] \tag{3.9}$$

where ΔT_{∞} is the expected steady state value, τ_1 and τ_2 are long and short thermal time constants respectively, in seconds (τ_1 for the sample and τ_2 for the environment).
Subsequently, the thermal conductivity κ of the sample is calculated via Fourier's law of heat conduction:

$$\kappa = \frac{QL}{A\Delta T} \tag{3.10}$$

$$Q = P - Q_{loss} \tag{3.11}$$

where Q is the amount of heat passing through the sample, A is the sample's cross-sectional area, L and ΔT refer to the distance and temperature difference between thermometers respectively. $P = I^2R$ is the applied heating power via heat source. The sample is heated via application of current I through the heater with known resistance R. $Q_{loss} = \sigma_T \times \left(\frac{S}{2}\right) \times \varepsilon \times$

$(T_{hot}^4 - T_{cold}^4)$ denotes heat losses due to radiation from the sample. S is the sample surface area, ε is the infrared emissivity, T_{hot} and T_{cold} are average temperatures of the hot and cold thermometers respectively. $\sigma_T = 5.67 \times 10^{-8} W m^{-2} K^{-4}$ is the Stefan-Boltzmann constant. The $\frac{1}{2}$ factor is due to the approximation that only half of the sample radiates at hot temperature, while the other half is at cold temperature. Infrared emissivity = 1 was employed as an approximated value suggested for nonmetallic sample surface in the PPMS manual.

Fig. 3-10 shows example plots of temperature dependent specific heat capacity and thermal conductivity of pSi sample and corresponding bulk Si reference sample. Distinct thermal transport properties of pSi as compared to bulk Silicon is evident in Fig. 3-10.

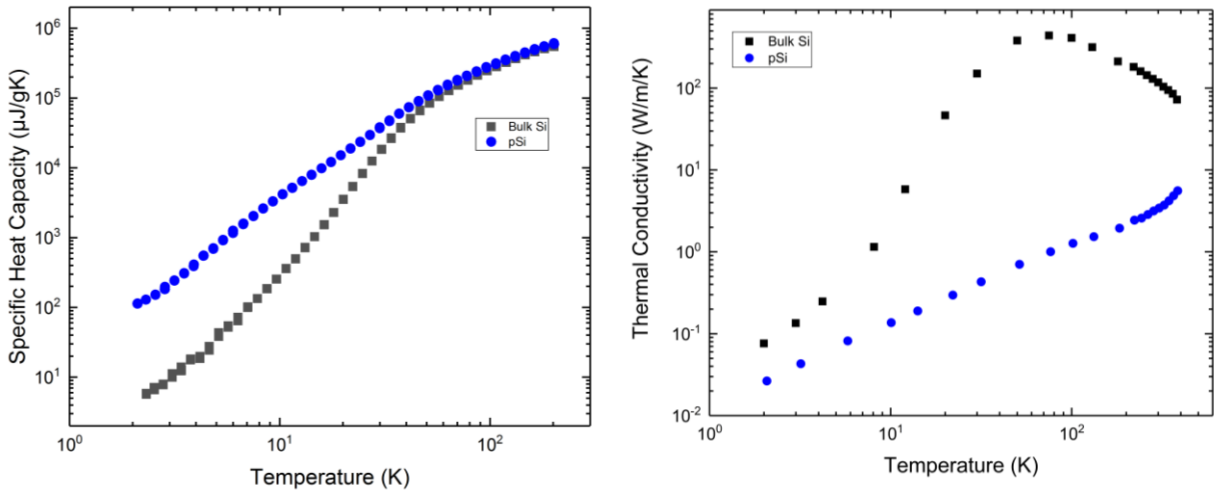

Fig. 3-10 Temperature dependent specific heat capacity and thermal conductivity of pSi samples and bulk Si obtained from PPMS measurement.

3.6.2. Laser flash analysis (LFA)

The laser flash analysis (LFA) method was used to measure temperature dependent thermal diffusivity $\alpha(T)$ followed by thermal conductivity κ calculation. The thermal diffusivity $\alpha(T)$ is a material-specific property defined as the rate of temperature spread through a material.
The sample is placed on a sample robot, which is enclosed by a furnace. For the measurement, the furnace is held at a predetermined temperature. A programmable laser pulse ($\leq 1\ msec$) irradiates one side of the sample, resulting in a temperature rise at the opposite side. A high-speed IR detector measures the resulting temperature rise of the opposite side of the sample. Thermal diffusivity is computed from the ΔT vs time t data.

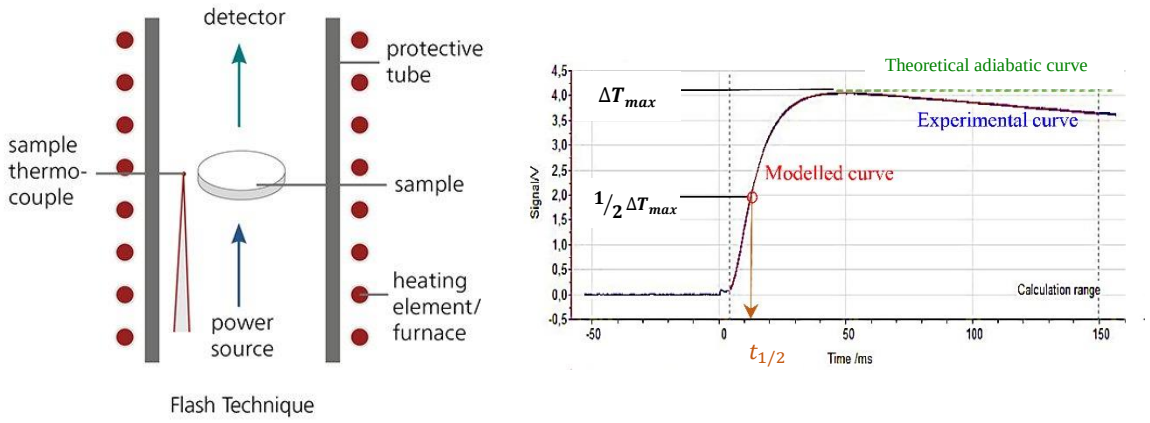

Fig. 3-12 (Right) LFA-457 measurement principle and (Left) obtained signal curve (V against t*)* where $\Delta T \propto V$. *Red line represents Cape-Lehmann and laser pulse correction model-fit*

Various thermal models exist for this purpose, including the original model by Parker et al. [101] and its refined versions by Cowan and Cape and Lehman [102]. In the Parker's model, the sample's thermal diffusivity is calculated based on only one parameter of the temperature curve - the time $t_{1/2}$ in which the reverse-side temperature reaches one-half of its maximum value. Thermal diffusivity is related to the sample thickness d and the half time $t_{1/2}$ as:

$$\alpha = 0.1388 \frac{d^2}{t_{1/2}} \tag{3.12}$$

Parker's model assumes an isotropic and adiabatic sample (with no heat loss during the measurement). Other assumptions include infinitely short pulse time and that the total radiation is absorbed in the thin layer of material near the surface. Since this method assumes ideal conditions of adiabatic sample and rapid pulse heating, it is somewhat limited in applicability. Other methods make it more suitable to experimental conditions, which consider heat losses, finite pulse duration, non-uniform pulse heating, and composite structures [101-104]. For example, Cowan added the correction regarding heat losses from both the sample's upper and lower surfaces [105]. Cape and Lehman analyzed the effects of radiation at high temperatures, the finite duration of the heating pulse, and the feasibility of low-temperature measurements [102]. The Cape-Lehmann model together with laser pulse correction model was used in the current work to determine the thermal diffusivity of pSi samples. It was followed by a thermal conductivity calculation by the following equation:

$$\kappa = \alpha(T) C_p(T) \rho_{pSi} \tag{3.13}$$

where $C_p(T)$ is temperature dependent specific heat of the sample measured from differential scanning calorimetry and ρ_{pSi} is the density of pSi sample with respect to bulk Silicon density ρ_{Si} and porosity φ (as determined from sorption measurements) of pSi sample as:

$$\rho_{pSi} = (1 - \varphi)\, \rho_{Si} \tag{3.14}$$

Fig. 3.13 presents temperature dependent thermal conductivity of pSi and p-doped bulk Si reference obtained from LFA measurement. Upon nanostructuring, pSi shows a reduction in thermal conductivity of about two orders of magnitude as compared to p-doped bulk Si.

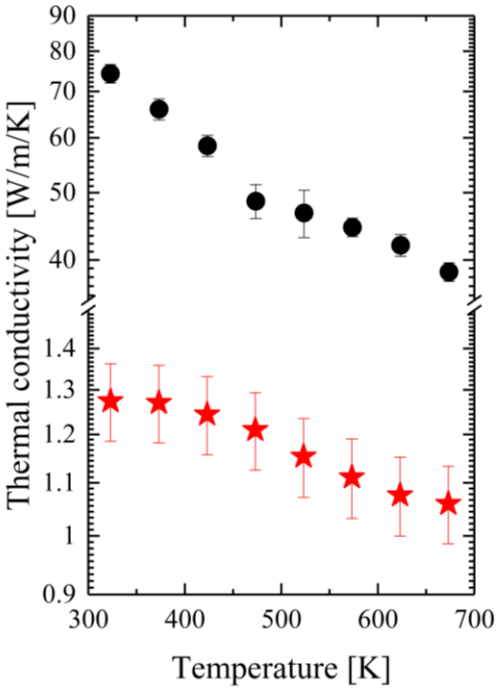

Fig. 3-13 Temperature dependent thermal conductivity of as-etched pSi samples (red stars) and p-doped bulk Silicon (black circles).

4. Results and discussion

4.1. Phonons in porous Silicon

PSi has been proposed as thermoelectric material of interest in various studies [2, 27, 106-108]. Notably, thermal conductivity is envisioned to be manipulated by increasing the diffuse scattering of phonons at artificial interfaces, e.g. pore walls [109, 110] and the phonon dispersion relation is manipulated, for example, via bandgap engineering [24]. While there are various theoretical studies on this topic, experimental investigations beyond macroscopic sample characterization are few [111]. Experimental, microscopic studies are essential for insights into atomistic interactions in nanostructures. Such interactions are encoded in the complex dispersion relation [2, 111]. Concerning thermoelectric research on pSi, it is vital to study the influence of pSi phonon dispersion on macroscopic quantities such as thermal conductivity.

In the current work, inelastic thermal neutron scattering was used to probe microscopic information about phonons across the entire Brillouin zone. It must be considered solely sensitive to the properties of the silicon skeleton when the probed phonon wavelengths become smaller than the length scale of structuring. However, the experimental demand for macroscopic amounts of nanostructured material (≈ 1 cm^3) with well-aligned crystallographic orientation is a formidable obstacle. This section presents the insight into phonon dispersion of pSi with pores roughly $2R \approx 8$nm across at a porosity of $\varphi \approx 50\%$ that is obtained by thermal neutron scattering experiments.

4.1.1. Modelling phonon dispersion

The arguably most intuitive approach to analytically describe the transverse and longitudinal phonon dispersions along the high symmetry directions of silicon are one-dimensional chain-like models. These models readily predict the collective motions of entire planes. Depending on the desired degree of approximation, they account for the interaction between neighboring lattice planes up to an arbitrary order that are for instance nearest neighbor and next nearest neighbor interactions. The entire approach, although simplified, bears a striking resemblance to more fundamental Born-von-Kármán calculations [112] and was used here.

The phonon dispersion for a linear chain of planes is given by

$$\omega^2 = \sum_{i=1}^{\infty} D_i \left(1 - \cos(qia)\right) \tag{4.1}$$

Here, a is the distance between adjacent planes, ω is the frequency of the phonons, and D_i encodes the interaction between planes.

From Eqn. 4.1 the sound velocity is inferred in the low-q limit to be

$$v_s = \sqrt{\sum_{i=1}^{\infty} i^2 D_i \frac{a}{2}} \tag{4.2}$$

There are three independent components c_{ij} of the stiffness tensor in crystals with cubic symmetry. These elastic moduli c_{11}, c_{12} and c_{44} relate to the sound velocities in the crystallographic directions $[hkl]$ via the general expression

$$v_{T/L}^{[hkl]} = \sqrt{\frac{f_{T/L}^{[hkl]}\left(c_{11}, c_{12}, c_{44}\right)}{\rho}} \tag{4.3}$$

where $\rho = 2.33\ gcm^{-3}$ is the silicon mass density and $f_{T/L}^{[hkl]}$ are functions of the three independent elastic constants [2]. It is

$$\begin{aligned} f_L^{[100]} &= c_{11} \\ f_T^{[100]} &= c_{44} \\ f_L^{[110]} &= \frac{c_{11} + c_{12} + 2c_{44}}{2} \\ f_T^{[110]} &= c_{44} \\ f_L^{[111]} &= \frac{c_{11} + 2c_{12} + 4c_{44}}{3} \\ f_T^{[111]} &= \frac{c_{11} + c_{12} + c_{44}}{3} \end{aligned} \tag{4.4}$$

Knowledge of transverse and longitudinal sound velocities in different crystallographic directions allows employing an optimization scheme [2] to determine directly the three elastic constants or related quantities like Young moduli $Y^{[hkl]}$.

For the non-linear least squares approximation of the phonon dispersion (Fig 4-1) the limited number of data points necessitates a conservative approach of minimal number of fitting parameters. Consequently, for transverse phonons, the sum in Eqn. 4.2 is truncated at $i = 2$ and for longitudinal ones already at $i = 1$.

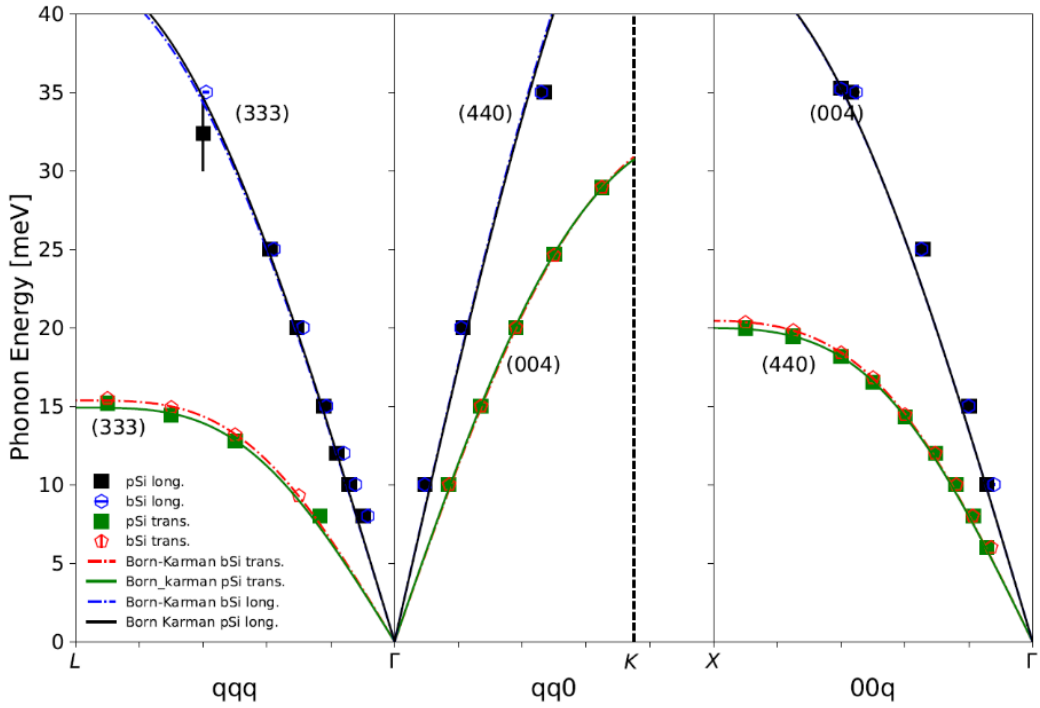

Fig. 4-1 Dispersion of longitudinal and transverse phonons in bSi (open symbols) and in porous silicon (filled symbols) along high symmetry directions [100] ($\overline{\Gamma L}$) [110] ($\overline{\Gamma K}$) and [111] ($\overline{\Gamma X}$): Labels indicate the Bragg reflection at which the phonons were measured. Colored lines (dashed, solid) represent Born-von-Kármán approximations of the different dispersion branches.

It is important for nanostructured materials like pSi to distinguish between micro- and macrostructural properties. Experiments often probe effective quantities averaged and homogenized over length scales l that are significantly larger than the structuring length d. In such a case $l^{-1}d \ll 1$ and experiments do not necessarily provide access to microscopic properties on the nanoscale.

Acoustic transmission spectroscopy [113] was employed to study acoustic sound waves in the limit of long wavelengths $q \to 0$ Å^{-1}, where q refers to the wavevector of the respective

vibrational mode. In the analysis of these experiments, pSi was inherently treated as an effective medium that consists of a single-crystalline silicon skeleton penetrated by nanometer sized pores. The technique provided consequently insights into the porosity-dependent sound velocities and elastic properties of the compound material. Brillouin scattering [114] probes phonons close to the center of the Brillouin zone and data analysis again treats pSi as continuum to obtain averaged material properties.

If at all, macroscopic measurements allow inferring microstructural properties only indirectly from more or less complex data modeling [115-117]. Thermoelectric transport measurements on pSi provide effective thermal conductivities, effective electrical conductivities and effective Seebeck coefficients. Relating these effective quantities to microscopic properties requires at least spatial averaging over interconnected Si-walls and a geometrically complex pore space to properly account for the sample morphology.

However, in general it is not sufficient to treat properties within effective medium theories [118] that relate heterogeneous systems to the properties of a homogenized 'bulk' reference system. On nanometer-sized length scales matter behaves fundamentally different than on macroscopic length scales characteristic for bulk systems. In the case of lattice thermal conductivity for instance novel aspects like phonon confinement and additional phonon boundary scattering at interfaces have to be considered carefully on the nanoscale [117].

The interpretation of macroscopic, mechano-elastic experiments [115, 116, 119] to obtain the elastic moduli of the nanostructured Si-skeleton in pSi is similarly challenging. Macroscopic deformation experiments can be analyzed by means of finite element calculations that include the microscopic properties of the Si-skeleton as adjustable parameters. However, the implementation of the complex sample topology is an obvious obstacle to overcome.

This study does not follow the approach to determine the elastic properties of the pSi-skeleton indirectly from macroscopic measurements.

In contrast, it utilizes inelastic thermal neutron scattering as a microscopic probe to determine the elastic moduli directly. The neutron scattering experiments elucidated the dispersion for phonons with wavelengths smaller than $2nm$ that is well below the structuring length scale of pSi ($\varphi \approx 50\%, R \approx 4nm$). An analysis of this dispersion within the framework of Born-von-Kármán models allowed inferring sound velocities in the Si-skeleton and subsequently the differences between bulk and nanostructure elasticity.

Fig. 4-1 exhibits the *bona-fide* indistinguishable phonon dispersions of pSi and bSi for longitudinal and transverse phonons (symbols) along the high symmetry directions $\overline{\Gamma L}$, $\overline{\Gamma K}$ and $\overline{\Gamma X}$. The dashed lines represent data modeling according to Eqn. 4.1. An excellent agreement between data and the non-linear least squares approximation of Eqn. 4.1 is evident.

Table 4.1 lists sound velocities for pSi and bSi, which are calculated with Eqn. 4.2 using the optimized model parameters D_i. The sound velocities in the pSi-skeleton with $8nm$ wide pores and bSi differ by less than 1% in average. The experimentally estimated sound velocities in bSi however deviate systematically by 5-10% from accepted literature values. This systematic error in the sound velocities forbids the discussion of the elastic moduli in terms of absolute values but does not affect the direct comparison between pSi and bSi.

Table 4-1 Sound velocities for transverse and longitudinal phonons in bSi and pSi in the [100], [110], and [111] directions.

	$v_T^{[100]}$ [m/s]	$v_L^{[100]}$ [m/s]	$v_T^{[110]}$ [m/s]	$v_L^{[110]}$ [m/s]	$v_T^{[111]}$ [m/s]	$v_L^{[111]}$ [m/s]
bSi	5485 ± 29	8992 ± 18	5350 ± 39	8339 ± 48	5124 ± 37	10105 ± 35
pSi	5454 ± 40	8999 ± 16	5425 ± 52	8275 ± 50	4971 ± 79	10197 ± 41
bSi_{lit} [2]	5844	8433	5844	9134	5094	9356
pSi/bSi	0.99	1.00	1.01	0.99	0.97	1.01

Components of the stiffness tensor c_{ij} and uniaxial Young moduli for pSi and bSi in Table 4.2 are derived with Eqn. 4.3. These results refine previous estimates in [2] for the effect of nanostructuring on the microstructural elastic properties of Si. Elastic moduli in pSi are reduced in average by less than 5% compared to bSi. Given the fairly conservative error estimates, one is indeed inclined to dispute any effect of nanostruturing on the elastic properties at all.

Table 4-2 Elastic moduli and uniaxial Young moduli for pSi and bSi as obtained from inelastic thermal neutron scattering experiments.

	c_{11}[GPa]	c_{12}[GPa]	c_{44}[GPa]	$Y^{[100]}$ [GPa]	$Y^{[110]}$ [GPa]	$Y^{[111]}$ [GPa]
bSi	181 ± 1	68 ± 2	69 ± 1	145 ± 2	162 ± 1	169 ± 1
pSi	178 ± 2	73 ± 3	69 ± 1	135 ± 5	160 ± 2	170 ± 1.5

Phonon-softening refers to the reduction of a phonon group velocity, e.g., upon approaching a phase transition, a characteristic temperature or system size. In this sense, Wingert and Yang [120, 121] reported reduced elastic moduli that correspond via Eqn. 4.3 to soft phonon modes for Si nanotubes smaller than $t_{NT} = 25$ nm in diameter [120] or Si nanoribbons with a surface to volume ratio $\frac{S}{V} > 0.11$ nm^{-1} [121]

In analogy with the nanotubes and -ribbons, one can readily characterize pSi by a locally defined, averaged pore-wall thickness t or the well-defined surface-to-volume ratio $\frac{S}{V}$. A simple geometrical model [2] allows estimating t from porosity and average pore radius. Surface-to-volume ratios can be extracted from the BET-analysis and the Si density ρ.

With values of $t \approx 2$ nm $< t_{NT}$ and $\frac{S}{V} = A * \rho \approx 0.366\ \mathrm{nm}^{-1} > 0.11\ \mathrm{nm}^{-1}$ both quantities imply phonon-softening in pSi. However, no indications are found in the thermal neutron scattering experiments that indicate an influence of nanostructuring on the phonon dispersion. Whether this difference between pSi and Si nanotubes and nanoribbons relates to the more complex, not-simply connected topology of pSi or the heavily disordered pore array is a fascinating question that remains unanswered and requires further experimental and theoretical studies beyond the scope of this work.

However, this result puts a practical limit on the minimum thermal conductivity for anodized pSi membranes. Excluding unrealistic approaches for pSi like phonon dispersion engineering, nanostructuring induced phonon-softening appears as prerequisite to beat the so-called amorphous limit [122] of $\kappa_{ph} = 0.1\ Wm^{-1}K^{-1}$ in pSi. In retrospective of the presented results, this necessitates samples with even higher porosity and smaller structural feature sizes, samples whose mechanical stability cannot be guaranteed.

It appears in order, to conclude this section with a brief review of results on phonon-softening in pSi as presented in [2]**.** There, Hofmann et.al study phonons with wavelengths between 2 nm and 10 nm to determine the elastic properties of pSi. Assuming to probe dominantly the properties of the pSi-skeleton a sizable phonon-softening in the range $c_{ij}^{bSi} > c_{ij}^{pSi} > 0.75 c_{ij}^{bSi}$ is inferred from scattering experiments. These results are clearly refined within the present work.

The cold neutron scattering experiments presented in [2] start the transition from microscopic probes like thermal neutron scattering to macroscopic probes like acoustic transmission spectroscopy. This troubling and admonishing tale of length scale dependent experimental

results is unfortunately not new and known from diffusion experiments in confinement [123, 124] where different probes seemingly give different answers to the same question.

The inelastic neutron scattering studies presented are first steps towards a thorough understanding of the influence of nanostructuring on the phonon dynamics in phonon-softening silicon. Nanostructuring on sub-10 nanometer length scales does not have an effect on the phonon dispersion. In contrast to Si nanoribbons and nanotubes, no sizable phonon-softening in pSi is observed in the inelastic neutron scattering experiments.

4.2. Specific heat capacity

For understanding the behaviour of the heat capacity of a solid, it is important to first obtain an expression for its total energy. The total vibrational energy is denoted as the sum of the energy of all the phonons in the solid, $E = \sum_{ph} \hbar\omega$ where $\hbar = h/2\pi$ with Plank constant h and phonon frequency ω. Since many phonons can have the same energy, the total energy can be expressed as $E = \sum_{\omega} n(\omega)\hbar\omega$, where $n(\omega)$ is the number of phonons of frequency ω. For a specific phonon mode characterized by its energy, $\hbar\omega$, the average occupation of that phonon mode at a given temperature is expressed by Bose-Einstein statistics $f(\omega) = 1/\left(e^{\beta\hbar\omega} - 1\right)$, where $\beta = 1/k_B T$ and k_B is Boltzmann's constant.

The number of available phonon modes can be expressed by the density of states $g(\omega)$, where $n(\omega) = f(\omega)g(\omega)$. From classical mechanics, it is known that a point mass has three degrees of freedom and, hence, a solid containing N atoms, comprises 3 N vibrational modes. Since N is large, the subtraction of the three rotational and three translational degrees of freedom of the solid can be neglected. The sum over the vibrational modes can be represented as an integral $\int g(\omega)d\omega = 3N$.

Subsequently, the total vibrational energy of a crystalline material can be expressed as

$$E = \int_0^{\infty} g(\omega) \frac{\hbar\omega}{e^{\beta\hbar\omega} - 1} d\omega \tag{4.5}$$

Now taking the derivative with respect to temperature, heat capacity at constant volume V can be expressed as

$$C_v = \left(\frac{\partial E}{\partial T}\right)_v = k_B \int_0^\infty g(\omega) \frac{(\beta\hbar\omega)^2 e^{\beta\hbar\omega}}{(e^{\beta\hbar\omega} - 1)^2} d\omega \tag{4.6}$$

In the experiments, the heat capacity was measured at constant pressure expressed as $C_p = \left(\frac{\partial H}{\partial T}\right)_p$, where H denotes enthalpy. However, since solids are almost incompressible in the used temperature range, $C_p = \left(\frac{\partial H}{\partial T}\right)_p$ is very close to heat capacity at constant volume, $C_v = \left(\frac{\partial E}{\partial T}\right)_v$. For bulk Si and pSi, the thermal expansion is negligible in the probed temperature range of $4K$-$300K$ and therefore $C_p \approx C_v$

4.2.1. Dulong-Petit Law

In the 19th century Dulong and Petit discovered that in the high-temperature limit of Eqn. 4.6 where $k_B T \gg \hbar\omega$, heat capacity becomes constant and takes the form $C = 3Nk_B$. It is known as the Dulong-Petit law from classical statistical mechanics. Constant heat capacity in this limit is simply a consequence of the fact that the quantized nature of the vibrations does not show up anymore at such high temperatures. Energy can be taken up in a quasi-continuous manner, and one arrives at the classical result that each degree of freedom yields $k_B T$ to the energy of the solid.

4.2.2. Einstein approximation

With the introduction of quantum mechanics, Einstein attempted to describe the temperature dependence of heat capacity. According to the Einstein approximation [125, 126], crystalline material comprising N atoms can be treated as an assembly of independent $3N$ oscillators, all vibrating with one single frequency ω_E for which the density of states $g(\omega)$ can be expressed as

$$g(\omega) = 3N\delta(\omega - \omega_E). \tag{4.7}$$

The Einstein temperature Θ_E is defined as

$$\Theta_E = \frac{\hbar\omega_E}{k_B}. \tag{4.8}$$

The resulting heat capacity can be expressed as

$$C_E = 3Nk_B \left[\frac{e^{\Theta_E/T} \left(\Theta_E/T\right)^2}{\left(e^{\Theta_E/T} - 1\right)^2} \right]. \tag{4.9}$$

In the high-temperature limit $\left(\Theta_E/T \ll 1\right)$, the term in square brackets approaches unity, and the Dulong-Petit law is recovered. This term decreases for intermediate temperatures and drops exponentially to zero for $\Theta_E/T \gg 1$ (i.e. $T \rightarrow 0$).

More specifically, the C_E starts to deviate significantly from the Dulong-Petit value for $\Theta_E/T \sim 1$, i.e. for temperatures $\Theta_E \sim \frac{\hbar\omega_E}{k_B}$. For temperatures of the order of Θ_E or below Θ_E, the thermal energy is no longer enough to excite the corresponding phonon mode quasi-continuously, the discrete nature of the vibrational levels starts appearing, and one says that this mode starts to "freeze out". From Eqn. 4.9, it can be seen that the specific heat approaches zero exponentially with temperature as $\frac{e^{-1/T}}{T^2}$, not as T^3 .While the optical branches are unimportant at low temperatures, the low-energy acoustic branches may still contribute. It is the contribution from the latter that gives rise to the T^3scaling for $T \rightarrow 0$.

4.2.3. Debye model

Debye treated the lattice as an elastic continuum. This assumption led to a distribution of allowed frequencies rather than a single allowed frequency.

To adequately address the low-temperature limit, the Debye model takes into account the acoustic branches. For $T > 0K$, primarily the lowest energy modes can still be excited thermally, i.e. specifically, the part of the single acoustic branch close to the Brillouin zone centre. In this region, the dispersion is linear in $\vec{q}$, and for the corresponding very long wavelength modes, the solid behaves like a continuous elastic medium. It is the conceptual idea behind the Debye model, which approximates $\omega(\vec{q}) = v_s\vec{q}$ for all modes, with v_s the speed of sound. Here, only a minimalistic Debye model is discussed because even in a perfectly isotropic medium, there would be at least different sound speeds for longitudinal and transverse phonons.

This linear scaling yields Debye density of states in a quadratic form as following

$$g(\omega) = \frac{9N\omega^2}{{\omega_D}^3} \tag{4.10}$$

$\omega_D = v_s(6\pi^2 n)^{1/3}$ is the Debye frequency where n refers to the number density of atoms in Silicon and v_s is the average sound velocity.

Since this quadratic form would be unbound for $\omega \to \infty$, a cutoff Debye frequency ω_D is introduced necessary to obtain a total of only 3N degrees of freedom by taking the integral over $g(\omega)$ over all frequencies.

The Debye temperature for three dimensional (3D) system can be expressed as

$$\Theta_D^{3D} = \frac{\hbar\omega_D}{k_B}. \tag{4.11}$$

Debye heat capacity for 3D system [127, 128] can then be expressed as

$$C_D^{3D} = 9Nk_B\left(\frac{T}{\Theta_D^{3D}}\right)^3 \int_0^{\Theta_D^{3D}/T} \frac{e^x x^4}{(e^x-1)^2}dx \tag{4.12}$$

Considering the temperature dependence of specific heat capacity, it should be noted that for $T \ll \Theta_D^{3D}$, C_D is directly proportional to T^3 and for $T \ll \Theta_E$, Einstein heat capacity varies with temperature as $\frac{e^{\frac{\Theta_D^{3D}}{T}}}{T^2}$. The experimental specific heat capacity for most materials in the lower temperature regime usually exhibits T^3 behavior following the Debye model.

Therefore, the specific heat data from a real solid can be well understood from the discussion of the three temperature ranges. Only the acoustic modes contribute noticeably to C_V at low temperatures, for which the Debye model provides a good description. Optical modes are excited with increasing temperatures, too, and the C_V curve changes gradually to the form predicted by the Einstein model. Finally, all modes contribute quasi-continuously at sufficiently high temperatures, and the classical Dulong-Petit value is approached. Similar to the role of Θ_E in the Einstein model, the Debye temperature Θ_D indicates the temperature range above which classical behaviour sets in and below which modes begin to freeze out due to the quantized nature of the lattice vibrations. Debye temperatures are usually obtained by fitting the predicted T^3 form of the specific heat to low-temperature experimental data.

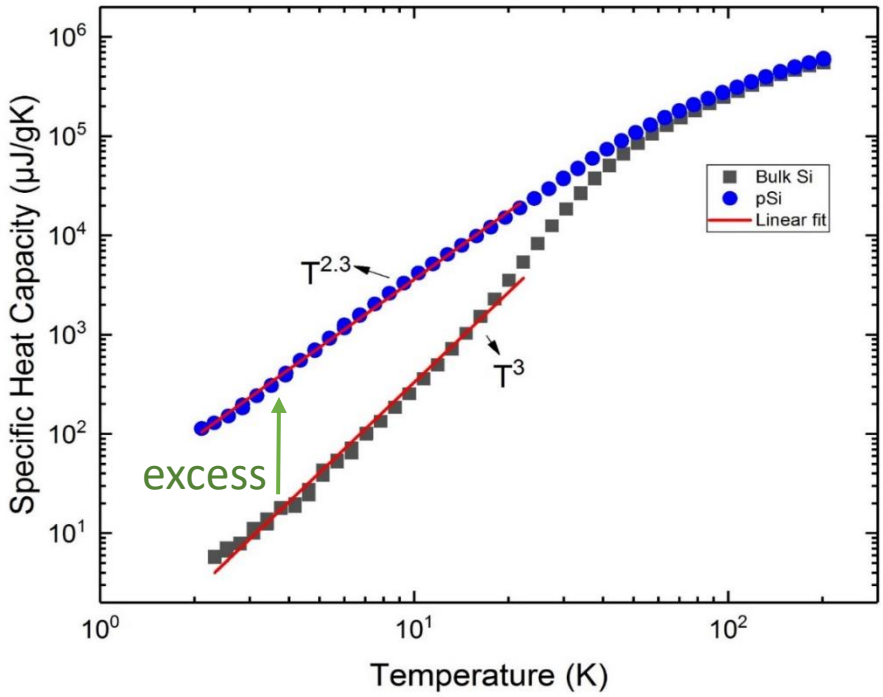

Fig. 4-2 Specific heat capacity of bulk Silicon (black squares) and pSi (blue circles) measured by PPMS. Red lines are fits to the data representing temperature dependence. Excess specific heat capacity identified for pSi as compared to bulk Silicon at lower temperature is labelled by green arrow.

4.2.4. Modelling specific heat

Fig. 4-2 presents the temperature-dependent specific heat capacity (C_P) of pSi and bulk Si measured in the temperature range of $2K - 300K$ with the PPMS. A 'traditional' specific heat capacity with T^3 dependence at low temperatures is seen for the bulk Si reference sample. However, a deviation from the T^3 dependence of the specific heat capacity is observed for pSi at lower temperatures. At high temperatures, the Dulong-Petit law in pSi and bulk Si is

retrieved. The deviation is analyzed considering both Einstein and Debye contribution of specific heat in bulk Si and pSi.

For analysis, first bulk Silicon's specific heat capacity is analyzed with a standard model approach governed by Eqn. 4.13. For a good fit, one needs to incorporate both, the Debye specific heat C_D^{3D} and the Einstein specific heat C_E^{3D} in the model. Both functions are combined with different weights f_D^{3D} and f_E^{3D}, in order to describe the data. For that, a plot of C_p / T^3 against temperature is presented in Fig. 4.3 to model this C_v. Debye contribution is taken into account, that is suited for acoustic branches at low temperatures and which show typical temperature T^3 behavior at low temperatures. Subsequently, flat part of <110> dispersion branch is treated by including Einstein modes (C_E^{3D}) in the current model.

$$C_v^{Bulk\ Si} = f_D^{3D} C_D^{3D} + (1 - f_D^{3D}) C_E^{3D} \tag{4.13}$$

Fig. 4-3 shows a very good agreement between the model and the experimental result. Model fits of bulk Silicon indicated about 90% contribution of Debye specific heat capacity $f_D^{3D} C_D^{3D}$ while 10% contribution of Einstein specific heat capacity $(1 - f_D^{3D}) C_E^{3D}$. Out of the model fits, Einstein temperature $\Theta_E = 177K$ $(\sim 15meV)$ and Debye temperature $\Theta_D = 602K$ $(\sim 52meV)$ are extracted as fitting parameters. $\Theta_D = 602K$ is found to be in close agreement to that reported for bulk Silicon [2] and origin of Einstein contribution is attributed to flat part of <110> dispersion [129]**.** Combined contribution of Debye and Einstein contribution guarantees Dulong Petit law at high temperatures.

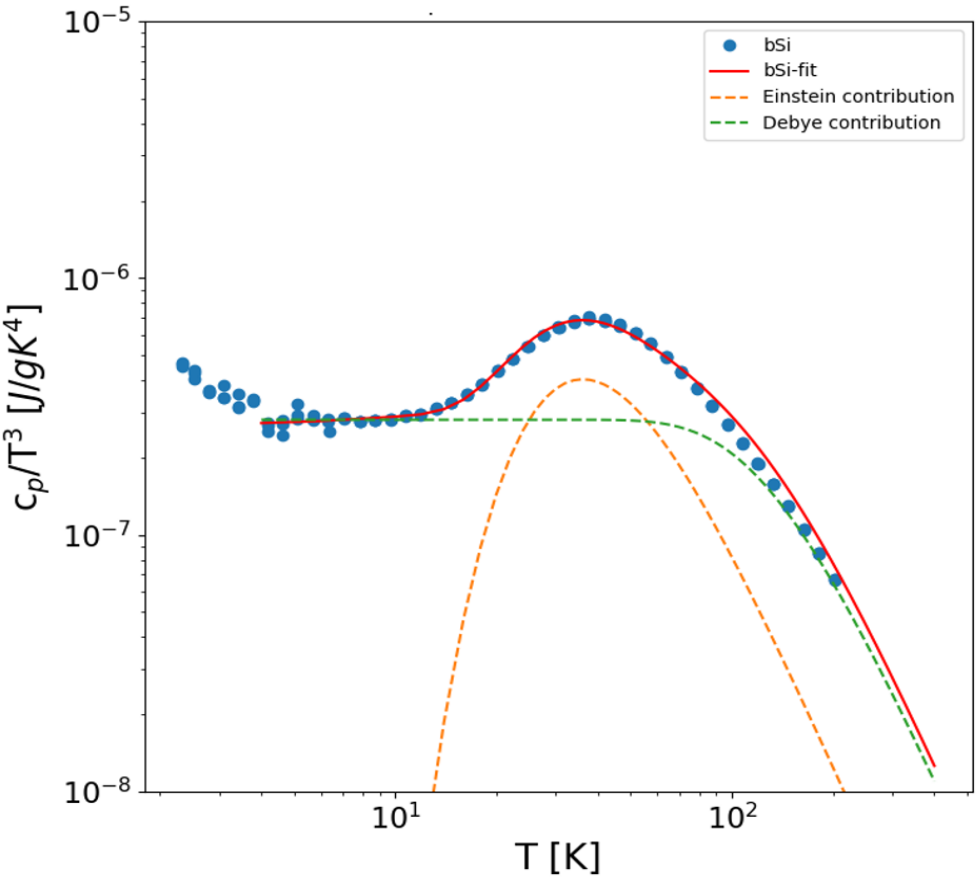

Fig. 4-3 Experimental data of bulk Silicon's specific heat (blue circles) represented as C_p/T^3 against temperature. Experimental data agrees well with a model fit (red line) governed by Eqn. 4.13 taking into account Einstein and Debye contribution (dashed lines) to specific heat capacity of bulk Silicon. One should note that data at very low temperatures ($T < 4K$) are an artefact from the PPMS instrument and is not attributed to the bulk Silicon sample but to the copper sample holder.

The modelling approach used for porous Silicon's specific heat capacity was to fix the fitting parameters from bulk Silicon and employ additional 2D surface contribution of Debye and Einstein specific heat capacity as expressed in the Eqn. 4.14.

$$C_{pSi} = f_{bulk}C_{bulk} + (1-f_{\text{bulk}})[f_D^{2D}C_D^{2D} + (1 - f_D^{2D})C_E^{2D}]. \tag{4.14}$$

2D surface contribution of Debye specific heat capacity C_D^{2D} [127] is

$$C_D^{2D} = 6Nk_B\left(\frac{T}{\Theta_D^{2D}}\right)^2 \int_0^{\Theta_D^{2D}/T} x^3 \frac{e^x}{(e^x-1)^2}dx \tag{4.15}$$

and 2D surface contribution of Einstein specific heat capacity C_E^{2D} can be expressed as

$$C_E^{2D} = 3Nk_B \frac{e^{\Theta_E^{2D}/T}\left(\Theta_E^{2D}/T\right)^2}{\left(e^{\Theta_E^{2D}/T}-1\right)^2}. \tag{4.16}$$

The surface contribution of each plays a role in excess specific heat capacity observed in pSi at lower temperatures. Both are combined with different weights, f_D^{2D} and f_E^{2D}, in order to describe the data.

Table 4-3 Fitting parameters for pSi specific heat model-fit presented in Fig. 4-4. governed by Eqn. 4.14.

Fixed parameters	$\Theta_D^{3D}\ [K]$	$\Theta_E^{3D}\ [K]$		
	602	178		
Free parameters	$\Theta_D^{2D}\ [K]$	$\Theta_E^{2D}\ [K]$	f_D^{2D} [%]	f_{bulk} [%]
	149 ± 0.02	40 ± 0.01	10 ± 0.05	90 ± 0.02

Fig. 4-4 shows an excellent agreement between the model and experimental data. Out of the model fit, Einstein temperature $\Theta_E^{2D} = 40K$ (~3meV) and Debye temperature $\Theta_D^{2D} = 149\ K$ ($\sim 12meV$) are extracted for pSi. The Debye contribution of C_D^{2D} explains the characteristic $T^{2.3}$ behaviour at low temperature with an assumption of presence of acoustic phonon modes on the surface of pSi. The origin of Einstein contribution of C_E^{2D} can be attributed to a boson peak of amorphous SiO_2 in pSi. In amorphous materials, the Boson peak is considered a signature of the existence of localized vibrational modes [130]. It was observed in other materials as well such as the polymer poly(methylmethacrylate) (PMMA) [131], the semiconductors α-Se, B_2O_3, As_2S_3 [132], and the metallic glass PdZr [133].

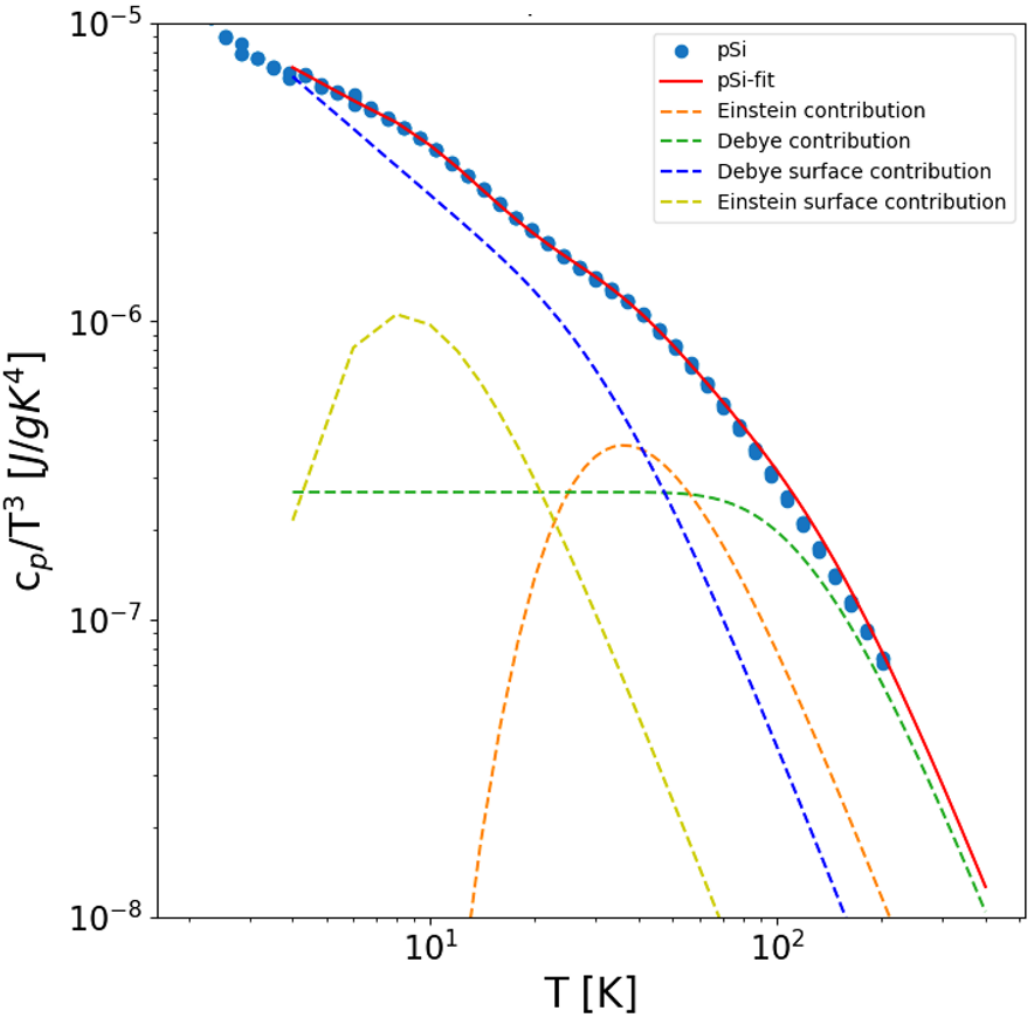

Fig. 4-4 Experimental specific heat capacity of pSi (blue circles) represented as C_p/T^3 against temperature. Experimental data agrees excellently with a model fit (red line) taking into account Debye and Einstein contribution of C_p in bulk Silicon together with surface contributions.

4.3. Thermal conductivity

In bulk Si, the dominant scattering mechanisms are the phonon – phonon and phonon– carrier scattering and the scattering by lattice defects [31]. However, additional scattering events occur and dominate in pSi, such as phonon scattering with interfaces [32]. These scattering effects reduce the phonon mean free path and significantly increase diffuse scattering, reducing thermal conductivity.

The cross-plane thermal conductivity of pSi was probed by LFA in the temperature range of $300K - 640K$. The in-plane thermal conductivity of pSi was probed by PPMS in the temperature range of $3K - 300K$. Due to experimental constraints, no common temperature range was investigated for the in-plane and cross-plane thermal conductivity of pSi samples.

As presented in Appendix C, in-plane and cross-plane thermal conductivities of pSi at $T = 300K$ show anisotropy in thermal conductivity. In the following sections, a robust model for the data analysis of the cross-plane thermal conductivity will be developed, followed by a discussion of the first ideas to describe the in-plane thermal conductivity of pSi.

4.3.1. From specific heat to thermal conductivity

It was found that at higher temperature the specific heat capacity of pSi approaches that of bulk Si (Fig. 4-2), dominated by 3D Debye contribution for $T > 50K$. Therefore, 3D Debye Callaway model was utilized for the thermal conductivity's data analysis probed by LFA in the temperature range of $T = 300 - 640K$. Specific heat capacity of pSi probed by PPMS for $T < 50K$ was found to deviate from classical 3D Debye model (i.e. classical T^3 dependence for $T \to 0K$). This deviation was accounted for 2D Debye DOS contribution to pSi specific heat at low temperatures as discussed in the last section. Thermal conductivity probed by PPMS showed neither $\kappa \sim T^3$ nor $\kappa \sim T^2$ temperature dependence mirroring $C_{pSi} \sim T^{2.3}$. Rather, thermal conductivity measured by PPMS showed $\kappa \sim T^1$ temperature dependence for $T \to 0K$ as evident in Fig. 4-5. This deviation will be discussed in Section 4.3.6.

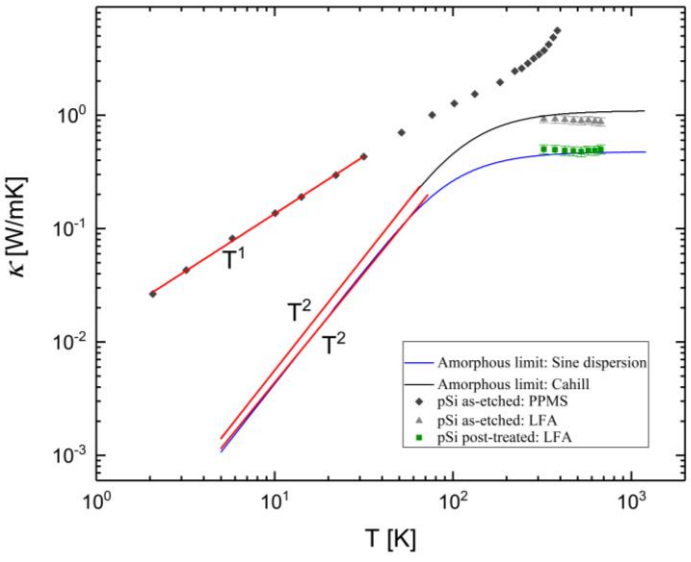

Fig. 4-5 Thermal conductivity of pSi probed by PPMS and LFA. Red lines are linear fits to the temperature dependence of thermal conductivity. Green squares represent cross-plane thermal conductivity of chemically post-treated pSi samples probed by LFA. Black and blue solid lines represent amorphous limits calculated from sine dispersion and Cahill's model detailed in Section 4.3.6

4.3.2. Callaway model for cross-plane thermal conductivity ($T = 300K - 640K$)

The temperature dependent lattice thermal conductivity κ of a crystalline material [134, 135] can be expressed as

$$\kappa = \frac{\pi^2 k_B 2T}{9\hbar} \int \tau_{ph}(\omega) {v_g}^2(\omega) g(\omega) \mathrm{W}(\omega) \mathrm{d}\omega \tag{4.17}$$

where $v_g(\omega)$ is the frequency-dependent phonon group velocity and $g(\omega)$ represents the phonon density of states. $\mathrm{W}(\omega) = \left(\frac{\hbar\omega}{k_B T}\right)^2 \frac{e^{\frac{\hbar\omega}{k_B T}}}{\left(e^{\frac{\hbar\omega}{k_B T}} - 1\right)^2}$ is the so-called window function [136, 137]. $\tau_{ph}(\omega)$ is the frequency-dependent phonon relaxation time that takes into account various phonon scattering processes.

For bulk Si, $\tau_{ph}(\omega)$ is dominated by point defects, Umklapp and boundary scattering as listed in Table 4-4. Total $\tau_{ph}(\omega)$ is calculated using the Matthiessen's rule

$$\frac{1}{\tau_{ph}(\omega)} = \frac{1}{\tau_D(\omega)} + \frac{1}{\tau_B(\omega)} + \frac{1}{\tau_U(\omega)} + \frac{1}{\tau_{\boldsymbol{\eta}}(\omega)}. \tag{4.18}$$

Table 4-4 Frequency-dependent phonon relaxation times. In these expressions, the prefactors M_P and M_U were used as fitting parameters. F is specularity parameter and L denotes characteristic length of sample's cross section. T_U is Umklapp temperature, η is nanostructure length and $v_g(\omega)$ is phonon group velocity.

Scattering process	Inverse relaxation time	Fitting parameters
Point defects	$\frac{1}{\tau_D(\hbar\omega)} = M_P\ \omega^4$	$M_P = 3.6419 \times 10^{-44} \pm 1.09 \times 10^{-42}\ [s^3]$
Crystal boundaries	$\frac{1}{\tau_B(\hbar\omega)} = \frac{v g(\omega)}{FL}$	$FL = 1.5 \times 10^{-5}$ (fixed) $[m]$
Umklapp scattering	$\frac{1}{\tau_U(\hbar\omega)} = M_U\ \omega^2\ T \exp\left(-\frac{T_U}{T}\right)$	$M_U = 3.5 \times 10^{-19} \pm 1.05 \times 10^{-19}\ [s/K]$
Nanostructures	$\frac{1}{\tau_{\boldsymbol{\eta}}(\hbar\omega)} = \frac{v_g(\omega)}{\eta}$	Not applicable for bulk Si

Further, the total mean free path $\lambda(\omega)$ can then be expressed as

$$\lambda(\omega) = v_g(\omega)\tau_{ph}(\omega) \tag{4.19}$$

Experimental data for bulk Silicon obtained from PPMS up to $300K$ is modelled using the Callaway approach (Fig. 4-6) utilizing phonon sine dispersion relation $\omega(q)$. Phonon density of states $g(\omega) = \frac{3}{2\pi^2} \times \frac{q(\omega)^2}{v_g}$ and phonon group velocity $v_g(\omega) = {}^{\partial\omega}/_{\partial q}$ were extracted from phonon sine dispersion relation (Eqn. 4.20).

$$\omega(q) = \omega_0 \sin(\pi k/2k_D) \tag{4.20}$$

$$v_g(\omega) = {}^{\partial\omega}/_{\partial q} = \frac{\omega_0 \pi}{2k_D} \cos(\pi k/2k_D) \tag{4.21}$$

ω_0 is the frequency at zone boundary (Eqn. 4.22) and k_D is the Debye wavevector (Eqn. 4.23).

$$\omega_0 = \frac{2\,\omega_D}{\pi} \tag{4.22}$$

$$k_D = {}^{\omega_D}/_{v_s} \tag{4.23}$$

ω_D in Eqn. 4.22 and Eqn 4.23 denotes Debye cutoff frequency expressed as

$$\omega_D = v_s(6\pi^2 n)^{1/3} \tag{4.24}$$

where n represents the number density of atoms in Silicon and v_s is the averaged sound velocity used in the model fits considering three acoustic branches (two transverse and one longitudinal)

$$v_s = \left[\frac{1}{3}\left(\frac{1}{{v_l}^3} + \frac{2}{{v_t}^3}\right)\right]^{-\frac{1}{3}} \tag{4.25}$$

Silicon's longitudinal sound velocity, $v_l = 8433\ m/s$ and transverse sound velocity, $v_t = 5844\ m/s$ along [001] as reported in [2] were used for the current model fits. ω_0 and ω_D were used as fixed parameters calculated from Eqn. 4.22 and Eqn. 4.24 respectively. Table 4-4 lists fitting parameters utilized for least square model fitting of thermal conductivity of p-doped bulk Silicon. Parameter F in the boundary scattering expression denotes phonon specularity [138]. F is zero for completely specular phonon reflection, and F is one for completely diffusive boundary scattering. Whenever partial specular reflection occurs, F is between zero and one. L represents characteristic length related to the sample's cross section [134]. Considering impurity scattering solely due to the boron doping in Silicon samples, M_P was extracted as a fitting parameter. Umklapp scattering expression of $\frac{1}{\tau_U(\hbar\omega)} = M_U\ \omega^2\ T\exp\left(-\frac{T_U}{T}\right)$ used for the model-fits in the current work was initially obtained by Slack et al. [139]. The value of M_U was determined from the model fit as a fitting parameter.

Table 4-5 Best-fit parameters extracted from Callaway model fitting of thermal conductivity of p-doped bulk Silicon probed by PPMS.

Fitting parameters	$\boldsymbol{M_P}$ $\boldsymbol{s^3}$	$\boldsymbol{M_U}$ $\boldsymbol{s/K}$	$\boldsymbol{T_U}$ $\boldsymbol{K}$
Bulk Silicon (Boron doped)	1.42×10^{-45}	2.12×10^{-19}	152
Literature	1.32×10^{-45} [140]	2.8×10^{-19} [140] 1.73×10^{-19} [44]	137 [44]

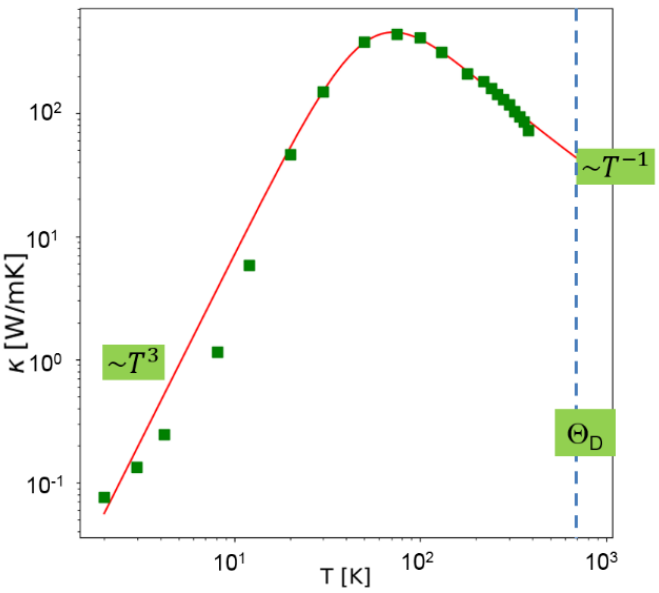

Fig. 4-6 Thermal conductivity of bulk Si probed by PPMS (green squares). Red line represents Debye Callaway model-fit governed by Eqn. 4.19 with the best-fit parameters enlisted in Table 4-5. Debye temperature of bulk Silicon is marked with dashed line.

At low temperatures, the phonon density is too low for significant phonon–phonon collisions. Further, point defect scattering becomes negligible. Rather, λ is determined by ω-independent phonon collisions with crystal surfaces and grain boundaries. As expected from the Debye model, C_v depends on T^3, so that κ_{ph} has the same temperature dependence as C_v, that is $\kappa_{ph} \propto T^3$. With further increase in temperature, the temperature dependence of κ_{ph} is controlled by $\lambda(\omega)$ rather than C_v, which changes only slowly with temperature. $\lambda(\omega)$ becomes limited by phonon–phonon collisions that obey the Umklapp process. Since $\lambda(\omega)$ is inversely proportional to the phonon density, $\tau_U(\hbar\omega)$ decreases with increasing temperature. Thermal conductivity is controlled by $\lambda(\omega)$ and C_v that changes only slowly with temperature. Since $\lambda(\omega)$ is inversely proportional to phonon density, κ_{ph} decreases with temperature. At temperatures above the Debye temperature, C_v is constant, and the phonon density increases with temperature. Thus, the $\lambda(\omega)$ decreases as $\lambda(\omega) \propto 1/T$, which means that $\kappa_{ph} \propto T^{-1}$ at sufficiently high temperatures [141].

For pSi, the Callaway model is not expected to work right away, as it does not take into account compound average of pSi pores upon porosification. Therefore, the applicability of effective medium models (EMMs) is reviewed in the next section that considers the compound average within pSi. PSi phonon dispersion obtained from neutron scattering experiments is followed by in-depth analysis of phonon dynamics. No change in pSi phonon dispersion is observed upon

nanostructuring. Bulk Si sound velocities from [2] is used to calculate the phonon density of states allowing the implementation of the Callaway model on temperature-dependent thermal conductivity data. The data analysis considers the compound average of pSi pores taken into account by EMMs and a new scattering length introduced in the system upon nanostructuring by the Callaway model.

4.3.3. Effective medium models

Developing more precise and unified methods to describe microstructure-property relationships (MPR) is essential in most heterogenic materials. In the literature, various equations are utilized for predicting the MPR [117, 142-144]. Many of these equations are derivable from theoretical approaches, such as effective medium (EM) theories [117, 145, 146]. Numerous models are proposed in literature to predict the heterogenic medium's macroscopic properties, knowing the constituents' properties and volume fractions [117, 143, 146]. They are known as effective medium theories (EMTs) or effective medium approximations (EMAs) [144]. In these models, heterogenic materials are considered as being macroscopically homogenous [118].

For example, heat current density $\mathrm{j}(\vec{r})$ at a particular point r in the material can be correlated to thermal conductivity with a temperature gradient at that point as governed by Eqn. 4.26.

$$\mathrm{j}(\vec{r}) = \kappa(\vec{r})\nabla T(\vec{r}) \tag{4.26}$$

$$< \mathrm{j}(\vec{r}) > \; = \; < \kappa(\vec{r})\nabla T(\vec{r}) > \; = \kappa_{eff} < \nabla T(\vec{r}) > \tag{4.27}$$

where < > refers to ensemble average.

Heterogeneous materials, such as polycrystalline ceramics, nanophase composites, and multi-phase composites, constitute two or more phases [117, 147]. The various properties of the materials are the macroscopic averages of statistical combinations of different properties of the many constituent phases. If the details of the inhomogeneities, i.e. material microstructure, change, the results of the statistical combination will change, and the macroscopic properties of the materials will also change, assuming that the component phases are isotropic. It is convenient to make the "ergodic" hypothesis [118] that the heterogeneous materials are statistically homogeneous, which means that if we randomly select some differential volumes or elementary structural units from the materials, the physical properties of these differential

volumes are the same as the properties of the macroscopic sample. This assumption also means that the property parameters' spatial (volume) average can substitute for the ensemble average (Eqn. 4.27).

Various effective medium models are reviewed in literature [117, 143]. Maxwell gave an analytical expression for the effective conductivity of a heterogenic medium. His model considered spherical particles embedded in a matrix with no thermal interaction existing between them [35].

Maxwell's model can be expressed as following

$$s(\varphi) = \frac{\kappa_{eff}}{\kappa_{bulk}} = \frac{1-\varphi}{1+\frac{\varphi}{2}} \tag{4.28}$$

where $s(\varphi)$ denotes the ratio of effective thermal conductivity κ_{eff} and bulk thermal conductivity κ_{bulk}, and φ is the porosity.

Many researchers modified Maxwell's model. Rayleigh described EMM in terms of regular array of spheres in a matrix [148]. Bruggemann proposed a differential transition model for low to high concentrations of dispersed particles in a matrix [37]. His theory assumes that a composite can be constructed incrementally by introducing infinitesimal changes to an existing material [34]. This scheme's advantage is that it covers a broad spectrum of materials, e.g. composites and porous materials. Another empirical model known as Lewis-Nielsen model [38] takes into account a wide range of filler shapes embedded in the matrix.

With an increased amount of filler particles per unit volume, one eventually reaches a point at which they begin to contact. Heat transfer is easier between two contacting particles than between the particle and the matrix, assuming highly conductive particles. With increasing filler fraction, chains of connected conductive particles begin to appear as channels. The filler volume fraction at which this transition occurs is known as the percolation threshold. [145, 147]. In this context, porous materials can be considered a hybrid system containing a solid matrix and gaseous inclusions (i.e. pores). Long, complex heat transport paths via small solid fractions in such materials do not ensure good thermal conduction. The limitation of classical EMMs is that they break down for materials with high porosities closer to the percolation threshold. However,

the Kirkpatrick model includes a self-consistent effective medium (SCEM) approach and considers the percolation threshold in disordered systems [38] as expressed in Eqn. 4.29.

$$s(\varphi) = 1 - \frac{\varphi}{\varphi_c} \tag{4.29}$$

where φ_c is the percolation threshold.

4.3.4. Combination of Callaway and Effective Medium Models

The limitation of the Callaway model is that it does not account for compound averages as in the case of effective medium models. However, in the Callaway model, an additional scattering length η for pSi is taken into account. An additional scaling parameter s_ϕ plugged in our model considers the porosity of pSi samples. The thermal conductivity of pSi can then be expressed as $\kappa_{pSi} = s_\phi * \kappa$.

The idea implemented in the current work is to combine the Callaway model and effective medium models to have insights into both macroscopic and microscopic properties of pSi. For pSi analysis, it was assumed that porosification will not change the boundary, point defect and Umklapp scattering parameters obtained from Callaway model fitting of bulk Si. Therefore, the Callaway model (with these fixed parameters) was then implemented on thermal conductivity data of pSi obtained from LFA diffusivity in the temperature range of $300K - 640K$. Reducing the number of free parameters allows the extraction of two free parameters: the scaling parameter s_Φ and the nanostructure length η encoded in inverse scattering rate expression $\frac{1}{\tau_\eta(\hbar\omega)} = \frac{v_g(\omega)}{\eta}$, for each pSi sample. Fig. 4-7 shows an example model-fit of one of the pSi samples. Table 4-6 enlists fixed and free parameters for the best model fit.

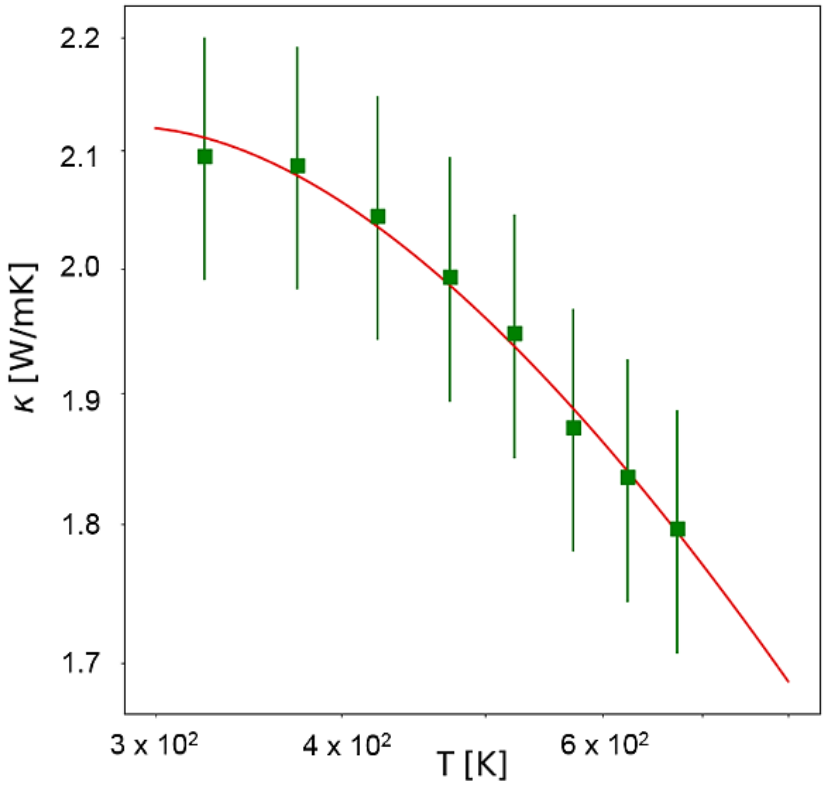

Fig. 4-7 Temperature dependent thermal conductivity of pSi (green squares). Red line represents Callaway model-fit with fitting parameters enlisted in Table 4-6.

Table 4-6. Best-fit parameters extracted from bulk Si model-fit utilized as fixed parameters in thermal conductivity modelling of pSi. s_ϕ and η denotes scaling parameter and nanostructure lengths respectively extracted from Callaway model fit of pSi (Fig. 4-7).

Fixed parameters	M_P $[s^3]$	$M_U[s/K]$	T_U $[K]$	$F \times L$ $[m]$
	1.42×10^{-45}	2.12×10^{-19}	152	$0.4 \times (17.4 \times 10^{-6})$
Free parameters	s_ϕ	$\eta\ [nm]$		
	12.1% ± 0.7%	10.2 ± 0.9 nm		

Scaling parameters s_ϕ (extracted from the Callaway model for thermal conductivity) are plotted against porosity of each sample as presented in Fig. 4-8 and analysed utilizing various EMMs.

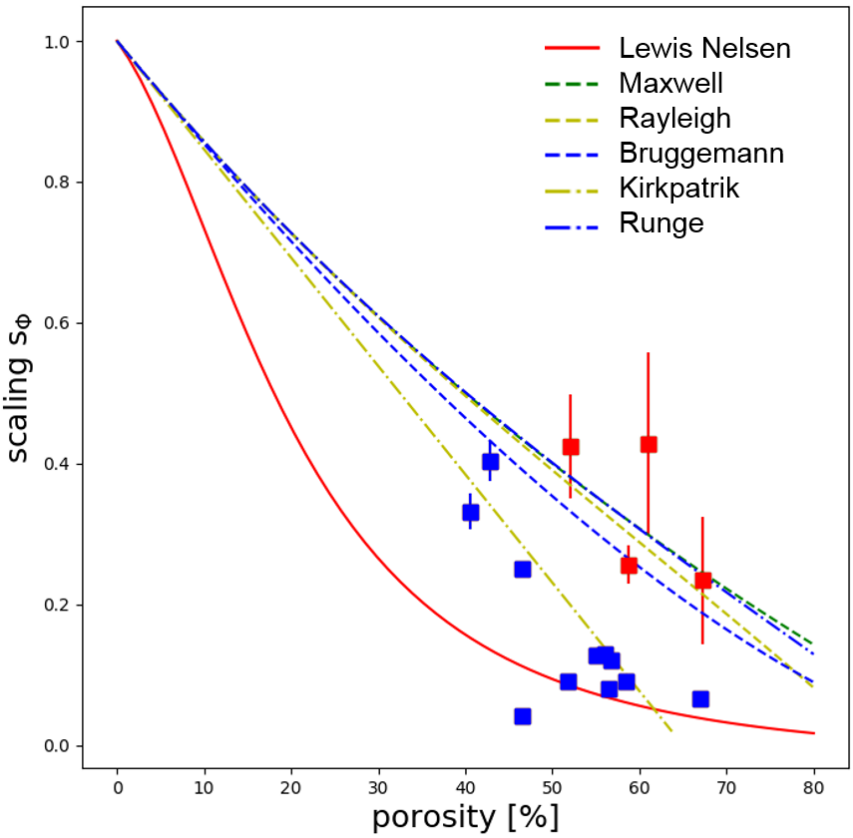

Fig. 4-8 EMA model fits presenting correlation of scaling parameters (extracted for each pSi sample from Callaway model-fit) with porosity. Blue squares show experimental data in line with Kirkpatrick model fit. Red squares indicate experimental data points showing prominent deviation from EMA models.

Blue and red squares present experimental data. As presented in the plot, it clearly shows that among all model fits, Kirkpatrick's model fits the best with experimental data while Lewis-Nielsen model shows deviation. Red squares in the plot refers to minority of pSi samples that show deviation from all EMMs.

It is essential to analyze thermal conductivity of pSi by taking into account both nanostructuring and porosity. Nanostructuring cause the reduction of thermal conductivity by changing the phonon mean path and porosity takes into account compound average considering pSi as an effective medium containing crystalline Silicon and vacant pore space. Nanostructure length, extracted as a free parameter from Callaway model-fits for each pSi sample is related to it's porosity as presented in Fig. 4-9. Nanostructure lengths for all samples were interestingly found to be around $10\ nm$. This new scattering length introduced due to structuring is interpreted to play a key role in the reduction of thermal conductivity (2 orders of magnitude) with reference to bulk Silicon while compound averaging cause a further reduction with $s_\phi \approx 0.1 - 0.5$. PSi porosity with a percolation threshold of around 65% as a function of etching parameters (e.g.

electrolyte composition within etching cell) additionally contributes to the thermal conductivity reduction.

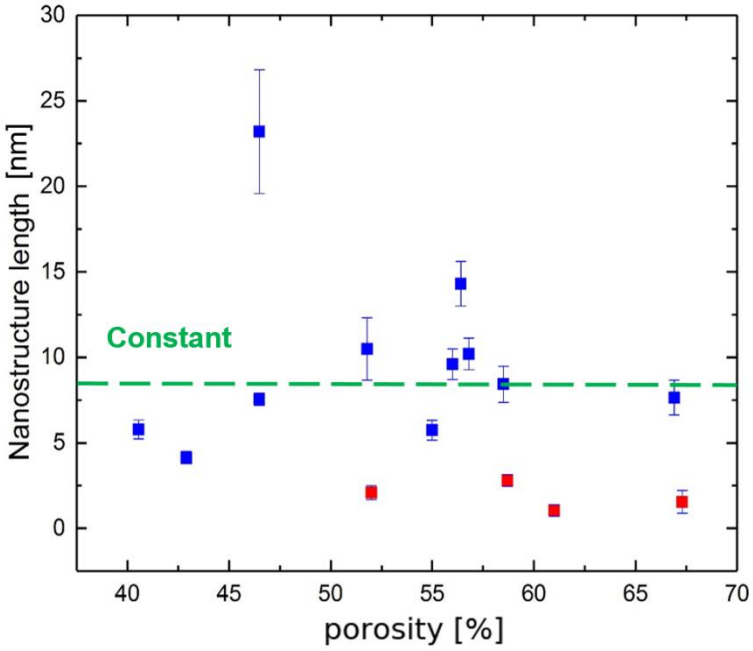

Fig. 4-9 Relation of nanostructure length and porosity of pSi samples. Green dashed line is a guide to the eye showing nanostructure length for all samples in the range of 10 ± 5 nm.

4.3.5. Amorphous limit and pSi

One should note that as seen in Fig. 4-5, LFA data of post treated pSi samples exhibit thermal conductivity of $0.5\,W/mK$ at $300K$, that is even lower than the so called amorphous limit ($1.1W/mK$) determined by Cahill [1]. This section discusses the amorphous limit reported by Cahill's Debye formulation and the amorphous limit calculated by Sine dispersion in the current work. As the name implies, amorphous limit is often discussed in the context of amorphous materials lacking long-range crystalline order. This disorder impairs the coherence of lattice vibrations and limits the mean free path to a few lattice spacings. It causes extremely low thermal conductivity and is referred to as the amorphous limit [1, 149]. In amorphous materials, the concept of extended phonon wave is not well-defined, nor is the phonon wave- vector, group velocity, or phonon mean free path. It makes thermal transport modelling in such materials quite challenging. Einstein [150] presented earlier theoretical studies on amorphous materials that was further refined by Slack [151]. Einstein's theory is based on an assumption of independent and non-correlated interatomic or lattice vibrations, in contrast to extended waves in crystalline materials. Heat conduction is governed by these independent oscillators, each with

a characteristic frequency - the Einstein frequency. Slack refined the theory by equating the minimum phonon mean free path l to be equal to phonon wavelength λ. The thermal conductivity obtained from Slack's model is known as the minimum thermal conductivity [1, 151]**.** Cahill et al. extended the model by dividing the sample into regions of size $\lambda/2$ with oscillating frequencies given by the low-frequency speed of sound, $\omega = 2\pi v/\lambda$. Cahill's model assumes $l = \lambda/2$ for each oscillator. Cahill model's physical picture is a random walk of energy between localized oscillators of various frequencies and the dominant energy transport between nearest neighbours. In the current work, amorphous limit is calculated using Eqn. 4.17 with appropriate mean free path, $l = \pi \frac{v_g}{\omega}$.

Table 4-7 enlists calculated values of minimum thermal conductivities κ_{min} of Si at $300K$ utilizing Cahill's Debye approximation and Sine dispersion. Their temperature dependence is presented in Fig. 4-5.

Table 4-7 Parameters utilized to calculate minimum thermal conductivity of Silicon at $T = 300K$: n number density of atoms, Silicon's transverse and longitudinal speeds of sound, $v_{t-Cahill}$ and $v_{l-Cahill}$, as reported by Cahill et. al. [1] and $v_{t-sine\ dispersion}$ as reported by Hofmann et. al. [2]. $\kappa_{min-Cahill}$ is the minimum thermal conductivity of Si calculated using Debye approximation. $\kappa_{min-sine\ dispersion}$ is the minimum thermal conductivity of Si calculated from sine dispersion utilizing speeds of sound reported by Hofmann et al. [2]. $\kappa_{cross-plane}$ and $\kappa_{cross-plane,post\ treated\ pSi}$ refers to the thermal conductivities of pSi and post treated pSi respectively probed by LFA, at $T = 300K$.

Parameters	Numerical values
N	$5 \times 10^{22}\ cm^{-3}$
$\boldsymbol{v_{t-Cahill}}$ $\boldsymbol{v_{t-sine\ dispersion}}$	$4370\ m/s$ $5844\ m/s$
$\boldsymbol{v_{l-Cahill}}$ $\boldsymbol{v_{l-sine\ dispersion}}$	$7360\ m/s$ $8433\ m/s$
$\boldsymbol{\kappa_{min-Cahill}}$	$0.96\ W/mK$
$\boldsymbol{\kappa_{min-sine\ dispersion}}$	$0.43\ W/mK$
$\boldsymbol{\kappa_{cross-plane}}$	$0.92\ W/mK$
$\boldsymbol{\kappa_{cross-plane,post\ treated\ pSi}}$	$0.50\ W/mK$

At $300K$, Psi samples exhibit cross-plane thermal conductivity of $0.92\ W/mK$, that is slightly lower than the so called amorphous limit ($1.1W/mK$) determined by Cahill [1] and almost twice the $\kappa_{\text{min-sine dispersion}} = 0.43W/mK$ calculated from sine dispersion utilizing speeds of sound reported by Hofmann et al. [2]. Post treated pSi samples exhibit thermal conductivity of $0.5\ W/mK$ at $300K$, that is lower than the so called amorphous limit ($1.1W/mK$) determined by Cahill [1] and almost equal to $\kappa_{\text{min-sine dispersion}} = 0.43W/mK$. Cahill uses linear phonon dispersion proposed by Debye based on acoustic-elastic wave assumption. However, this assumption does not consider the periodic boundary condition's effect on the phonon dispersion creating standing waves at Brillouin boundaries, as reported by Born von Karman [152]. It leads to a deviation of Debye dispersion for phonon transport close to the Brillouin boundaries, hence overestimating lattice thermal conductivity because of the overestimation of the group velocity of these high-frequency phonons [152]. Moreover, it overestimates minimum thermal conductivity leading to the violation of measured thermal conductivity even lower than Cahill's minimum thermal conductivity, as also evident for the measured thermal conductivity values of as-etched and post-treated pSi. Minimum thermal conductivity determined in our work utilizing sine dispersion shows a deviation from Cahill's by a factor of two, i.e. $\kappa_{\text{min-sine dispersion}} = \frac{1}{2}\kappa_{min-Cahill}$. This result removes the contradiction of the measured thermal conductivity of pSi being lower than the minimum thermal conductivity. Moreover, it opens further prospects for developing thermally resistive materials for applications such as thermoelectrics.

4.3.6. Modelling of in-plane thermal conductivity ($T = 2K - 300K$)

Thermal conductivity with $\kappa \sim T^1$ dependence in a temperature range of $T = 2K - 300K$ was initially analyzed in the current work by utilizing 2D Debye DOS combined with mean free path $\lambda_{mean} \propto \omega^{-1}$ with $\Theta_D^{2D} = 140K$ as a fixed parameter (value extracted from specific heat capacity data analysis). Experimental data and the model fit are presented in Fig. 4-10 (a), where the contribution of 2D Debye DOS is evident for $T < 50K$. As a second step, treating the data by utilizing 3D DOS combined with phonon mean free path $\lambda_{mean} \propto \omega^{-2}$ with $\Theta_D^{3D} = 697K$ leads to quite good agreement of experimental data and the model fit up to $200K$ (Fig. 4-10 (b)) considering frequency-dependent nanostructure scattering. In our speculative interpretation, thermal conductivity for $T > 200K$ could be attributed to diffusive heat transport through Einstein surface modes governed by Eqn. 4.31 [153] where D encodes thermal diffusivity and T_E is the Einstein temperature.

$$\kappa_{diffusion} = D * \left(\frac{T_E}{T}\right)^2 \frac{e^{\frac{T_E}{T}}}{\left(e^{\frac{T_E}{T}} - 1\right)^2} \tag{4.31}$$

Subsequently, combination of 3D Debye DOS model with harmonic oscillator ($166\ meV$) as a third step leads to excellent agreement of experimental data and the model-fit as evident in Fig. 4-11. In diffusive thermal transport, heat is quantized by non-propogating atomic vibrations termed as *diffusons*, characterized by diffusivity [153]. The diffuson theory of Allen and Feldman explains diffusive thermal transport as the harmonic coupling between non-propagating (i.e., unlike phonons) atomic vibrations [153]. Recently, Mathias et al., in their work, proposed that *diffusons* may better describe heat transfer in amorphous, disordered and even nanomaterials, particularly at high temperatures [154]. Earlier, Dell'Anna et al. attributed the "re-increase" of thermal conductivity of amorphous silicon above the plateau region to heat carried by "*diffuson*" modes [155]. ω dependent scattering was also reported in [153] for vitreous silica where the role of these modes is explained in terms of diffusive heat transport. In a contemporary studies, Sette et al. [156] confirmed ω^{-2} dependent diffusivity of these modes by numerical calculations.

Concluding, 'excess' specific heat capacity of pSi, at low temperature ($T < 50K$) is interpreted to be due to acoustic phonon modes on the surface of pSi and an additional Einstein contribution C_E^{2D}. The origin of C_E^{2D} is attributed to a boson peak of amorphous SiO_2 in pSi [130]. At temperature range of $T = 300 - 640K$, 3D DOS dominates as interpreted from temperature dependent data analysis of specific heat capacity and thermal conductivity.

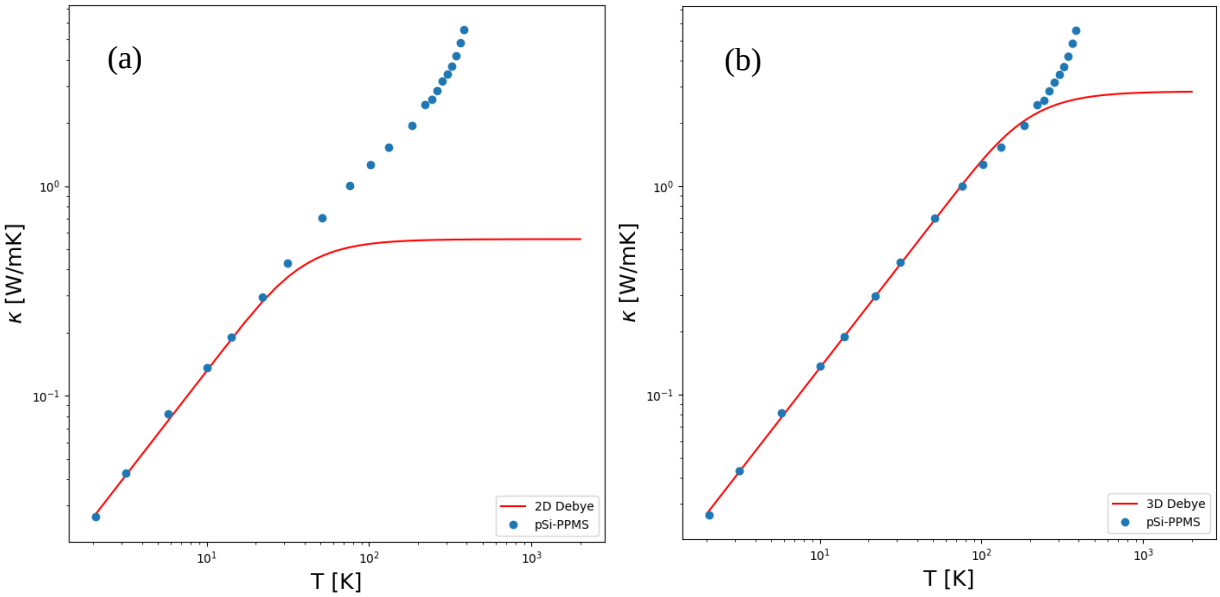

Fig. 4-10 Temperature dependent thermal conductivity of pSi (blud dots) probed by PPMS. Red line in (a) represents 2D Debye model-fit ($\Theta_D^{2D} = 140K, \lambda_{mean} \propto \omega^{-1}$) up to $50K$ and (b) represents 3D Debye model-fit ($\Theta_D^{3D} = 697K, \lambda_{mean} \propto \omega^{-2}$) up to $T = 200K$.

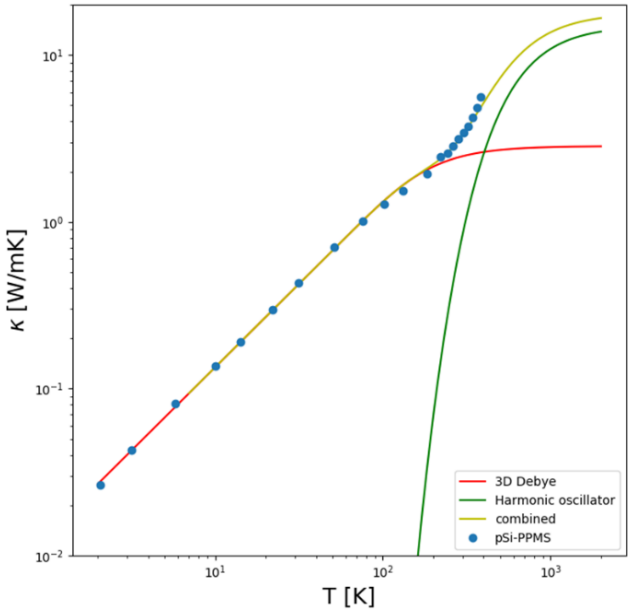

Fig. 4-11 Temperature dependent thermal conductivity of pSi modelled with 3D Debye (Red line) and harmonic oscillator (Green line) contribution. Yellow line represents their combined contribution agreeing excellently with experimental data up to $400K$ *(blue dots).*

4.4. Electrical transport in pSi

Despite the widespread attention awarded to pSi, there has been little agreement on any predominant charge transport mechanism in pSi [42]. Reported studies have proposed different charge transport mechanisms [45, 157-160]. Models based on extended states transport [161], phonon-assisted hopping [108] and charge carrier tunneling to localized states near band edges [162] are few examples.

This section presents temperature-dependent electrical conductivity and thermopower measurements on a multitude of different pSi samples. The detailed data analysis will identify multi-phonon absorption as the underlying process that defines pSi's electronic properties.

The earliest reports on the electrical transport in pSi were about its low electrical conductivity compared to bulk Si [157]. In the current work, pSi exhibits the electrical conductivity of up to seven orders of magnitude lower than the corresponding p-doped Silicon source wafer ($\sigma = 50 - 100\ Scm^{-1}$) at $T = 300K$ (Section. 4.4.1, Fig. 4-13).

The conductivity of p-doped Si wafers shows a temperature dependence as expected for highly doped semiconductors (Section. 4.4.1, Fig. 4-13 inset). Increased phonon scattering rate reduces the mobility of the holes at higher temperatures. Consequently $\sigma(T)$ decreases in the extrinsic

region ($T > 100K$) [126]. In contrast, pSi shows thermally activated charge transport (Fig. 4-13) in the probed temperature range ($T > 300K$).

Structural disorder in pSi creates localized states in pSi known as Anderson states [163]. These additional trap centers create band tails that are not restricted to the surface. The disordered nanostructure also introduces new scattering centers for charge carriers. It reduces the mean free path for hole transport and hence electrical conductivity. Surface effects and intrinsic disorder alter the band structure of pSi. It resembles to that of amorphous silicon containing gap states and band tails [164].

An increase in bandgap from $E_g^{Si} = 1.14eV$ in bulk Si to $E_g^{pSi} = 1.46eV$ in pSi upon nano-structuring is depicted in UV-vis spectra (Fig. 4-12). This is attributed to charge carrier confinement in small dimensional crystalline pore walls that increases the bandgap.

As reported by Lehmann et al., these regions (i.e pore walls) can be considered as quantum wires with a diameter D or in a further approximation, with a square cross-sectional box of the side length D. Utilizing particle-in-a-box approximation, the net increase in band gap energy, ΔE can be expressed as:

$\Delta E = \frac{h^2}{8m^* D^2} = E_g^{pSi} - E_g^{Si} = \Delta E_v + \Delta E_c$ where $h = 4.13 \times 10^{-15} eVs$ is Plank's constant and m^* = denotes effective hole mass (m_h^*) and effective electron mass (m_e^*) for ΔE_v and ΔE_c, respectively. ΔE expression allows the estimation of pore wall thickness $D \approx 9\,nm$ for pSi samples knowing $\Delta E = E_g^{pSi} - E_g^{Si} = 0.32\,eV$ through UV-vis spectra.

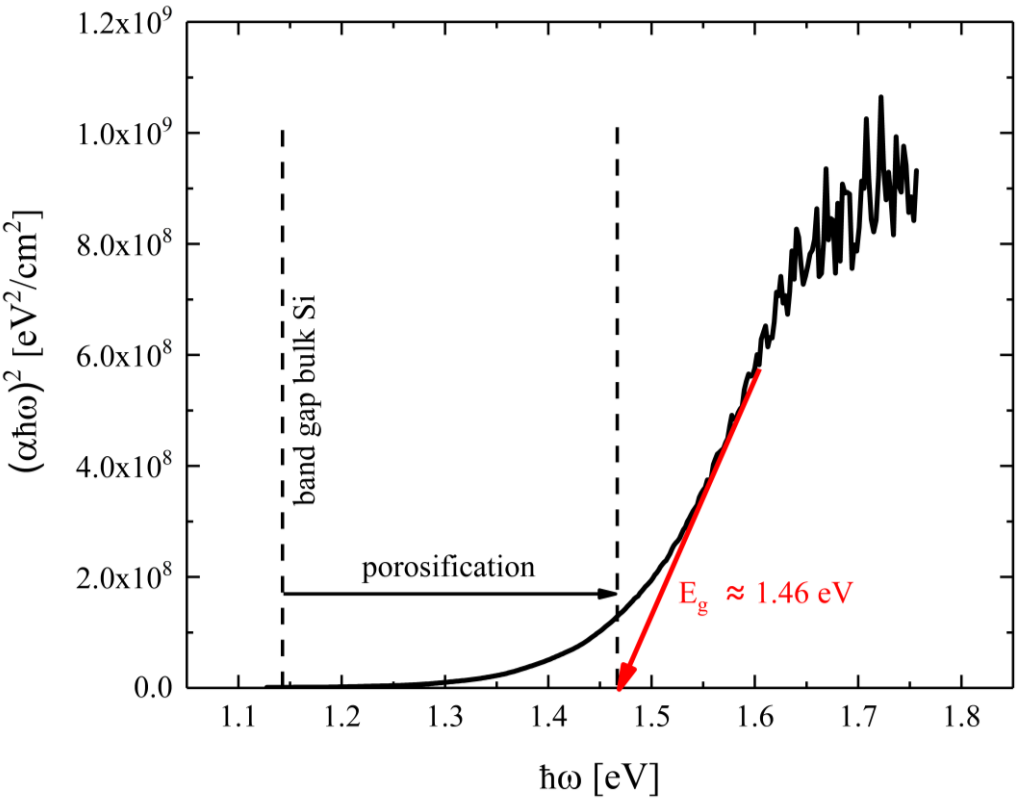

Fig. 4-12 Optical bandgap in pSi at $T = 300K$. The so-called tauc-plot exhibits the dependence of the absorbance α on the incident photon energy $\hbar\omega$. Optical bandgap of pSi 1.46eV and bSi 1.14eV are marked.

4.3.7. Thermaly activated charge transport and Meyer Neldel Rule (MNR) in pSi

Temperature dependent electrical conductivity measurements of pSi showed thermally activated charge transport behavior governed by Eqn. 4.32 where E_A^σ is activation energy and σ_0 is a high temperature limit for electrical conductivity. For each sample, E_A^σ and σ_0 were extracted by fitting the experimental data to Eqn. 4.32 as shown in Fig. 4-13.

$$\sigma = \sigma_0 exp\left(-E_A^\sigma \Big/ k_B T\right) \tag{4.32}$$

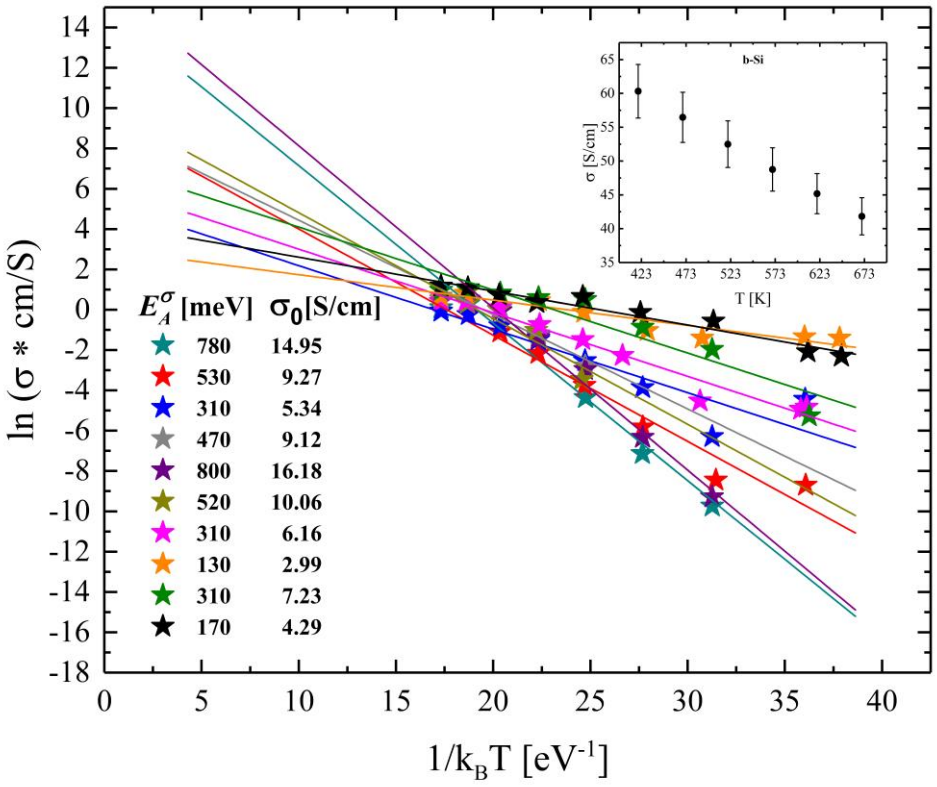

Fig. 4-13 Temperature dependence of electrical conductivity of porous Silicon samples. Solid lines are best fits to Eqn 4.32 in an Arrhenius representation along with E_A^σ and σ_0 values extracted for each sample. The two data columns are the optimized model parameters. Error bars are of a similar size than the symbols. The inset shows the T-dependent conductivity of bulk Silicon.

E_A^σ values in the range of $100 - 800\ meV$ were found to be in close agreement to that reviewed by Leigh Canham in 'Handbook of porous Silicon' [42]. Porosity in the range of $40 - 60\%$ and pore radius $(4 - 6nm)$ did not show any correlation with E_A^σ. A quantity expected to influence E_A^σ directly is the conductivity of the source wafers that is related to the hole density. Electrical conductivity of source wafers was in the range of $50 - 100\ Scm^{-1}$. Variation of temperature dependent electrical conductivity from wafer to wafer could lead very well to the different activation energies**.** However, irrespective of different activation energies, all data sets and their non-linear least square fits intersect at one single point with a reasonable margin of error. This refers to the so-called Meyer-Neldel rule (MNR) that relates E_A^σ and σ_0 values extracted from least square approximation fits in Fig. 4-13. This linear correlation of $ln\sigma_0$ against E_A^σ is presented in Fig. 4-14. MNR is followed when an increased activation energy in a thermally activated charge transport is compensated by an exponential increase of σ_0 with E_A^σ (Eqn. 4.33)

$$\sigma_0 = \sigma_{00} exp\left(E_A^{\sigma}/E_{MN}\right) \tag{4.33}$$

here σ_{00} is a constant, $E_{MN} = k_B T_{MN}$ is termed as Meyer Neldel (MN) energy where T_{MN} denotes isokinetic characteristic MN temperature.

From the slope of the MNR model fit in Fig. 4-14, one can extract E_{MN}. For our pSi samples, it is found to be $58\ meV$ that interestingly corresponds to maximum in the phonon density of states (DOS) of Silicon [165]. MNR for thermally activated electrical conductivity, atomic diffusion or thermal emission of charge carriers are intensively studied in the contemporary scientific literature [161, 166-170]. For charge transport in pSi, MNR and the characteristic MN energy $E_{MN} = 58\ meV$ in pSi is explained in the context of level-shift, entropy [170, 171] and phonon assisted hopping.

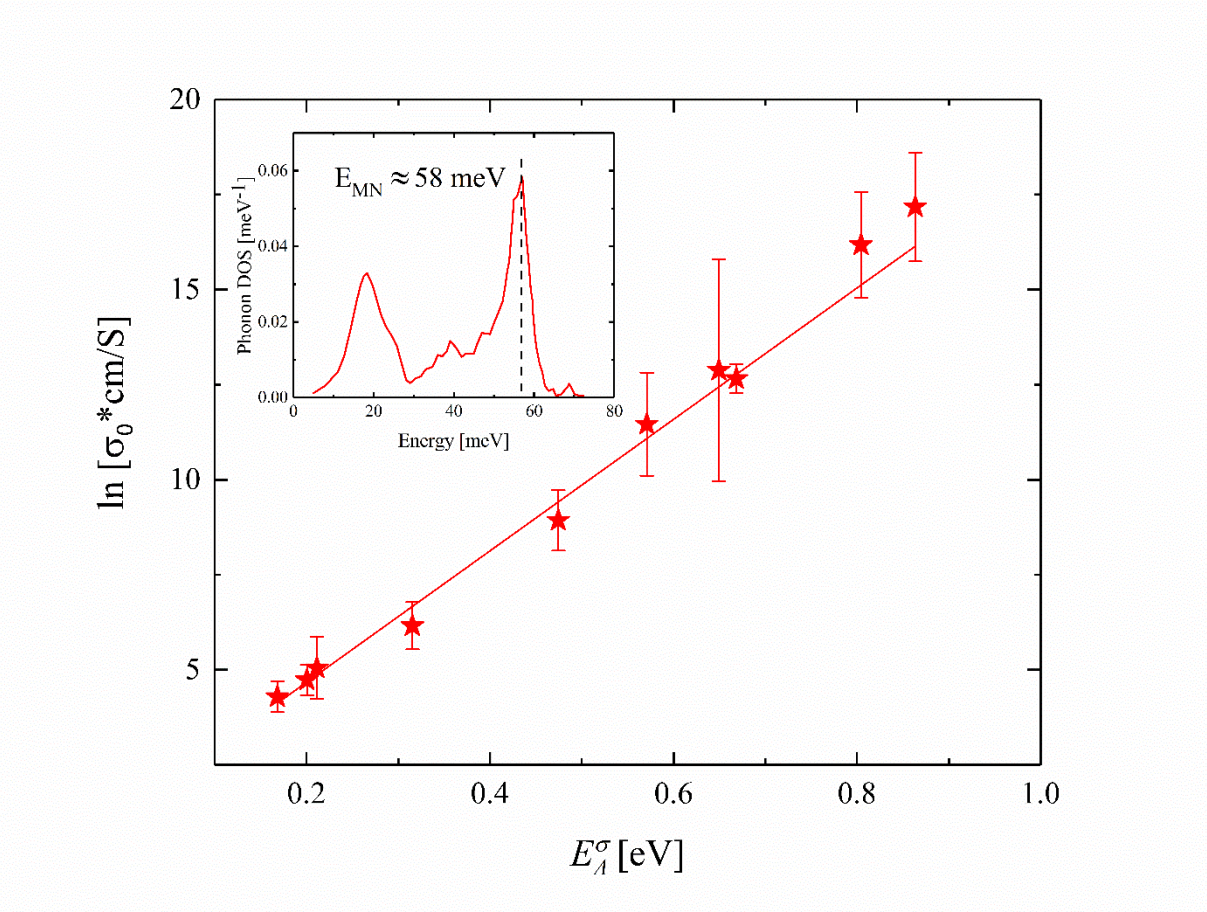

Fig. 4-14 Experimentally determined values of σ_0 as a function of corresponding E_A^{σ} for each pSi sample. Solid straight line is a best fit to MNR (Eqn. 4.17). $E_{MN} = 58\ meV$ determined from inverse of slope of straight line agrees well with maximum in Silicon phonon density of states (inset).

4.3.8. MNR and level-shift model

Level-shift models relate the MNR to a temperature-dependent Fermi level and a tailored electron density of states that causes this temperature dependence governed by Eqn. 4.34 where E_F refers to Fermi level and conduction band is denoted by E_C.

$$\sigma(T) = \sigma_{00} exp\left(\frac{\delta E_F\,(T)}{k_B T}\right) exp\left(\frac{E_C - E_F\,(T=0)}{k_B T}\right) \tag{4.34}$$

In Eqn. 4.34, temperature dependence of Fermi level, $E_F\,(T)$ is related to the temperature dependent occupation of the states [172] and explains MNR in disordered semiconductors such as a-Si:H [159]. The second term in Eqn. 4.34 is referred as compensation factor.

4.3.9. MNR and multi excitations entropy (MEE) model

In the MEE-based model framework, Yelon et al. considered charge transport as a thermodynamic activation process to explain MNR [171]. The Gibbs free energy G is identified as the appropriate thermodynamic potential. The activation rate of this process is $X \propto exp(\Delta G/k_B T)$. With the fundamental relation between the Gibbs free energy G, the enthalpy H and entropy S of the system, it is $X \propto exp(\Delta S/k_B) \times exp(-\Delta H/k_B T)$ and the derivation of the MNR is complete with $\Delta H = E_A$ and $\Delta S/k_B = \Delta H/E_{MN}$.

The reasoning relies on an intuitive argument. Many elementary excitations (e.g. phonons) must be absorbed in a thermal fluctuation to overcome activation energy, which is much larger than the thermal energy $k_B T$ and the energy of the individual excitations itself. Consequently, the absorption process comes along with a large 'selection' entropy ΔS as there are multiple ways to absorb the required number of phonons. It is this entropy that increases with activation energy and causes the compensation factor in the MNR [170, 171]. In this picture, the characteristic E_{MN} was reported to be that of excitations, which in the present context is typical of optical phonons [170]. Upon applying the MEE model in the MNR framework to a closely related material to pSi, i.e., a-Si:H, its E_{MN} was found to be 30 meV, which equals the typical optical phonon energy in the material [168]. However, for a-Si:H materials with high defect concentration, the MEE model did not explain obtained E_{MN} values much larger than the optical

phonon energy. Instead, the level shifts model accounted for a more detailed MNR behaviour in *a*-Si:H [173, 174]. Balberg et al. compiled the data of pSi from various research groups together with the data of *a*-Si:H [168, 175]. Within the MNR framework, they proposed the presence of 'only two' different charge transport mechanisms. It was manifested by two best-fit well-separated MNR lines representing all data points (Fig. 4-15).

One was associated with extended-states transport via band tails [176] as found in a-Si:H (upper line), and the second was associated with activated hopping via intercrystallite hopping (lower line). However**,** they could not distinguish the hopping mechanisms in the level-shift and MEE model frameworks. They did not comment on E_{MN} in relation to the phonon DOS. In contrast, M. Ben Chorin et al. advocated hopping conduction in pSi through energy states close to Fermi level [177].

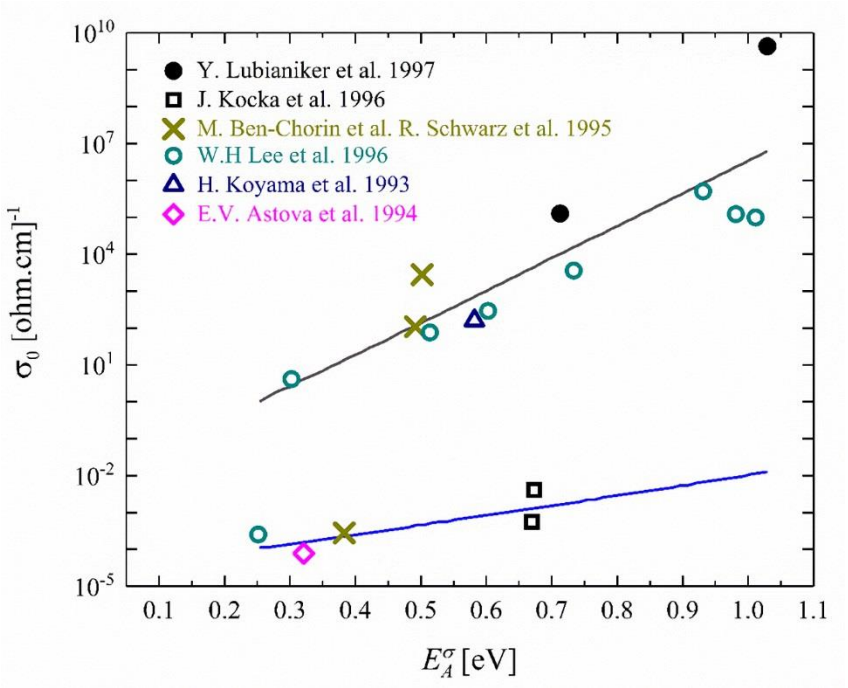

Fig. 4-15 Experimentally determined values σ_0 of as a function of the corresponding E_A^σ values in a variety of porous silicon samples. The sources of the data are mentioned in the figure. The solid lines represent the best fit to a MNR. Upper line shows transport in extended states, and lower line refers to charge transport by activated hopping.

4.3.10. MNR and phononic assisted hopping models

Yelon et al. drew additional confidence in their models from Emin's microscopic optical-phonon assisted charge hopping models [170]. Emin derived the multi-phonon assisted hopping rate (polaronic hopping rate) for a two-site model in an impressively extended calculation [178]. This hopping rate includes a compensation factor and allows to assign Meyer-Neldel energy as:

$$E_{MN} = \frac{\hbar\omega_0}{\ln(M)} \quad , \quad M = \frac{2M_{e-p}}{\hbar\omega_0} \tag{4.36}$$

Here, ω_0 is dispersionless optical phonon energy, and M is the electron-phonon coupling strength.

In the MEE framework, one is tempted to explain the MNR in pSi by multi-phonon absorption as the underlying mechanism of a thermally activated carrier transport in localized states. The phonon dispersion of Si/pSi has an energy cutoff at around $70\,meV$ (Fig. 4-14). Multiple phonons are necessary to account for the activation energies $E_A^{\sigma} \gg k_B T$ required for charge transport. The MEE interpretation is appealing considering the exceptional agreement between the Meyer-Neldel energy and the maximum in the optical phonon density of states of Si respectively pSi.

In this context, it is important to note that MEE theory only predicts a proportionality and not equality between E_{MN} and the energy of the elementary excitation, whose details depend on the microscopic model (see Eqn. 4.36). Assuming $E_{MN} = \hbar\omega_0 = 58\,meV$, a hole phonon coupling of $M_{H-p} = 78\,meV$ was estimated for pSi samples (for p-doped samples, charge transport is via holes and therefore coupling constant is denoted here by holes and phonons) in the current work. The origin of polaronic coupling holes and phonons in the current interpretation is attributed to amorphous silicon oxide that covers the internal surfaces of pSi. Silicon itself is not polar, and therefore it is unlikely for pure Si to exhibit polaronic charge transport. Moreover, the validity of the MEE model and its justification from comparing it with two site jump models for polaronic transport rates in disordered materials is heavily debated. In a nutshell, Fishchuk et al. argue that the two-site model of Emin is not sufficient to justify a macroscopic MNR in a disordered system within the MEE models [179].

Consequently, one must resort to additional arguments rather than relying on MNR interpretation in the context of MEE models to conclude that multi-phonon absorption plays a vital role in the microscopic charge transport in nanostructured pSi.

For deeper insight, experimental data of temperature dependent thermopower was analyzed. It proved more stringently that charge transport occurs by hopping in localized states assisted by several phonons' absorption. The thermopower of non-degenerate semiconductors and amorphous semiconductors depends linearly on the inverse temperature (Eqn. 4.37). In Eqn.

4.37, E_A^S is characterizing activation energy for charge transport while *A* encodes details of the scattering mechanisms [180].

$$S(T) = \frac{k_B}{e}\left(\frac{E_a^S}{k_B T} + A\right) \tag{4.37}$$

Fig. 4-16 shows experimental data of Seebeck coefficient against *1/T* of pSi samples along with least-squares approximations based on Eqn. 4.37. The positive sign of the thermopower evidences hole transport in pSi.

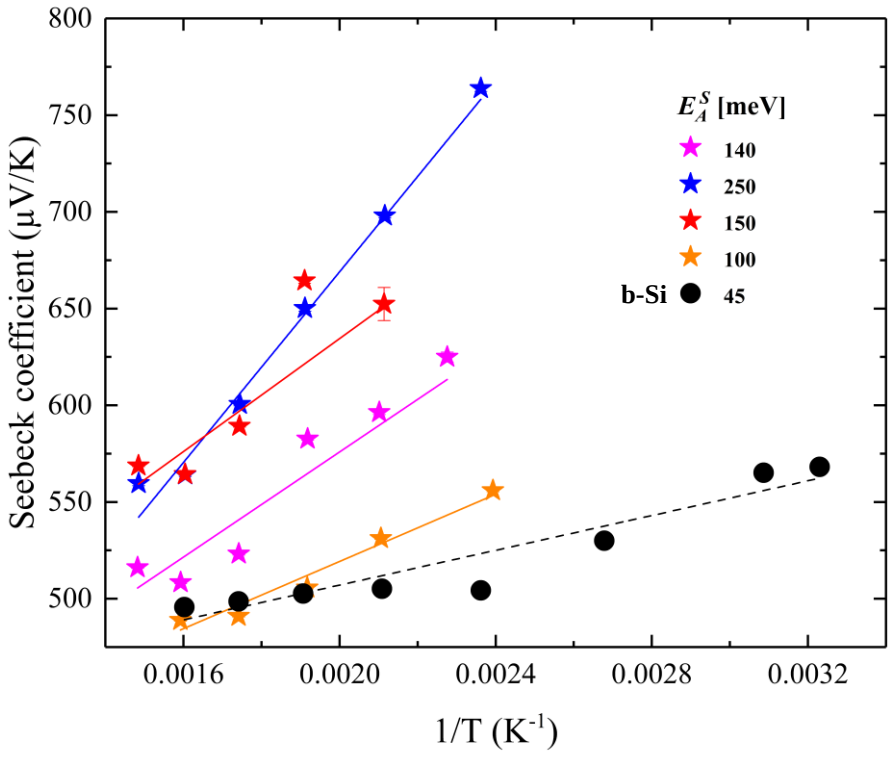

Fig. 4-16 Temperature dependence of Seebeck coefficient of pSi sample. Solid straight line represents a model fit to Eqn. 4.37. Dashed line corresponds to absolute Seebeck coefficient of bulk Silicon.

For bulk Silicon, E_A^S = 45 meV is found in excellent agreement with the energy of the boron donor level in the Silicon band gap [126]. For all pSi samples, E_A^S extracted from Seebeck data was found to be lower than that found from electrical conductivity data (Table 4-8). This trivial observation provides important insight into the charge transport mechanism in pSi. For charge transport in extended states, $E_A^S \equiv E_A^\sigma$. However for transport in localized states via hopping, it is $E_A^S < E_A^\sigma$. The hopping manifests in an exponential temperature dependent $exp(-E_{hop}/k_B T)$ of the mobility. The hopping energy E_{hop} defines the required population of phonon

states. This exponential term enters linearly the two thermoelectric transport coefficients L_{11} and L_{12} whose ratio defines the thermopower $S \propto {}^{L_{11}}/_{L_{12}}$. The absorption/emission of phonons during the hopping process does not alter the transported entropy per carrier, which is proportional to the thermopower S.

Table 4-8 Activation energies for electrical conductivity and thermopower

Sample	1	2	3	4	5	6	7	8	9	10
$\boldsymbol{E_A^\sigma [meV]}$	781 ± 76	527 ± 64	315 ± 59	468 ± 80	804 ± 57	524 ± 120	315 ± 23	126 ± 17	312 ± 47	168 ± 15
$\boldsymbol{E_A^S}$ $\boldsymbol{[meV]}$	460 ± 92	150 ± 65	100 ± 57	250 ± 16	410 ± 52	100 ± 77	140 ± 34	100 ± 10	100 ± 26	100 ± 11
$\boldsymbol{E_A^\sigma - E_A^S}$ $\boldsymbol{[meV]}$	321 ± 119	377 ± 92	65 ± 61	368 ± 98	394 ± 77	425 ± 142	175 ± 42	26 ± 20	212 ± 54	68 ± 19

Concluding, porosification alters significantly the electronic transport mechanism in crystalline Silicon. Highly p-doped Silicon wafers exhibit the typical conductivity of non-degenerate semiconductors with carrier transport in extended states. Increasing temperature increases the hole-phonon scattering rates and thus reduces the carrier mobility respectively σ.

Porosification leads to significant charge carrier depletion due to gap states, localized Anderson states in the band tails and band bending at the huge internal interfaces. Electrical conductivity measurements reveal a Meyer-Neldel compensation rule for the thermally activated transport. It readily relates to multi-pohonon absorption and transport in localized Anderson states.

Temperature dependent thermopower measurements' data show activation energies significantly smaller than the ones necessary for current flow. It implies a carrier mobility that depends on the temperature dependent phonon state population.

5. Conclusion

In this chapter, the main scientific insights are concluded as following:

Phonon dispersion in pSi

The inelastic neutron scattering studies in the thesis present new scientific insights about the influence of nanostructuring on the phonon dynamics in single crystalline silicon. Nanostructuring on sub-10 nanometer length scales does not affect the phonon dispersion. In contrast to Si nanoribbons and nanotubes, no sizable phonon-softening in pSi was observed in the inelastic neutron scattering experiments. Nanostructuring induced phonon softening appears as a prerequisite to beat the so-called amorphous limit [6] of 0.1 in pSi. A retrospective of the presented results require samples with even higher porosity and smaller structural feature sizes, which cannot guarantee mechanical stability.

Thermal transport in pSi

Temperature-dependent specific heat and thermal conductivity measurements presented in the thesis provided insights into static and dynamic thermal transport properties of nanostructured pSi. A noncharacteristic low-temperature specific heat $C_p \neq constant \times T^3$ was identified for pSi. To model non-traditional C_p, additional 2D Debye and 2D Einstein contribution of specific heat in pSi was considered. Their combined contribution in the model-fit evidenced excellent agreement with experimental data. The origin of the 2D Debye modes was attributed to surface modes and 2D Einstein modes to the boson peak of SiO_2 in pSi.

PSi exhibited a reduction in thermal conductivity by two orders of magnitude compared to bulk Si (150 W/mK at 300K). It indicated a strong effect of nanostructuring on phonon scattering rates in pSi. Phonon dispersion results of pSi obtained from neutron scattering experiments were followed by in-depth analysis of phonon dynamics. Data analysis considered the compound average of pSi pores and new scattering length introduced in a system upon nanostructuring by a combination of Callaway and Effective medium models. It was interpreted that nanostructuring at sub-10 nanometer cause the thermal conductivity reduction by two orders of magnitude in pSi while compound averaging causes a further reduction with $s_\phi \approx 0.1 - 0.5$.

Electronic transport in pSi

Nanostructuring caused the reduction of electrical conductivity of pSi by seven orders of magnitude compared to bulk Si. This reduction was attributed to charge carrier depletion through interface trapping and scattering at rough surfaces in pSi. The electrical conductivity in mesoporous silicon was found to be thermally activated with activation energies up to almost 1eV. Electrical conductivity measurements revealed a Meyer-Neldel compensation rule for thermally activated transport. It readily relates to multi-phonon absorption and transport in localized Anderson states. Temperature-dependent thermopower measurements further evidenced multi-phonon assisted transport in pSi. Thermopower data showed activation energies smaller than the ones obtained from electrical conductivity data. It implies carrier mobility that depends on the temperature-dependent phonon state population.

Overall conclusion

This thesis provide novel insights into macro and microscopic charge carrier and heat transport mechanisms in pSi. As such, it is of interest for fundamental science as well as applied science. In particular, material scientists who seek to develop pSi/nanostructured Si-based energy materials, e.g. super-capacitors or thermoelectrics, will benefit from this study.

Appendices

Appendix A: Post-processing of as-etched pSi

Robust chemical post treatment method is developed to increase the pore diameter of pSi between 10-21 nm as discussed in chapter 2. The left panel of Fig.1 shows a selection of nitrogen sorption isotherms measured on as-etched and post-treated pSi membranes. It depicts modified sorption behavior of the porous membranes upon different post-treatments. The visually most striking feature is the shift of adsorption and desorption branches towards higher reduced pressures with increasing number of post treatment cycles. One cycle refers to 30 minutes oxidization treatment of pSi membranes by dipping in hydrogen peroxide (H_2O_2)

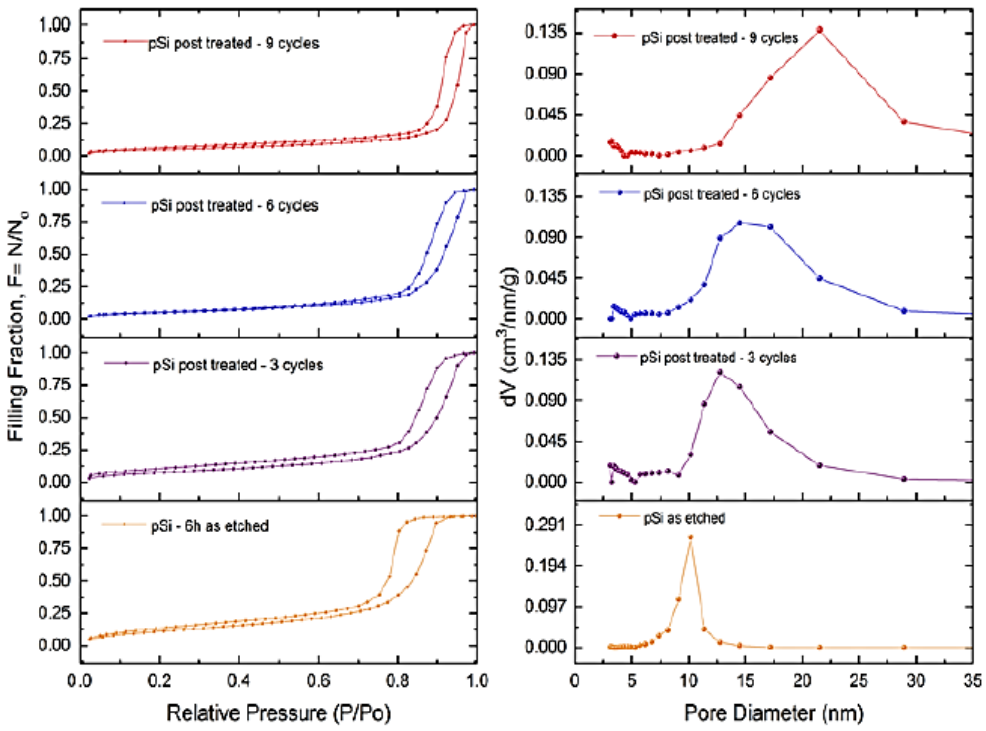

Fig. 1 Nitrogen sorption Isotherms and pore size distribution: the left panel shows isotherms for as etched and post treated samples. The right panel relates the isotherms to the pore size distributions.

followed by 30 minutes in hydrofluoric acid (HF). It readily encodes changes in the membranes' pore size distribution (PSD). The right panel of Fig. 1 shows accordingly PSDs extracted from the isotherms by means of BJH-analysis [3] of the desorption branches. The as-etched sample has a pore size distribution centered around 10 nm obtained from sorption measurements.

Already three cycles of post-treatment shift it towards 14 nm. After six and nine cycles, average pore sizes around 16 nm and 21 nm are achieved. For comparison, we note that a one-step post-treatment exposing the samples for 10 hours to H_2O_2 and 10 hours to HF leads only to an average pore size of 15 nm. Table 1 lists morphological parameters extracted from the isotherms. Specific surface area, porosity and pore diameter are given for as-etched and post-treated samples.

Table 1 Morphological parameters of differently treated samples

Sample 1	As-etched	3 cycles	6 cycles	9 cycles
Pore diameter d [nm]	10	14	16	21
Surface [m^2/g]	239	314	343	373
Porosity [%]	57	72	77	84

Appendix B: Macroscopic thermoelectric measurements of pSi

Thermoelectric measurements of pSi were performed for various samples synthesized with varied etching time (4h-6h). The scatter is prominent in temperature dependent thermopower denoted by Seebeck coefficient, electrical conductivity and thermal conductivity measurements. Electrical conductivity shows thermally activated charge transport. Figure of merit shows only a slight increase from 0.01 to 0.04 with respect to temperature.

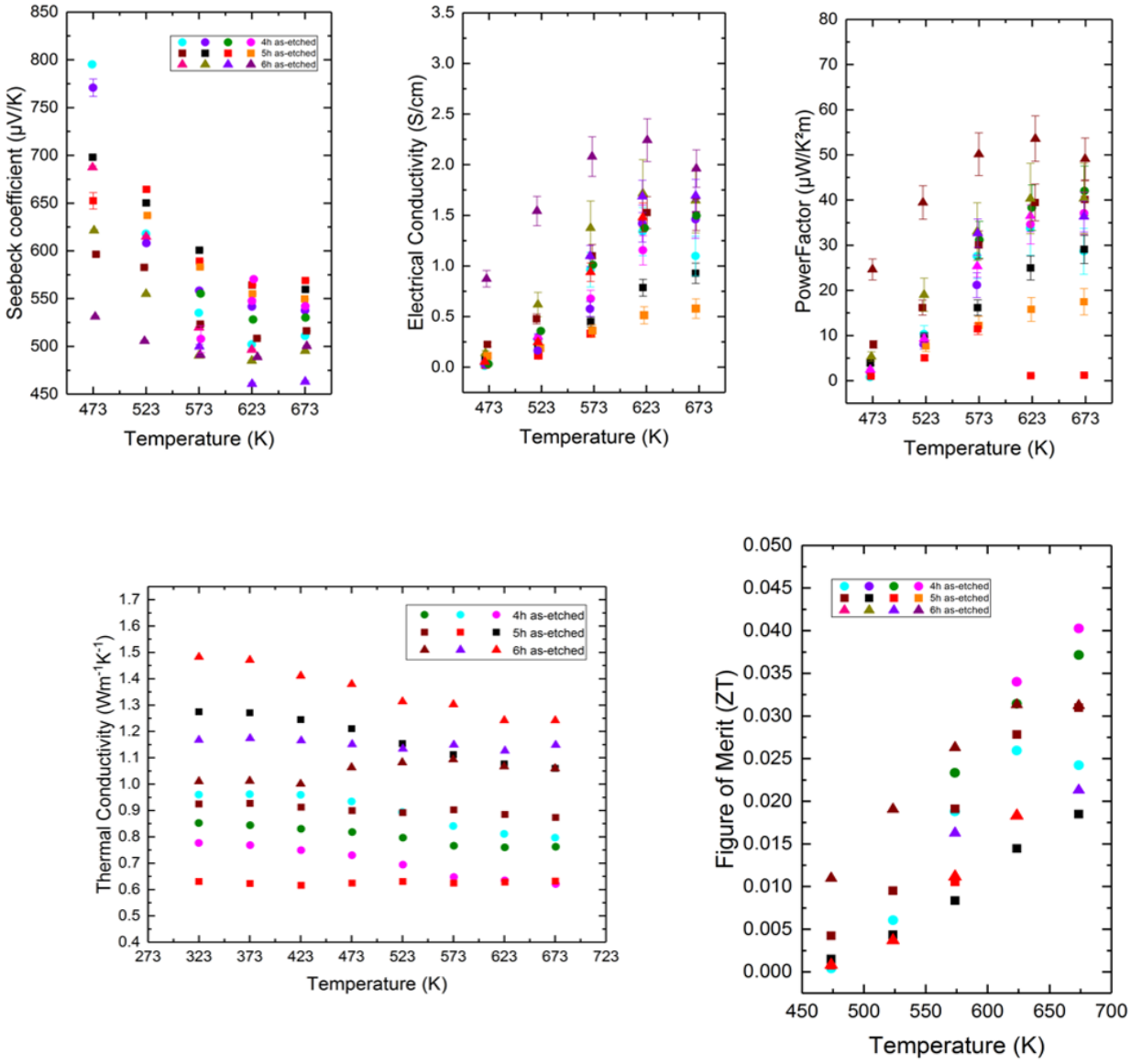

Fig. 2 Temperature dependent Seebeck coefficient, electrical conductivity, power factor, thermal conductivity and Figure of Merit of as- etched pSi samples with 4-6h etching time as indicated in legends.

Appendix C: Thermal conductivity – PPMS vs. LFA or inplane vs. crossplane

Inplane-crossplane anisotropy in pSi's thermal conductivity is identified in current work as depicted in Fig. 3. Thermal conductivity measurements by other methods in future (e.g. 3ω method) in common temperature range may provide interesting insights into thermal transport of pSi for a wide temperature range.

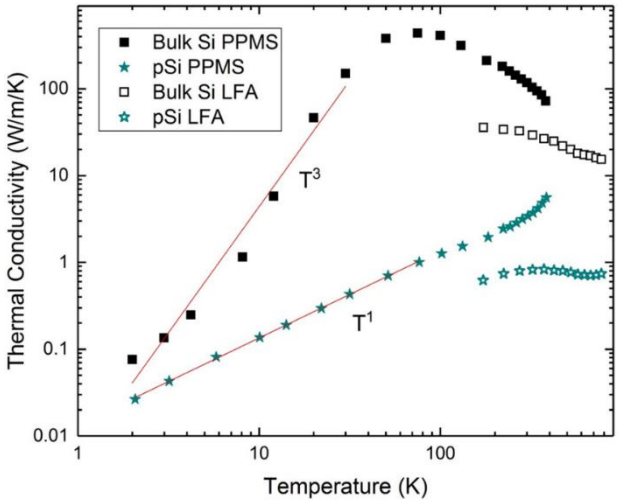

Fig. 3 Inplane and crossplane thermal conductivity of pSi and bulk Si probed by PPMS and LFA respectively.

Appendix D: pSi band gap estimation from UV-vis

The spatial confinement of carriers in a crystalline Si skeleton with nanometer-sized walls increases the bandgap in pSi significantly. Bulk Si exhibits a bandgap of 1.14 eV at 302 K and therefore absorbs light with a wavelength below 1200 nm. This absorption threshold is red-shifted for pSi. This effect becomes most prominent in UV-vis spectra. PSi band gap values obtained from UV-vis experiments for all as-etched samples was found to be 1.4 eV as labelled in Fig.4.

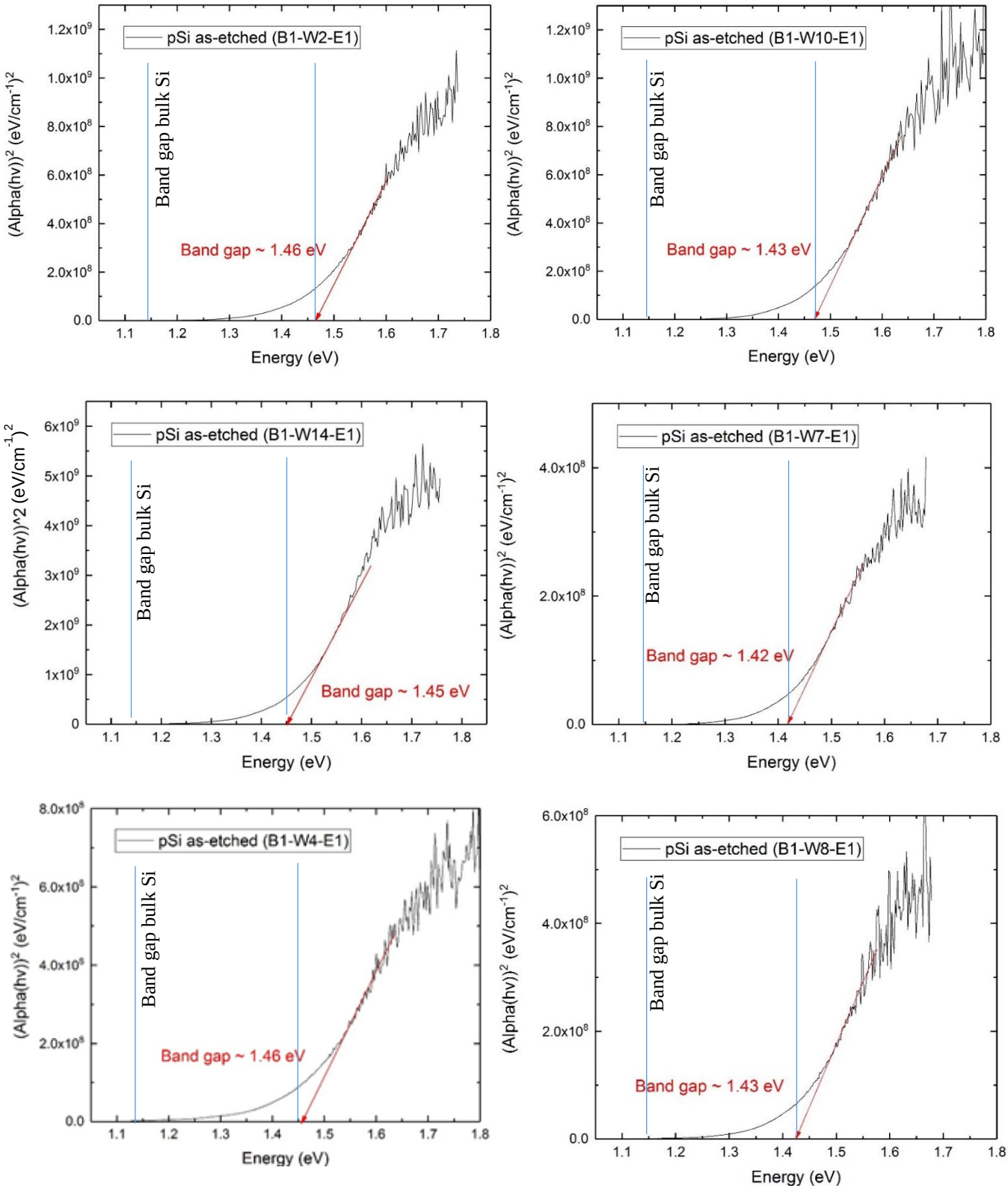

Fig.4 Optical bandgap in pSi samples at T = 300K: The so-called tauc-plot exhibits the dependence of the absorbance α on the incident photon energy ħω. The arrow marks the optical bandgap of around 1.4 eV for all pSi samples.

References

1. Cahill, D., S. Watson, and R. Pohl, *Lower Limit to the Thermal Conductivity of Disordered Crystals.* Physical review. B, Condensed matter, 1992. **46**: p. 6131-6140.
2. Hofmann, T., et al., *Phonons in mesoporous silicon: The influence of nanostructuring on the dispersion in the Debye regime.* Microporous and Mesoporous Materials, 2017. **243**: p. 263-270.
3. Bogdanov, D., et al., *Low-cost renewable electricity as the key driver of the global energy transition towards sustainability.* Energy, 2021. **227**: p. 120467.
4. Ryu, H., H.-J. Yoon, and S.-W. Kim, *Hybrid Energy Harvesters: Toward Sustainable Energy Harvesting.* Advanced Materials, 2019. **31**(34): p. 1802898.
5. Ellabban, O., H. Abu-Rub, and F. Blaabjerg, *Renewable energy resources: Current status, future prospects and their enabling technology.* Renewable and sustainable energy reviews, 2014. **39**: p. 748-764.
6. Krischer, K. and K. Schönleber, *Physics of energy conversion*. 2015: De Gruyter.
7. Hubbert, M.K., *Energy from fossil fuels.* Science, 1949. **109**(2823): p. 103-109.
8. Secretariat, R., *Renewables 2012 global status report.* Rep Paris: REN12, 2012.
9. Kalghatgi, G., *Development of Fuel/Engine Systems—The Way Forward to Sustainable Transport.* Engineering, 2019. **5**(3): p. 510-518.
10. Tritt, T.M., *Thermoelectric Phenomena, Materials, and Applications.* Annual Review of Materials Research, 2011. **41**(1): p. 433-448.
11. Snyder, G.J. and E.S. Toberer, *Complex thermoelectric materials.* Nature Materials, 2008. **7**(2): p. 105-114.
12. Goupil, C., et al., *Thermodynamics and Thermoelectricity*, in *Continuum Theory andModeling of Thermoelectric Elements*. 2016. p. 1-74.
13. Rowe, D.M., *Modules, systems, and applications in thermoelectrics*. Vol. 2. 2012: CRC press.
14. Nandhakumar, I., N.M. White, and S. Beeby, *Thermoelectric materials and devices*. 2016: Royal Society of Chemistry.
15. Fan, X., et al., *PEDOT:PSS for Flexible and Stretchable Electronics: Modifications, Strategies, and Applications.* Advanced Science, 2019. **6**(19): p. 41.
16. Kroon, R., et al., *Thermoelectric plastics: from design to synthesis, processing and structure-property relationships.* Chemical Society Reviews, 2016. **45**(22): p. 6147-6164.
17. Adiga, S.P., et al., *Nanoporous membranes for medical and biological applications.* Wiley Interdisciplinary Reviews-Nanomedicine and Nanobiotechnology, 2009. **1**(5): p. 568-581.
18. Liu, Z., et al., *Flexible electronics based on inorganic nanowires.* Chemical Society Reviews, 2015. **44**(1): p. 161-192.
19. Witting, I.T., et al., *The Thermoelectric Properties of Bismuth Telluride.* Advanced Electronic Materials, 2019. **5**(6): p. 1800904.
20. LaLonde, A.D., et al., *Lead telluride alloy thermoelectrics.* Materials Today, 2011. **14**(11): p. 526-532.
21. Chiwanga, S., et al., *Chapter 9 Automotive Power Harvesting/Thermoelectric Applications*, in *Thermoelectric Materials and Devices*. 2017, The Royal Society of Chemistry. p. 230-251.
22. Nolas, G.S., D.T. Morelli, and T.M. Tritt, *SKUTTERUDITES: A Phonon-Glass-Electron Crystal Approach to Advanced Thermoelectric Energy Conversion Applications.* Annual Review of Materials Science, 1999. **29**(1): p. 89-116.
23. Slack, G.A., *Design Concepts for Improved Thermoelectric Materials.* MRS Proceedings, 2011. **478**: p. 47.
24. Hopkins, P.E., et al., *Phonon considerations in the reduction of thermal conductivity in phononic crystals.* Applied Physics A, 2011. **103**(3): p. 575-579.
25. Chen, Z., X. Zhang, and Y. Pei, *Manipulation of phonon transport in thermoelectrics.* Advanced Materials, 2018. **30**(17): p. 1705617.

26. Ryll, B., et al., *Structure, Phase Composition, and Thermoelectric Properties of YbxCo4Sb12 and Their Dependence on Synthesis Method.* ACS Applied Energy Materials, 2018. **1**(1): p. 113-122.
27. HOFMANN, T., *Nanostructured Energy Materials: From Organic Photovoltaic to Hybrid Thermoelectrics*, in *Soft Matter and Biomaterials on the Nanoscale*. p. 435-479.
28. Kim, W., R. Wang, and A. Majumdar, *Nanostructuring expands thermal limits.* Nano Today, 2007. **2**(1): p. 40-47.
29. Pei, Y., H. Wang, and G.J. Snyder, *Thermoelectric Materials: Band Engineering of Thermoelectric Materials (Adv. Mater. 46/2012).* Advanced Materials, 2012. **24**(46): p. 6124-6124.
30. Rowe, D.M., *CRC handbook of thermoelectrics*. 2018: CRC press.
31. Goldsmid, H. and R. Douglas, *The use of semiconductors in thermoelectric refrigeration.* British Journal of Applied Physics, 1954. **5**(11): p. 386.
32. Rowe, D.M., *Thermoelectrics handbook: macro to nano*. 2018: CRC press.
33. *Front Matter*, in *Thermoelectric Materials and Devices*. 2017, The Royal Society of Chemistry. p. P001-P004.
34. Nolas, G.S., J. Poon, and M. Kanatzidis, *Recent developments in bulk thermoelectric materials.* MRS bulletin, 2006. **31**(3): p. 199-205.
35. Polozine, A., S. Sirotinskaya, and L. Schaeffer, *History of Development of Thermoelectric Materials for Electric Power Generation and Criteria of their Quality.* Materials Research, 2014. **17**: p. 1260-1267.
36. Goldsmid, H.J. and A.W. Penn, *Boundary scattering of phonons in solid solutions.* Physics Letters A, 1968. **27**(8): p. 523-524.
37. Kasap, S., J. Málek, and R. Svoboda, *Thermal Properties and Thermal Analysis: Fundamentals, Experimental Techniques and Applications*. 2017. p. 1-1.
38. Hicks, L.D. and M.S. Dresselhaus, *Effect of quantum-well structures on the thermoelectric figure of merit.* Physical Review B, 1993. **47**(19): p. 12727.
39. Dames, C. and G. Chen, *Theoretical phonon thermal conductivity of Si/Ge superlattice nanowires.* Journal of Applied Physics, 2003. **95**(2): p. 682-693.
40. Bisi, O., S. Ossicini, and L. Pavesi, *Porous silicon: a quantum sponge structure for silicon based optoelectronics.* Surface Science Reports, 2000. **38**(1-3): p. 1-126.
41. Kolahalam, L.A., et al., *Review on nanomaterials: Synthesis and applications.* Materials Today: Proceedings, 2019. **18**: p. 2182-2190.
42. Canham, L., *HANDBOOK OF POROUS SILICON : Contents*. 2014.
43. Li, D., et al., *Thermal conductivity of individual silicon nanowires.* Applied Physics Letters, 2003. **83**(14): p. 2934-2936.
44. Mingo, N., et al., *Predicting the thermal conductivity of Si and Ge nanowires.* Nano Letters, 2003. **3**(12): p. 1713-1716.
45. Khardani, M., et al., *Electrical conductivity of free-standing mesoporous silicon thin films.* Thin Solid Films, 2006. **495**(1-2): p. 243-245.
46. Murphy, P. and J. Moore, *Coherent phonon scattering effects on thermal transport in thin semiconductor nanowires.* Physical Review B, 2007. **76**(15): p. 155313.
47. Pei, Y., H. Wang, and G. Snyder, *Thermoelectric Materials: Band Engineering of Thermoelectric Materials (Adv. Mater. 46/2012).* Advanced Materials, 2012. **24**(46): p. 6124-6124.
48. Zhang, B.A., et al., *Doping effects on the thermoelectric properties of pristine poly(3,4-ethylenedioxythiophene).* Rsc Advances, 2015. **5**(43): p. 33885-33891.
49. Mehta, R.J., et al., *Seebeck Tuning in Chalcogenide Nanoplate Assemblies by Nanoscale Heterostructuring.* ACS Nano, 2010. **4**(9): p. 5055-5060.
50. Zhao, Y., J.S. Dyck, and C. Burda, *Toward high-performance nanostructured thermoelectric materials: the progress of bottom-up solution chemistry approaches.* Journal of Materials Chemistry, 2011. **21**(43): p. 17049-17058.
51. Li, J.-F., et al., *High-performance nanostructured thermoelectric materials.* NPG Asia Materials, 2010. **2**(4): p. 152-158.
52. Schilz, J., et al., *Synthesis of thermoelectric materials by mechanical alloying in planetary ball mills.* Powder technology, 1999. **105**(1-3): p. 149-154.

53. Ji, X., et al., *Solvothermal synthesis and thermoelectric properties of lanthanum contained Bi–Te and Bi–Se–Te alloys.* Materials Letters, 2005. **59**(6): p. 682-685.
54. Kumari, L., et al., *Controlled hydrothermal synthesis of zirconium oxide nanostructures and their optical properties.* Crystal Growth and Design, 2009. **9**(9): p. 3874-3880.
55. Sanmathi, C., et al., *Microstructure control on thermoelectric properties of Ca0. 96Sm0. 04MnO3 synthesised by co-precipitation technique.* Materials Research Bulletin, 2010. **45**(5): p. 558-563.
56. Lee, J., et al., *Evolution of ZnO nanostructures in sol–gel synthesis.* Current Applied Physics, 2009. **9**(4): p. 792-796.
57. Ganguli, A.K., A. Ganguly, and S. Vaidya, *Microemulsion-based synthesis of nanocrystalline materials.* Chemical Society Reviews, 2010. **39**(2): p. 474-485.
58. Wu, X.-J., et al., *Electrochemical synthesis and applications of oriented and hierarchically quasi-1D semiconducting nanostructures.* Coordination Chemistry Reviews, 2010. **254**(9-10): p. 1135-1150.
59. Uhlir, A. and I. Uhlir, *Historical perspective on the discovery of porous silicon.* physica status solidi (c), 2005. **2**: p. 3185-3187.
60. Foll, H., et al., *Formation and application of porous silicon.* Materials Science & Engineering R-Reports, 2002. **39**(4): p. 93-141.
61. Granitzer, P. and K. Rumpf, *Porous Silicon-A Versatile Host Material.* Materials, 2010. **3**(2): p. 943-998.
62. Hernández-Montelongo, J., et al., *Nanostructured porous silicon: the winding road from photonics to cell scaffolds - a review.* Frontiers in bioengineering and biotechnology, 2015. **3**: p. 60-60.
63. Rouquerol, J., et al., *RECOMMENDATIONS FOR THE CHARACTERIZATION OF POROUS SOLIDS.* Pure and Applied Chemistry, 1994. **66**(8): p. 1739-1758.
64. Dimova-Malinovska, D., et al., *Preparation of thin porous silicon layers by stain etching.* Thin Solid Films, 1997. **297**(1-2): p. 9-12.
65. Kolasinski, K.W., *Porous silicon formation by galvanic etching.* Handbook of Porous Silicon, 2014. **2**.
66. Li, X. and P. Bohn, *Metal-assisted chemical etching in HF/H 2 O 2 produces porous silicon.* Applied Physics Letters, 2000. **77**(16): p. 2572-2574.
67. Solá, F., et al., *Electron beam induced growth of silica nanorods and heterostructures in porous silicon.* Nanotechnology, 2007. **18**(40): p. 405308.
68. Smith, R.L. and S.D. Collins, *POROUS SILICON FORMATION MECHANISMS.* Journal of Applied Physics, 1992. **71**(8): p. R1-R22.
69. Zhang, X.G., *Morphology and formation mechanisms of porous silicon.* Journal of the Electrochemical Society, 2004. **151**(1): p. C69-C80.
70. Harraz, F.A., et al., *Cylindrical pore arrays in silicon with intermediate nano-sizes: A template for nanofabrication and multilayer applications.* Electrochimica Acta, 2008. **53**(22): p. 6444-6451.
71. Kilian, K.A., T. Boecking, and J.J. Gooding, *The importance of surface chemistry in mesoporous materials: lessons from porous silicon biosensors.* Chemical Communications, 2009(6): p. 630-640.
72. Starkov, V.V., et al., *Silicon Structures with Variable Morphology of Pores Methods of Obtaining Physical and Optical Properties.* Journal of the Electrochemical Society, 2018. **165**(11): p. E534-E539.
73. Kumar, P., et al., *Tuning the pore wall morphology of mesoporous silicon from branchy to smooth, tubular by chemical treatment.* Journal of Applied Physics, 2008. **103**(2): p. 6.
74. Koshida, N. and T. Nakamura, *Emerging functions of nanostructured porous silicon—With a focus on the emissive properties of photons, electrons, and ultrasound.* Frontiers in chemistry, 2019. **7**: p. 273.
75. Kovacs, A. and U. Mescheder, *Transport mechanisms in nanostructured porous silicon layers for sensor and filter applications.* Sensors and Actuators B: Chemical, 2012. **175**: p. 179-185.
76. Jia, H., et al., *Hierarchical porous silicon structures with extraordinary mechanical strength as high-performance lithium-ion battery anodes.* Nature communications, 2020. **11**(1): p. 1-9.

77. Gadea, G., et al., *Silicon-based nanostructures for integrated thermoelectric generators*. Journal of Physics D-Applied Physics, 2018. **51**(42): p. 29.
78. Chen, M.Y., et al., *Electric-Field-Assisted Protein Transport, Capture, and Interferometric Sensing in Carbonized Porous Silicon Films.* Advanced Materials, 2011. **23**(39): p. 4537-4542.
79. Santos, H.A., *Porous silicon for biomedical applications.* 2014.
80. Huber, P., *Soft matter in hard confinement: phase transition thermodynamics, structure, texture, diffusion and flow in nanoporous media.* Journal of Physics-Condensed Matter, 2015. **27**(10): p. 43.
81. Hochbaum, A.I., et al., *Enhanced thermoelectric performance of rough silicon nanowires.* Nature, 2008. **451**(7175): p. 163-167.
82. Boukai, A.I., et al., *Silicon nanowires as efficient thermoelectric materials.* Nature, 2008. **451**(7175): p. 168-171.
83. Li, J.C., et al., *Vibrational and thermal properties of small diameter silicon nanowires.* Journal of Applied Physics, 2010. **108**(6): p. 5.
84. Lee, J.-H., G.A. Galli, and J.C. Grossman, *Nanoporous Si as an efficient thermoelectric material.* Nano letters, 2008. **8**(11): p. 3750-3754.
85. Tang, J., et al., *Holey silicon as an efficient thermoelectric material.* Nano letters, 2010. **10**(10): p. 4279-4283.
86. Boor, J., et al., *Thermoelectric properties of porous silicon.* Applied Physics A, 2012. **107**.
87. Christophersen, M., et al., *A comparison of pores in silicon and pores in III-V compound materials.* Physica Status Solidi a-Applied Research, 2003. **197**(1): p. 197-203.
88. Santos, A. and T. Kumeria, *Electrochemical etching methods for producing porous silicon*, in *Electrochemically Engineered Nanoporous Materials*. 2015, Springer. p. 1-36.
89. Pérez, E.X., E.i.A. Universitat Rovira i Virgili. Departament d'Enginyeria Electrònica, and U.R.i.V.E.T.S.d.E.d. Tarragona, *Design, Fabrication and Characterization of Porous Silicon Multilayer Optical Devices*. 2007: Universitat Rovira i Virgili. Escola Tècnica Superior d'Enginyeria.
90. Lehmann, V. and U. Gosele, *POROUS SILICON FORMATION - A QUANTUM WIRE EFFECT.* Applied Physics Letters, 1991. **58**(8): p. 856-858.
91. Lorensen, W.E. and H.E. Cline, *Marching cubes: A high resolution 3D surface construction algorithm.* SIGGRAPH Comput. Graph., 1987. **21**(4): p. 163–169.
92. Thommes, M., *Physical Adsorption Characterization of Nanoporous Materials.* Chemie Ingenieur Technik, 2010. **82**(7): p. 1059-1073.
93. Lowell, S., et al., *Characterization of Porous Solids and Powders: Surface Area, Pore Size and Density*. Vol. 1. 2006.
94. Thommes, M., et al., *Physisorption of gases, with special reference to the evaluation of surface area and pore size distribution (IUPAC Technical Report).* Pure and Applied Chemistry, 2015. **87**.
95. Brun, M., et al., *A new method for the simultaneous determination of the size and shape of pores: the thermoporometry.* Thermochimica Acta, 1977. **21**(1): p. 59-88.
96. Barrett, E.P., L.G. Joyner, and P.P. Halenda, *The Determination of Pore Volume and Area Distributions in Porous Substances. I. Computations from Nitrogen Isotherms.* Journal of the American Chemical Society, 1951. **73**(1): p. 373-380.
97. Brunauer, S., P.H. Emmett, and E. Teller, *Adsorption of Gases in Multimolecular Layers.* Journal of the American Chemical Society, 1938. **60**(2): p. 309-319.
98. W, A.N., et al., *Solid State Physics*. 1976: Holt, Rinehart and Winston.
99. Shirane, G., S.M. Shapiro, and J.M. Tranquada, *Neutron Scattering with a Triple-Axis Spectrometer: Basic Techniques*. 2002: Cambridge University Press.
100. Hwang, J.S., K.J. Lin, and C. Tien, *Measurement of heat capacity by fitting the whole temperature response of a heat-pulse calorimeter.* Review of scientific instruments, 1997. **68**(1): p. 94-101.
101. Parker, W.J., et al., *A FLASH METHOD OF DETERMINING THERMAL DIFFUSIVITY, HEAT CAPACITY, AND THERMAL CONDUCTIVITY*. 1960, ; Naval Radiological Defense Lab., San Francisco. p. Medium: X; Size: Pages: 27.
102. Cape, J.A. and G.W. Lehman, *Temperature and Finite Pulse-Time Effects in the Flash Method for Measuring Thermal Diffusivity.* Journal of Applied Physics, 1963. **34**(7): p. 1909-1913.

103. Borup, K.A., et al., *Measuring thermoelectric transport properties of materials.* Energy & Environmental Science, 2015. **8**(2): p. 423-435.
104. dos Santos, W.N., P. Mummery, and A. Wallwork, *Thermal diffusivity of polymers by the laser flash technique.* Polymer Testing, 2005. **24**(5): p. 628-634.
105. Cowan, R.D., *Pulse method of measuring thermal diffusivity at high temperatures.* Journal of Applied Physics, 1963. **34**(4): p. 926-927.
106. Martin-Palma, R.J., et al., *Thermoelectric properties of nanostructured porous silicon.* Materials Research Express, 2018. **5**(1).
107. Valalaki, K., P. Benech, and A. Galiouna Nassiopoulou, *High Seebeck Coefficient of Porous Silicon: Study of the Porosity Dependence.* Nanoscale research letters, 2016. **11**(1): p. 201-201.
108. Vega-Flick, A., et al., *Thermal conductivity reduction in highly doped mesoporous silicon: The effect of nano-crystal formation.* Journal of Applied Physics, 2018. **124**(8): p. 9.
109. Romano, G., A. Di Carlo, and J.C. Grossman, *Mesoscale modeling of phononic thermal conductivity of porous Si: interplay between porosity, morphology and surface roughness.* Journal of Computational Electronics, 2012. **11**(1): p. 8-13.
110. Romano, G. and J.C. Grossman, *Toward phonon-boundary engineering in nanoporous materials.* Applied Physics Letters, 2014. **105**(3): p. 033116.
111. Hofmann, T., et al., *Phonons in highly-crystalline mesoporous silicon: The absence of phonon-softening upon structuring silicon on sub-10 nanometer length scales.* Microporous and Mesoporous Materials, 2021. **312**: p. 110814.
112. Zdetsis, A.D. and C.S. Wang, *Lattice dynamics of Ge and Si using the Born-von Karman model.* Physical Review B, 1979. **19**(6): p. 2999-3003.
113. Aliev, G.N., B. Goller, and P.A. Snow, *Elastic properties of porous silicon studied by acoustic transmission spectroscopy.* Journal of Applied Physics, 2011. **110**(4): p. 043534.
114. Andrews, G.T., et al., *Brillouin light scattering from porous silicon films and multilayers.* physica status solidi (a), 2007. **204**(5): p. 1372-1377.
115. Grosman, A., J. Puibasset, and E. Rolley, *Adsorption-induced strain of a nanoscale silicon honeycomb.* EPL (Europhysics Letters), 2015. **109**(5): p. 56002.
116. Rolley, E., N. Garroum, and A. Grosman, *Using capillary forces to determine the elastic properties of mesoporous materials.* Physical Review B, 2017. **95**(6): p. 064106.
117. Minnich, A. and G. Chen, *Modified effective medium formulation for the thermal conductivity of nanocomposites.* Applied Physics Letters, 2007. **91**(7): p. 073105.
118. Nan, C.-W., *Physics of inhomogeneous inorganic materials.* Progress in Materials Science, 1993. **37**(1): p. 1-116.
119. Gor, G.Y., et al., *Elastic response of mesoporous silicon to capillary pressures in the pores.* Applied Physics Letters, 2015. **106**(26): p. 261901.
120. Wingert, M.C., et al., *Sub-amorphous Thermal Conductivity in Ultrathin Crystalline Silicon Nanotubes.* Nano Letters, 2015. **15**(4): p. 2605-2611.
121. Yang, L., et al., *Thermal conductivity of individual silicon nanoribbons.* Nanoscale, 2016. **8**(41): p. 17895-17901.
122. Cahill, D.G., S.K. Watson, and R.O. Pohl, *Lower limit to the thermal conductivity of disordered crystals.* Physical Review B, 1992. **46**(10): p. 6131-6140.
123. Chmelik, C., et al., *Nanoporous Glass as a Model System for a Consistency Check of the Different Techniques of Diffusion Measurement.* ChemPhysChem, 2011. **12**(6): p. 1130-1134.
124. Kondrashova, D., et al., *Scale-dependent diffusion anisotropy in nanoporous silicon.* Scientific Reports, 2017. **7**(1): p. 40207.
125. Klein, M.J., *Einstein, specific heats, and the early quantum theory.* Science, 1965. **148**(3667): p. 173-180.
126. Sze, S.M., *Semiconductor Devices: Physics and Technology*. 2012: John Wiley & Sons Singapore Pte. Limited.
127. Schliesser, J. and B. Woodfield, *Development of a Debye heat capacity model for vibrational modes with a gap in the density of States.* Journal of physics. Condensed matter : an Institute of Physics journal, 2015. **27**: p. 285402.
128. Miranda, E. and G. Mora-Barzaga, *How Good Is the Debye Model for Nanocrystals?* Journal of Modern Physics, 2019. **10**: p. 601-612.

129. Valentin, A., et al., *Study of phonon modes in silicon nanocrystals using the adiabatic bond charge model.* J. Phys.: Condens. Matter, 2008. **20**.
130. Baggioli, M. and A. Zaccone, *Universal origin of boson peak vibrational anomalies in ordered crystals and in amorphous materials.* Physical review letters, 2019. **122**(14): p. 145501.
131. Zeller, R. and R. Pohl, *Thermal conductivity and specific heat of noncrystalline solids.* Physical Review B, 1971. **4**(6): p. 2029.
132. Stephens, R.B., *Intrinsic low-temperature thermal properties of glasses.* Physical Review B, 1976. **13**(2): p. 852.
133. Graebner, J.E., et al., *Low-temperature properties of a superconducting disordered metal.* Physical Review Letters, 1977. **39**(23): p. 1480.
134. Holland, M., *Analysis of lattice thermal conductivity.* Physical review, 1963. **132**(6): p. 2461.
135. Callaway, J., *Model for Lattice Thermal Conductivity at Low Temperatures.* Physical Review, 1959. **113**(4): p. 1046-1051.
136. Kruglyak, Y., *Heat Transfer by Phonons in Landauer-Datta-Lundstrom Approach*. 2014.
137. Lundstrom, M.S. and C. Jeong, *Near-equilibrium transport: fundamentals and applications*. Vol. 2. 2012: World Scientific Publishing Company.
138. Kazan, M., et al., *Thermal conductivity of silicon bulk and nanowires: Effects of isotopic composition, phonon confinement, and surface roughness.* Journal of Applied Physics, 2010. **107**(8): p. 083503.
139. Slack, G.A. and S. Galginaitis, *Thermal conductivity and phonon scattering by magnetic impurities in CdTe.* Physical Review, 1964. **133**(1A): p. A253.
140. Jeong, C., S. Datta, and M. Lundstrom, *Thermal conductivity of bulk and thin-film silicon: A Landauer approach.* Journal of Applied Physics, 2012. **111**(9): p. 093708.
141. Kim, G.H., et al., *Engineered doping of organic semiconductors for enhanced thermoelectric efficiency.* Nature Materials, 2013. **12**(8): p. 719-723.
142. Chae, K., et al., *Enhanced Thermoelectric Properties in a New Silicon Crystal Si24 with Intrinsic Nanoscale Porous Structure.* Nano Lett, 2018.
143. Pietrak, K. and T.S. Wiśniewski, *A review of models for effective thermal conductivity of composite materials.* J. Power Technol., 2014. **95**: p. 14-24.
144. Siddiqui, M.U. and A.F.M. Arif, *Generalized effective medium theory for particulate nanocomposite materials.* Materials, 2016. **9**(8): p. 694.
145. Ghanbarian, B. and H. Daigle, *Thermal conductivity in porous media: Percolation-based effective-medium approximation.* Water Resources Research, 2016. **52**(1): p. 295-314.
146. Kiradjiev, K.B., et al., *Maxwell-type models for the effective thermal conductivity of a porous material with radiative transfer in the voids.* International Journal of Thermal Sciences, 2019. **145**: p. 106009.
147. Tian, W. and R. Yang, *Phonon transport and thermal conductivity percolation in random nanoparticle composites.* Computer modeling in engineering and sciences, 2008. **24**(2/3): p. 123.
148. Rayleigh, L., *LVI. On the influence of obstacles arranged in rectangular order upon the properties of a medium.* The London, Edinburgh, and Dublin Philosophical Magazine and Journal of Science, 1892. **34**(211): p. 481-502.
149. Cahill, D.G. and R.O. Pohl, *Thermal conductivity of amorphous solids above the plateau.* Physical review B, 1987. **35**(8): p. 4067.
150. Einstein, A., *Elementare Betrachtungen über die thermische Molekularbewegung in festen Körpern.* Annalen der Physik, 1911. **340**(9): p. 679-694.
151. Slack, G.A., *The thermal conductivity of nonmetallic crystals.* Solid state physics, 1979. **34**: p. 1-71.
152. Chen, Z., et al., *Rationalizing phonon dispersion for lattice thermal conductivity of solids.* National Science Review, 2018. **5**: p. 888-894.
153. Allen, P.B., et al., *Diffusons, locons and propagons: Character of atomie yibrations in amorphous Si.* Philosophical Magazine B, 1999. **79**(11-12): p. 1715-1731.
154. Agne, M., R. Hanus, and G. Snyder, *Minimum thermal conductivity in the context of: Diffuson -mediated thermal transport.* Energy & Environmental Science, 2018. **11**.
155. Dell'Anna, R., G. Ruocco, and G. Viliani, *High Frequency Sound Waves in Vitreous Silica.* Physical Review Letters, 1998. **80**.

156. Sette, F., et al., *Dynamics of glasses and glass-forming liquids studied by inelastic X-ray scattering.* Science, 1998. **280**(5369): p. 1550-1555.
157. Aroutiounian, V.M. and M.Z. Ghulinyan, *Electrical conductivity mechanisms in porous silicon.* Physica Status Solidi a-Applied Research, 2003. **197**(2): p. 462-466.
158. Forsh, P., et al., *Specific features of electrical transport in anisotropically nanostructured silicon.* Semiconductors, 2004. **38**(5): p. 603-606.
159. Ram, S., S. Kumar, and P. Cabarrocas, *Influence of the statistical shift of Fermi level on the conductivity behavior in microcrystalline silicon.* Physical Review B, 2007. **77**.
160. Zimin, S.P., *Hopping conductivity in low-porosity mesoporous silicon formed on p(+)-Si : B.* Semiconductors, 2006. **40**(11): p. 1350-1352.
161. Lubianiker, Y. and I. Balberg, *Two Meyer-Neldel rules in porous silicon.* Physical Review Letters, 1997. **78**(12): p. 2433-2436.
162. Kočka, J., et al., *Charge transport in porous silicon: Considerations for achievement of efficient electroluminescence.* Thin Solid Films, 1996. **276**: p. 187-190.
163. Cutler, M. and N.F. Mott, *Observation of Anderson localization in an electron gas.* Physical Review, 1969. **181**(3): p. 1336.
164. Mott, N. and E. Davis, *Disordered Materials. (Book Reviews: Electronic Processes in Non-Crystalline Materials).* Science, 1980. **207**: p. 1196-1197.
165. Kim, D., et al., *Phonon anharmonicity in silicon from 100 to 1500 K.* Phys. Rev. B, 2015. **91**: p. 014307.
166. Dalvi, A., N.P. Reddy, and S. Agarwal, *The Meyer–Neldel rule and hopping conduction.* Solid state communications, 2012. **152**(7): p. 612-615.
167. Fishchuk, I.I., et al., *Origin of Meyer-Neldel type compensation behavior in organic semiconductors at large carrier concentrations: Disorder versus thermodynamic description.* Physical Review B, 2014. **90**(24): p. 245201.
168. Lubianiker, Y. and I. Balberg, *A comparative study of the Meyer–Neldel rule in porous silicon and hydrogenated amorphous silicon.* Journal of Non-Crystalline Solids, 1998. **227-230**: p. 180-184.
169. Yakimov, A.I.e., et al., *The Meyer-Neldel rule in the processes of thermal emission and hole capture in Ge/Si quantum dots.* Journal of Experimental and Theoretical Physics Letters, 2004. **80**(5): p. 321-325.
170. Yelon, A., B. Movaghar, and H.M. Branz, *Origin and consequences of the compensation (Meyer-Neldel) law.* Physical Review B, 1992. **46**(19): p. 12244-12250.
171. Yelon, A., B. Movaghar, and R.S. Crandall, *Multi-excitation entropy: its role in thermodynamics and kinetics.* Reports on Progress in Physics, 2006. **69**: p. 1145.
172. Kikuchi, M., *The Meyer–Neldel rule and the statistical shift of the Fermi level in amorphous semiconductors.* Journal of applied physics, 1988. **64**(10): p. 4997-5001.
173. Drusedau, T. and R. Bindemann, *The Meyer - Neldel Rule and the Fundamental Pre -Exponential Factor in the Conductivity of a -Si:H.* physica status solidi (b), 1986. **136**: p. K61-K64.
174. Overhof, H. and P. Thomas. *The statistical shift model for the Meyer-Neldel rule*. in *Defect and Diffusion Forum*. 2001. Trans Tech Publ.
175. Balberg, I., *Transport in porous silicon: The pea-pod model.* Philosophical Magazine B, 2000. **80**(4): p. 691-703.
176. Shimizu, T., et al., *Proceedings of the Sixteenth International Conference on Amorphous Semiconductors - Science and technology - Kobe, Japan, September 4-8, 1995.* Journal of Non-Crystalline Solids, 1996. **200**: p. R7-R7.
177. Ben-Chorin, M., et al., *Hopping transport on a fractal: ac conductivity of porous silicon.* Physical Review B, 1995. **51**(4): p. 2199-2213.
178. Emin, D., *Phonon-assisted transition rates I. Optical-phonon-assisted hopping in solids.* Advances in Physics, 1975. **24**(3): p. 305-348.
179. Fishchuk, I.I., et al., *Unraveling the Role of Multiphonon Excitations and Disorder Concerning the Meyer-Neldel Type Compensation Effect in Organic Semiconductors.* Physical Review Applied, 2018. **10**(5): p. 054063.
180. Lundstrom, M., *Fundamentals of Carrier Transport*. 2009: Cambridge University Press.

Acknowledgement

A debt of gratitude is owed to my supervisor Dr. Tommy Hofmann and my doktorvater, PD.Dr. Klaus Habicht at Helmholtz-Zentrum Berlin für Materialien und Energie GmbH for their guidance, encouragement and support throughout the research, experimentation and development of this thesis. This would not have been possible without their diligent efforts, expertise, mentoring, leadership and co-operation.

I extend heartfelt gratitude to Prof. Dr. Mathias Bargheer (Universität Potsdam) and Prof. Dr Patrick Huber (Technische Universität Hamburg) for providing requisite facilities and advice throughout the research work. I am grateful to MatSEC graduate school for the financial support during the execution of the project.

I acknowledge the support of my co-workers, Dr. Katharina Fritsch for insightful discussions and Dr. Danny Kojda for assistance with macroscopic thermoelectric measurements. I thank Jan-Ekkehard Hoffmann for his assistance with SEM and Natalia Gostkowska-Lekner for UV-Vis experiments. I thank Dr. Dirk Wallacher for the technical support and for providing the access to etching lab. I am thankful to Dr. Sebastian Risse for the access to laser cutter lab.

Finally, I am grateful for the unconditional, unequivocal, and loving support of my family and friends.